DISSERTATION

# PROTEIN CRYSTALS AS NANOTEMPLATING MATERIALS

Submitted by

Ann Kowalski

Department of Chemical and Biological Engineering

In partial fulfillment of the requirements

For the Degree of Doctor of Philosophy

Colorado State University

Fort Collins, Colorado

Spring 2019

Doctoral Committee:

Advisor: Christopher Snow

Matt Kipper
Christie Peebles
Justin Sambur

ABSTRACT

PROTEIN CRYSTALS AS NANOTEMPLATING MATERIALS

The advancement of nanomaterial development depends on the reliable and scalable synthesis of three dimensional nanostructures and devices. Applications for these materials range from catalysis and energy storage to biomedicine and imaging. Towards the goals of shape-controlled immobilization and synthesis, templating is arising as a promising manufacturing method.

With the rise of bionanotechnology, DNA and protein scaffolds can be designed, synthesized, and functionalized to coordinate nanoparticles, enzymes, and other guests in three dimensions, or act as molds for the synthesis of anisotropic nanostructures. Inherently, protein crystals are an attractive target, as they have nearly unlimited designability, intrinsic functionality for a variety of useful materials, and mild reaction conditions.

The overarching goal of this work is to explore the feasibility of protein crystals as templates for the creation of biohybrid materials. We show that protein crystals with large solvent channels can strongly adsorb and immobilize gold nanoparticles by reversible metal affinity interactions and that these nanoparticles can serve as nucleation sites for the growth of nanorods within the pores of protein crystals by a variety of gold growth methods. We show that, depending on the method used, gold nanorod synthesis within the crystals can be dependent on the presence of a seed particle.

Despite their stability, these crystals can be dissolved to release the gold structures, which can be analyzed by electron microscopy and elemental analysis. A variety of gold nanorod products are formed, from highly anisotropic individual rods, to interconnected rod bundles, to parallel rods embedded within a protein matrix.

Additionally, we show that protein crystal pores can be used for the long-term capture of multiple enzymes and that these enzymes retain their activity within the crystal. Product can be separated by a simple washing step, and the immobilized two-enzyme pathway can be used for multiple cycles over several weeks. Rates of product formation are higher for enzymes immobilized within crystals of a high surface-to-volume ratio; thus, the use of micron-sized crystals minimizes transport limitations typically associated with enzyme immobilization. Preliminary work suggests the crystals may also impart significant thermal stability to the embedded enzymes.

Porous protein crystals may provide a superior templating method for the development of nanomaterials. Here we further demonstrate the wide variety of applications for protein crystals by revealing their success as scaffolds for immobilization, synthesis, and catalysis.

ACKNOWLEDGMENTS

*Thank you to all the past and present members of the Snow Lab for their support, encouragement, knowledge, and friendship.*

Dr. Christopher Snow
Dr. Thaddaus Huber
Dr. Lucas Johnson
Dr. Ning Zhao
Dr. Luke Hartje
Abby Ward
Julius Stuart
Jake Sebesta
Holly Dierl
Stacey Zintgraff
Sam Sloan

*Thank you to my collaborators at CSU and beyond for their expertise and insight.*

Dr. Chris Ackerson
Dr. Ricky Nemeth
Dr. Thomas Ni
Dr. Crystal VanderZanden
Suzanne Royer
Dr. Peter Ciesielski (NREL)

*Funding:*

National Science Foundation Interdisciplinary Graduate Education and Research Traineeship (Multidisciplinary Approaches to Science: Bioenergy)
National Science Foundation Grant Nos. 1434786, 5301057, 1434786, and 1506219
Colorado State University College of Engineering Graduate Teaching Fellowship

TABLE OF CONTENTS

LIST OF FIGURES

# CHAPTER 1. INTRODUCTION TO NANOMATERIAL TEMPLATING

*Nanomaterials and nanodevices*

A grand challenge in the development of nanomaterials is the reliable and scalable production of programmable, three dimensional nanostructures. Both arrays of these structures, where individual monomers are placed in specific locations and orientations with respect to one another, as well as purified solutions of structures, are of interest.[1,2] The low-cost, repeatable synthesis of these materials in arbitrary shapes would find a multitude of applications in light-harvesting, sensing, electronics, energy storage, catalysis, imaging, and medicine.[3–9]

Applications for these materials would benefit from shape-controlled synthesis and/or templated immobilization into 3D arrays. Most of the applications require either exact placement between nanoparticles, highly anisotropic structures, or size and shape precision on the sub-nanometer scale. These goals can be difficult to reach using in-solution synthesis methods.[10] Traditional methods for templating and patterning (e.g. lithography) can be slow, expensive, or have limited resolution. For example, many lithographic methods only pattern in two dimensions, while many others pattern in series, which is more difficult to scale up.[11,12]

*The benefit of templating*

Towards these ends, researchers have redesigned biomolecules for self-assembly, and achieved notable recent successes with DNA and protein

nanotechnology.[13–16] These scaffolds from nucleic acids, virus capsids, supramolecular assemblies, or protein cages act as molds and can provide specific attachments sites for immobilization of the nanostructures in three dimensions. There are several advantages to using biological templates: they have a variety of pre-existing morphologies and infinite designable ones, and they often have intrinsic functionalization towards metals, polymers, and other compounds.[17] Most reactions involving biomolecules are mild and many are environmentally friendly.

DNA crystals have been widely explored as templating scaffolds. Their large pores can function as molecular sieves or microreactors when loaded with enzymes. Protein crystals have been less explored, but may have several advantages including many functional groups for a wide range of guest attachment strategies, large solvent volume, and rigid structure that allows for atomic level characterization via x-ray diffraction despite their size. Protein templates have naturally repeating, patterned structures that allow for molecular level modifications and the addition of many other functional groups with affinity for nanostructures.[18,19] Much like DNA crystals,[20] porous protein crystals can also be crosslinked to form a robust template and modified to bind guest molecules.[21,22]

*Templating and immobilization with protein crystals*

Because of the high interest in designing protein assemblies and protein crystals for materials science and biotechnology applications, there are many recent, notable examples of the use of protein crystals and cages for nanomaterial capture, nanostructure synthesis, and catalysis.

Protein crystals can be used to capture metal ions, cofactors, and nanoparticles. Ceci and coworkers recently synthesized a hybrid cowpea mottle virus-ferritin protein cage that could capture RNA, Superparamagnetic iron oxide nanoparticles, and gold nanoparticles. There are many applications for these encapsulated guests, but this group specifically showed that these magnetic assemblies were excellent contrast enhancing agents during magnetic resonance imaging.[23] In a similar example, Tabe and coworkers used crosslinked hen egg white lysozyme (HEWL) crystals to immobilize Ruthenium complexes within the pores by attachment to Histidine residues. They used the captured organometallic complexes to perform reduction reactions.[24]

In addition to capturing guest molecules, researchers have also shown that protein crystals and cages can serve as vessels for the synthesis of various organic and inorganic nanostructures. In a recent example, England and coworkers synthesized polypyrrole (PPy) nanowire arrays within the pores of a crosslinked hen egg white lysozyme crystal. They showed that the polypyrrole-laden crystal was electrically conductive and insoluble in organic solvents. They were able to confirm via TEM that a thin section of the interior of the lysozyme crystal contained electron-dense wires, indicative of polypyrrole synthesis.[25]

Lastly, researchers have shown that protein cages and crystals can be used to perform catalysis and these reactions are often improved in the protein environment. For example, Tetter and Hilvert recently encapsulated three fluorescently-tagged enzymes within a ferritin cage and demonstrated that the enzymes were all highly active within the cage and were less effected by proteases and temperature increases than the free enzyme.[26] In a similar experiment, Liljestrom and coworkers synthesized a

hybrid cowpea mottle virus-avidin protein crystal that could be pre- or post-functionalized with horseradish peroxidase enzyme. The enzyme was highly active within the crystal.[27]

Although many groups are exploring the use of designed protein cages and assemblies as hybrid templating materials, the use of porous protein crystals has typically been limited to hen egg white lysozyme. However, there are many proteins that crystallize with much larger or more interestingly-shaped solvent channels than HEWL. In the presented work, we explore the development of a new large pore protein crystal as a template for capture, synthesis, and catalysis.

*Aims of the presented work*

This work demonstrates the use of protein crystals as templating materials for three main nanomaterial applications: (1) **capture** (Chapter II and IV), (2) **synthesis** (Chapter III), and (3) **catalysis (**Chapter IV).

In Chapter II (Fig. 1.1) we show that we can capture gold nanoparticles inside protein crystal scaffolds in a specific and generalizable scheme and quantify the loading of gold nanoparticles under various conditions. The gold nanoparticles can be captured within the pores for multiple days through shared metal affinity and can be released from the crystal using a metal chelator. The 3D organization of gold nanoparticles has applications in catalysis and optics.

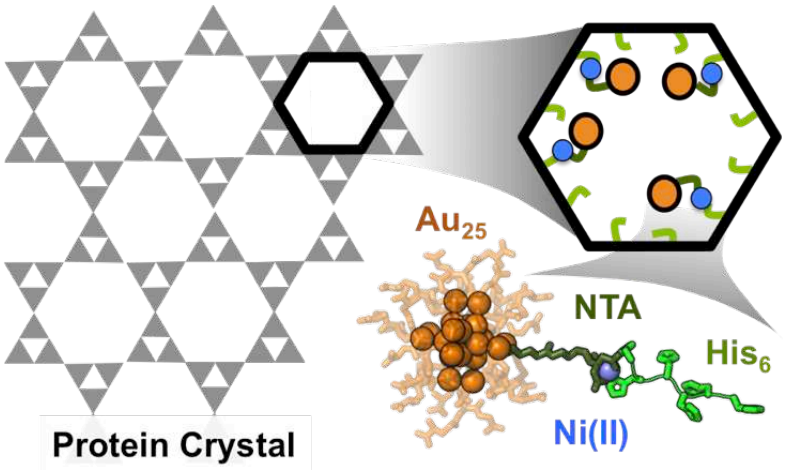


Figure 1.1 Chapter II schematic

25-atom gold nanoparticles with glutathione (GSH) and nitrilotriacetic acid (NTA) ligands can be reversibly bound to a protein crystal scaffold through NTA-Ni(II)-HisTag interactions.

In Chapter III, we demonstrate control over the synthesis of gold nanorods and larger particles within the protein crystal pores, and we characterize the resulting structures using electron microscopy and spectrometry. Gold nanoparticles from the previous work act as nucleation points for growth of nanorods within the cylindrical solvent channels of the crystal. This growth can be monitored by spectroscopy, or the resulting structures can be separated by dissolving the protein crystal. Highly anisotropic gold nanostructures have applications in sensing, imaging, and photothermal therapy.

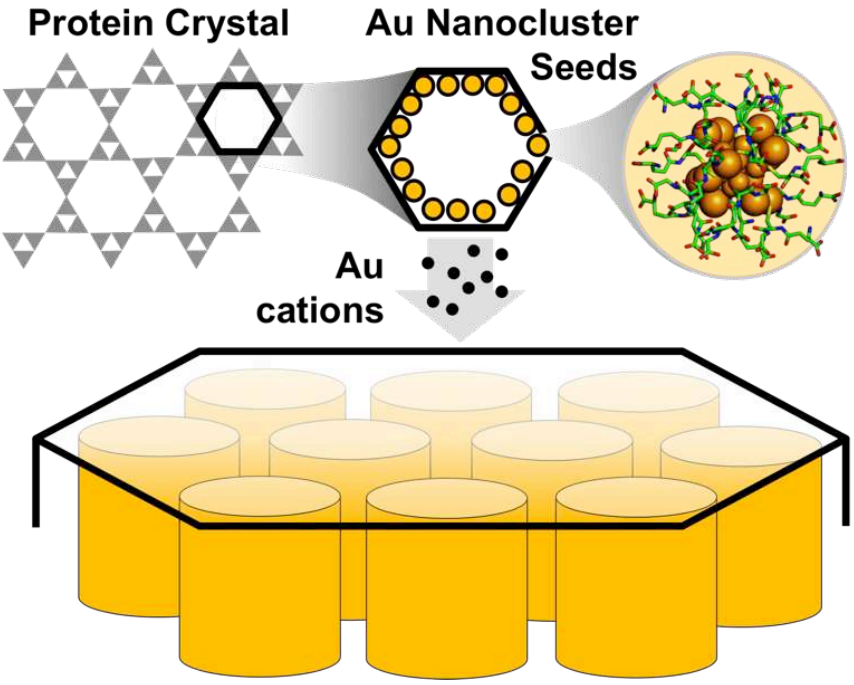


Figure 1.2 Chapter III schematic

Using previously attached 25-atom gold nanoparticles as ‘seeds,’ gold nanorods can be grown within the cylindrical pores of protein crystals.

In Chapter IV, we show that the same protein crystal can also be used to capture enzymes and that these enzymes are catalytically active within the crystal pores. An immobilized two-enzyme pathway remains active for multiple recycles over several weeks, and immobilization of enzymes within the crystal adds thermostability.

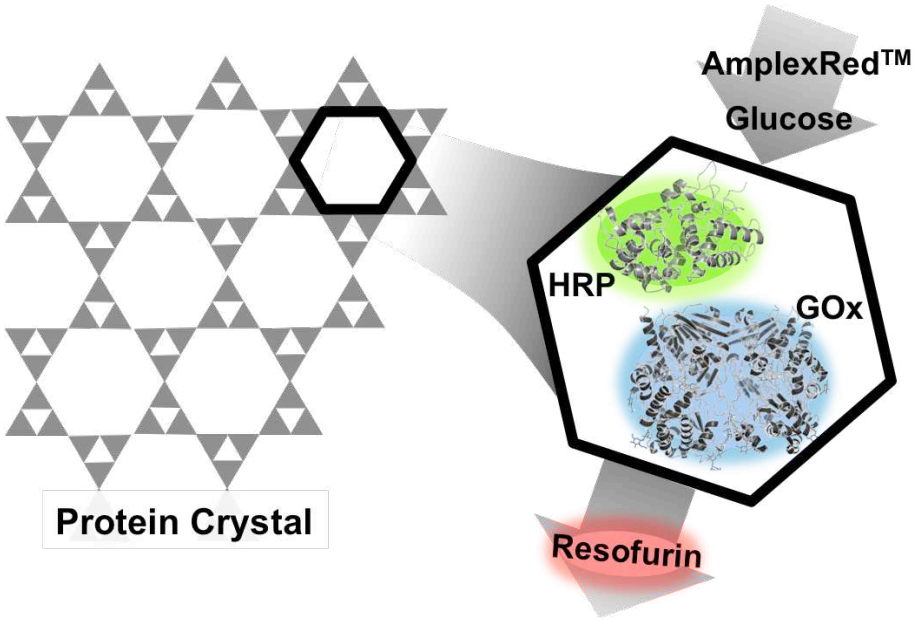


Figure 1.3 Chapter IV schematic

NHS-fluorescein labeled horseradish peroxidase (HRP) and CF405S-succinimydl ester labeled glucose oxidase (GOx) can be entrapped and remain catalytically active within the pores of a CJ protein crystal.

# CHAPTER 2. GOLD NANOPARTICLE CAPTURE IN PROTEIN CRYSTALS[*]

## SYNOPSIS

DNA assemblies have been used to organize inorganic nanoparticles into 3D arrays, with emergent properties arising as a result of nanoparticle spacing and geometry. We report here the use of engineered protein crystals as an alternative approach to biologically mediated assembly of inorganic nanoparticles. The protein crystal's 13 nm diameter pores result in an 80% solvent content and display hexahistidine sequences on their interior. The hexahistidine sequence captures $Au_{25}$(glutathione)$_{\sim 17}$ (nitrilotriacetic acid)$_{\sim 1}$ nanoclusters throughout a chemically crosslinked crystal *via* the coordination of Ni(II) to both the cluster and the protein. Nanoparticle loading was validated by confocal microscopy and elemental analysis. The nanoparticles may be released from the crystal by exposure to EDTA, which chelates the Ni(II) and breaks the specific protein/nanoparticle interaction. The integrity of the protein crystals after crosslinking and nanoparticle capture was confirmed by single crystal X-ray crystallography.

[*] Kowalski, A., Huber, T., Ni, T., Hartje, L., Appel, K., Yost, J., Ackerson, C., and Snow, C. *RSC Nanoscale.* 2016, **8**, 12693-12696.

# INTRODUCTION

## *Properties of gold nanoparticles*

Gold nanoparticles are of interest to researchers for their unique optical, electronic, and magnetic properties.[7,28] Gold, and other noble metal nanoparticles, have a unique surface plasmon resonance (SPR) that enhances their radiative and non-radiative properties[29] and local electromagnetic field.[28] This SPR arises from collective oscillation free electrons on the metal induced by the oscillating electromagnetic field of incoming light. The metal surface's electron oscillation reaches a maximum amplitude for a specific frequency of light; this is called the surface plasmon resonance.[30] The SPR causes strong absorbance of light at this wavelength and is much stronger for plasmonic metals like gold and silver than other metals.[31,32]

The strength of the surface plasmon resonance and the wavelength at which it occurs are very sensitive to changes in particle size, shape, and composition.[29] For example, larger spherical gold nanoparticles (~100 nm) have a broad absorption peak at a 600 nm wavelength, whereas smaller spherical gold nanoparticles (~20 nm) have a sharp absorption peak at wavelengths around 520 nm. This arises in part due to differences in the ratio of surface plasmon collisions to overall particle size.[33,34] Additionally, gold nanoparticles of differing shape (e.g. rods) can have multiple absorbance peaks associated with the dimensions of each distinct axis[34]; this will be covered further in the next section.

Light extinction by colloidal gold nanoparticle solutions comes from light absorption due to SPR, as well as Raman light scattering. Raman scattering occurs

when photons are released from particles at higher wavelengths than at which they are absorbed. SPR oscillations increase both the absorbance and Raman scattering of gold nanoparticles beyond fives times that of conventional dyes and fluorescent molecules of comparable size.[8]

Theoretical and experimental physicists are also interested in the magnetic properties of gold nanoparticles. Some small gold nanoparticles, between 1.4 nm and 15 nm in diameter, with thiol-ligands (or other covalently-bound ligands) capping the surface, exhibit ferromagnetism.[33] Surfactant stabilized nanoparticles, or those with electrostatically-bound ligands, do not typically exhibit permanent magnetism. This is similar to bulk gold samples.[33] This is a particularly surprising result because metals like gold are measured to be diamagnetic; altering the magnetism by preparing functionalized gold particles is a new and exciting field of magnetism research.[35]

Overall, gold nanoparticles have interesting and useful electronic, optical, and magnetic properties. These properties different from bulk gold, and can be tuned significantly by altering surface groups, particle shape and size, and surrounding medium. There is significant research into the properties and applications for gold nanoparticles in fields ranging from theoretical physics to biomedicine. Better understanding of how nanoparticles behave in solution, as well as in organized arrays, will create many new applications in the future.

*Properties of gold nanoparticle assemblies*

Not only do individual gold nanoparticles exhibit unique properties, but these properties are modified in ordered assemblies depending on the distance between particles, the size of the particles, and the orientation of particles relative to each

other.[36–38] For example, closely spaced gold nanoparticles can act as waveguides for the transmission of electromagnetic energy due to near-field coupling. Essentially, the plasmon resonance induced on an individual nanoparticle by light at a specific frequency can be transferred to a near neighbor (within tens of nanometers away). This "guide" of electrons is dependent on the size of particles and the distance between them.[39,40]

These waveguides are useful optical devices because they are not limited by the diffraction limit of light; nanoscale devices can more easily be fabricated with this method.[41] Most waveguide instruments at the sub-micron scale have only been theorized, but several examples exist at the microwave regime with nanoparticles approximately 50 nm in diameter with particle spacing between 75 and 125 nm. These assemblies can be fabricated with electron-beam lithography and experimentally show that electron transport occurs in gold nanoparticle chains below the diffraction limit of light.[42]

There is still much to learn about gold nanoparticle assemblies as they contribute to plasmonic devices. Theoretical and experimental work has shown promise in tuning and minimizing the propagation of energy loss along these nanoparticle chains. In one study, loss was cut in half by increasing the aspect ratio of the individual particles.[41] In another study, it was discovered that because the wavelength of light is greater than the bending radius in these plasmonic devices, information could be transferred around $90^0$ corners and other sharp changes in device shape.[39] These discoveries are essential to the creation of more complex nanoscale electronics and circuits.

Besides one-dimensional waveguides, two- and three-dimensional arrays of gold nanoparticles also have interesting properties. In many cases, these nanostructures self-assemble into highly ordered superlattices upon controlled evaporation of their surrounding media (usually an organic solvent).[1] Self-assembly is observed under a variety of conditions and with different ligands, and seems to be dependent on particle size and a balance between attractive and repulsive forces.[43] For example, there have been many studies which explore the phenomenon of bimodal self-assembly where particles of homogenous size arrange themselves by spontaneous segregation.[1,44]

Several groups have fabricated "thin films" of colloidal gold nanoparticles and studied the relationship between film thickness (number of layers of crosslinked gold nanoparticles) and resistivity.[45] These thin films have non-metallic properties and retain conductivity similar to that of nanostructured bulk materials, without fusing into bulk gold.[46] Most of these films have thiol linker molecules between particles and individual particle sizes from 4 to 10 nm. Here again the distance between particles is a major factor driving their conductivity (e.g. whether they behave as particles or thin continuous gold films),[1] and other unusual properties including electron hopping and Coulomb staircase behavior.[46,47]

Additionally, gold nanoparticle arrays of similar dimensions but containing distinct linker molecules can have different absorbances, due to shifts in resonance states.[48] For example, Wessels *et. al.* fabricated identical, three dimensional arrays of gold nanoparticles in which different linkers of similar length could define the overall behavior of the array. The three-dimensional arrays contained 4 nm gold nanoparticles interlinked with thiol- or carbomate- terminated linkers. Thiol-terminated linkers lowered the

plasmon absorption bands from 630 nm to 550 nm when compared to carbomate-terminated linkers. Additionally, the presence of cyclohexane instead of benzene rings lowered conductivity by one order of magnitude. This shows it is possible to tune both the optics and the electronic properties (from insulating to conducting) without changing the gold nanoparticle size or spacing.[48]

More recently, Shiigi and Nagaoka fabricated a miniaturized device in the form of a 2D array of gold nanoparticles with nanometer spacing. This array is highly sensitive to very small electrical signals and could act as a switch depending on the conducting or insulating properties of the spacer molecules.[49] The widespread application of these technologies still depends on further study, which is often limited by the ability to develop a wide variety of shapes and sizes of arrays. The ability to control the fabrication of these systems on the nanometer scale will contribute significantly to their further development.

*Applications for gold nanoparticles and arrays*

The applications for these nanoparticles and their two- and three-dimensional lattices are seemingly endless. Although many of the applications are in biomedicine and other bio-related fields, there are also applications in chemical catalysis, energy storage, and electronics. Most studies shown that gold nanoparticles have relatively little cytotoxicity up to concentrations of 100 gold nanoparticles per cell, which makes them attractive for biological use. However, protecting ligands may have an adverse effect, as may linker molecules used in arrays.[50]

*Biological Applications*

Gold nanoparticles can be used in detection of everything from nucleic acids to enzymatic reactions based on their scattering, fluorescence, and visible color change with respect to size and inter-particle distance. For example, a solution of 15 nm diameter gold nanoparticle will typically look pink by eye. In the presence of an antigen that binds to the nanoparticle surface, the particles will agglutinate. When their inter-particle distance becomes less than that of their diameter, the overlap in their dipoles leads to a darker purple solution. The color change indicates the presence or absence of an antigen, nucleic acid, or other molecule of interest. These same principles are used when gold nanoparticles enhance (Raman scattering)[51] or quench (fluorescence) the signal of a nearby molecule.[52] One group reports detection of a certain liver toxin by gold nanoparticles on the order of 0.6 parts per billion.[36]

Gold nanoparticles are also easy to synthesize with various surface functional groups. Rai *et. al.* functionalized the surface of 20 nm gold nanoparticles with antimicrobial molecules. They further attached these particles to glass surfaces to create a stable, reusable, antimicrobial surface that was effective against *Staphylococcus aureus* and *Escherichia coli*. Because of the low toxicity of gold nanoparticles, this has applications in biomedicine as well.[53] Gold nanoparticles have been used in a variety of drug and gene delivery schemes. Their advantages include targeted delivery, added stability, prevention of enzymatic degradation, and secure cell wall penetration. Gold nanoparticles can agglomerate naturally at certain cites within the body, or they can be actively targeted to sites through binding to specific molecules.

Because of gold's unique optics, light can be used to release payloads at certain locations.[9]

Some recent *in vivo* studies have used gold nanoparticles to induce cell death via hyperthermia therapy. In combination with radiotherapy and chemotherapy, hyperthermia therapy, the controlled addition of heat to cause apoptotic cell death, has been shown to increase overall patient survival. Traditional hyperthermia therapy has several drawbacks. It's difficult to heat deep tumors to the necessary temperature, and tumor selectivity is low. The use of gold nanoparticles to target tumors and induce thermal therapy is a promising route. The nanoparticles can be targeted to tumor sights magnetically, through the enhanced permeability and retention effects,[54] or by surface functionalization. In one example, 100 nm diameter silica particles coated with a 15 nm diameter gold shell were used. The silica core and gold coating shifted the surface plasmon resonance peaks to near infrared. At these wavelengths, maximum transmission can be achieved through blood and tissues. A laser can be used to heat the particles up to 37$^{o}$C, causing irreversible tissue damage to the tumors.[55]

Gold nanoparticles can also be used to increase the uptake of certain chemotherapeutic drugs, and their absorption of ionizing radiation has led to enhancements of sensitivity during radiotherapy, which can cleave DNA. However, extremely high doses of gold nanoparticles (8.5 uL/g or up to 5000 gold nanoshells per cancer cell) are still required for these applications.[54–56]

The same properties that make gold nanoparticles useful for therapeutics are also useful in imaging, but for slightly different reasons. In fact, the size of gold nanoparticle can guide the choice of application. For smaller gold nanoparticles (~20 nm

in diameter), almost all light extinction is caused by absorption. By the time gold nanoparticles are 80 nm in diameter, both absorption and scattering contribute almost equally to extinction. This means, smaller gold nanoparticles are ideal for therapies, as most light is absorbed and efficiently converted to heat. Larger gold nanoparticles are often used in biological imaging, as they have a higher scattering efficiency.[29] High electron scattering, coupled with low toxicity and the ability of gold nanoparticles to be functionalized with a variety of surface layers that target specific molecules, make them excellent contrast agents for biological images ranging from cancer cells to bacteria to damaged bone tissue.[57,58]

Arrays of gold nanoparticles have promising applications in a variety of sensors. Because of their extreme sensitivity to electrical currents, they can be used to study trace amounts of compounds. Recently, Peng et. al. fabricated a 3 mm gold electrode array coated with 5 nm gold nanoparticles functionalized with organic capping layers. These sensors exhibited a reversible change in electrical resistance when they were exposed to the breath of patients with various types of cancer. The sensors, depending on their organic compound ligand layer, were able to differentiate among volatile organic compounds present in healthy humans versus patients with lung, breast, colon, or prostate cancer.[59] Gold nanoparticles have also been used to sense DNA, heavy metal ions, cells, proteins, thiols, glucose, and many other biomolecules.[3,4]

*Non-biological applications*

Beyond biological applications, physicists and chemists are interested in gold nanoparticle's applications in catalysis, energy storage, and nanoelectronics. Gold

nanoparticles, with their high surface-to-volume ratio, stability in the presence of water or oxygen, and overall robust structure, make attractive catalysts for a host of organometallic chemical conversions. They often use milder conditions and are more selective and efficient than other catalysts and other synthesis pathways.[60,61] Interestingly, the mechanisms for some of these reactions are still not known; Au(III) can sometimes catalyze the same reactions as Au(I) without a change in oxidation state.[62]

Self-assembling gold nanoparticle arrays may find applications in photovoltaic cells.[5] In general, self-assembly is a cost efficient manufacturing strategy for nanoelectronics. For photovoltaic and other electronics, complex and exact nanoarchitectures must be realized in order to optimize charge transport and maximize light absorption.[36] Recently, Suresh et. al. have developed a method for building dense gold nanoparticle arrays for applications in nanocrystal flash memories. The use of hierarchical self-assembly in this method allows for increased charge storage density without increasing required voltage.[63] Another group recently developed a gold nanoparticle array triboelectric generator. This device is capable of harvesting mechanical energy from common ambient occurrences such as human footsteps and ocean waves. The optimized nanoscale surface lead to record high power output.[64]

Applications for functionalized gold nanoparticles and their arrays and superlattices are widespread. The economical, precise, large-scale production of these structures will be necessary to realize many of their purposes and contribute to their further study.

*Synthesis of gold nanoparticle arrays*

There are two major classes of synthesis for gold nanoparticle arrays: top-down and bottom-up. Self assembly and templating methods are considered bottom-up; you start with the building blocks and place them together to create an array. Lithographic methods are often considered top-down; you write an array onto a surface, or etch away at a surface to produce an array.

There are quite a few etching and writing lithograph techniques that have been used to create a variety of two- and three-dimensional patterns of gold nanostructures. They include nanosphere lithography, electron lithography, micro-contacting printing, nanoimprint lithography, and photolithography. Nanosphere lithography involves the use of a pre-existing pattern of polymer spheres, usually polystyrene, upon which a gold film is sputtered to a desired height. The polystyrene spheres can be removed by sonication, which leaves patterns of gold triangles or disks in the void space. At increased temperatures, called thermal dewetting, these triangles or disks have the tendency to form spheres, which allows some shape control. Nanosphere lithography has some shape and size barriers and is typically limited two dimensions.[12]

Electron beam lithography is a high resolution etching method that uses electrons to remove patterns on a sputtered gold surface. Recently it has been shown to create a two-dimensional pattern of gold nanostructures on a titanium slide and has been used successfully in surface-enhanced Raman scattering. Like nanosphere lithography, it is also restricted to two dimensions. Additionally, it is a serial method; the electron beam travels over a surface instead of etching the entire grid in parallel. This limits the scale-up feasibility.[65]

Two very similar lithographic methods are nanoimprint lithography and micro-contact printing. Micro-contact printing uses an etched PDMS block coated in gold “ink” to stamp a pattern onto a slide. This method is relatively fast and cheap, as entire slides can be stamped at once. However, the resolution is severely limited by the etching ability on the PDMS block. Similarly, nanoimprint lithography uses a stamp to mechanically deform the surface of a gold-coated slide. Again this method is quick and cheap, but limited by the design capabilities of the stamp.[17]

Photolithography uses light to etch away a gold surface. Recently researchers fabricated an array of 100 nm diameter gold nanospheres of 5 um spacing on a silica slide. Thermal dewetting is again used to reduce the size and alter the final shape of the gold nanoparticles. The resulting structures have applications in high-sensitivity plasmonic biosensing, but are again limited to two-dimensions and micrometer resolution.[11] Overall, lithographic methods are useful on the small scale and for high-cost applications, but may by difficult to implement in lost-overhead, commercial scale productions.

Self-assembly is a promising method for creating a variety of gold arrays. Self-assembly can either occur spontaneously or be induced by linkers, temperature, and solution changes. Boal et. al. showed that increasing the temperature generally decreased the size of gold nanospheres synthesized by polymers with gold recognition capabilities.[66] Self-assembly can also be induced by solution changes and evaporation. For example, a randomly scattered mono-layer of gold nanoparticles on a silicon surface will organize itself into small patches of two-dimensional aggregates upon the

addition of an alkanethiol solution. An alcohol solution forces the aggregates to form a repeating, hexagonal structure on the surface.[67]

Recently, the dynamics of self-assembly of gold nanoparticles was observed under liquid cell transmission electron microscopy. Surfactant-coated gold nanoparticles were linked together in a chain by the presence of ethylenediammonim, which hydrogen bonds with the surface layer on the gold.[68] Self-assembly in general is limited by theoretical explanations followed by trial and error experimental approaches which can lead to unexpected results. However, understanding the assembly mechanisms is important, and self-assembly characteristics are often the first step in templating, the newest and most-promising method for nanoscale assembly control in three dimensions.

Polymer templates are sometimes used to control the assembly of gold nanoparticles. For example, three-dimensional, hexagonal, mesoporous silica films were used to create an ordered structure of 2.5 nm diameter gold spheres. Additionally, when the surrounding silica film was dissolved, the gold spheres could retain an unsupported superlattice structure in the presence of hydrogen fluoride.[69] Additionally, block co-polymer monolayers can organize gold nanoparticles,[70] and act as nanoreactors for subsequent gold-catalyzed chemistry.[71] The major drawbacks in using polymers as templates are the lack of existing strategies for synthesizing complex polymers of the necessary topology and containing specialized components. Additionally, long-range order is sometimes lost in polymers unless a mechanical or electromagnetic flow is used.[17]

*Biological Templating*

The use of biological scaffolds is an emerging field for the organization of gold nanoparticles in three dimensions. Biological templating is promising because of the inherent structural diversity already contained in biological species and materials. Biotemplates also have the potential to be high resolution, parallelizable, and cost effective. They also function well at ambient conditions and often don't require harsh chemicals, making them more energy efficient and environmentally friendly than other traditional fabrication methods.[17]

DNA is likely the most common templating method for gold nanoparticle arrays. Both DNA origami[72] and cDNA[73] based approaches have been used to control the assembly of gold nanoclusters. DNA origami templated self-assembly has been used to create a linear waveguide of 1 nm diameter gold nanoparticles.[74] In a notable recent example, Thacker *et. al.* placed gold nanoparticle dimers of 40 nm diameter onto a DNA origami "platform" to a final spacing between particles of less than 5 nm. This assembly could detect the presence of an analyte using SERS, as well as the sequence of a single-stranded DNA oligonucleotide attached to the gold particles.[75] DNA can also be used to study the crystallization phenomenon of nanoparticles.[76] Additionally, DNA origami has the added benefit of long-range organization of gold nanoparticles. Self-assembly with smaller molecular linkers is limited to interparticle distances of less than 10 nm.[77] There are numerous examples of DNA-based organization of particles.[17,78]

Though DNA has been thoroughly explored,[79–82] the use of proteins to organize nanoparticles is less well established. This is in part because protein oligomer assembly structures are harder to predict than DNA nanostructures. Protein templating allows

molecular-level modifications and the use of mild reaction conditions, and proteins already have many different functional groups with affinities for various nanostructures.[17] Notable examples of protein organization of nanoparticles include the use of viruses[83–85], chaperonin protein templates,[86] and multimeric proteins[87–91] to organize particles. Kostiainen *et. al.* prepared binary superlattices by co-assembling protein cages with nanoparticles.[23] Groups have also used chaperonin protein crystals,[19] bacterial surface layer (S-layer) protein units,[92] and lysozyme amyloid fibers[93] to organize gold nanoparticles in one and two dimensions by electrostatic interactions.

More recently, Maity et. al. co-crystallized Au(III) ions from potassium gold chloride ($KAuCl_4$) with a spherical, 24-mer ferritin protein cage. After crystallization and stabilization by crosslinking, gold ion movement and gold nanoparticle formation due to sodium borohydride reduction inside the crystal was studied. From this, protein-gold binding pockets were elucidated and some mechanism of nanoparticle formation in a protein environment was determined.[94] Similarly, another group co-crystallized gold nanoparticles inside lysozyme crystals and found that the gold assembled within the crystal by electrostatic affinity for the protein.[95] These examples show the ability of proteins and protein crystals to work as scaffolds for the immobilization of gold nanoparticles in three dimensions.

*Impacts of presented work*

There are well over one hundred thousand protein crystal structures deposited in the Protein Data Bank with pore diameters beyond 25 nm.[96] The pores of protein crystals are often used to facilitate diffusion of cofactors, drugs, and substrates into

crystals, in order to observe the biological effects of these molecules in single crystal x-ray structural studies.[97] Diffusion of metals into crystals is also used in metal based phasing methods such as multiple anomalous dispersion and multiple isomorphous replacement.[98–100] Indeed, small metal clusters were used for phasing the largest biomacromolecules solved by single-crystal x-ray methods.[101] The diversity of available protein crystals, as well as their abundant structural information, make them ideal templates for organizing gold nanoparticles and other molecules. Compared to other scaffold materials, crosslinked protein crystals offer potential advantages in terms of stability and precision in the face of changing solvent conditions. Nonetheless, protein crystals represent a less explored scaffold.[102,103]

To our knowledge, this report is the first example of successful, controlled adsorption of larger nanoparticles into a pre-existing protein crystal. In the above examples, the conventional 'soaking' of metal coordination complexes and clusters into crystals for phasing relies on serendipitous binding; the metals do not adsorb to specified sites.[95] In contrast, we capture gold nanoparticles at defined sites inside an existing protein crystal via a specific metal-mediated interaction. A key benefit of metal-based capture motifs is the relative ease of generalizing the capture motif to other guest molecules and other templates. The precise control of gold nanoparticle placement in arbitrary 3D arrays will advance applications in sensors, energy storage, and catalysis.

RESULTS

This project uses a protein crystal, CJ, to bind 25-atom gold nanoparticles ($Au_{25}$) at defined sites within the crystal pores. CJ0 (Genebank ID: cj0420, Protein Data Bank code: 2fgs) is a putative periplasmic polyisoprenoid-binding protein from *Campylobacter jejuni.* It was identified from the Protein Data Bank in an automated search for proteins that crystallize with large pores. The vector encoding CJ0 was obtained from Protein Structure Initiative: Biology-Materials Repository. For ease of uniform expression and purification, the periplasmic signaling peptide was deleted, yielding the target gene, CJ. CJ has a C-terminal histag and encoded in expression vector pSB3. A variant of CJ (CJΔH6) was cloned to insert a tobacco etch virus (TEV) protease cleavage site between the protein and an N-terminal hexahistidine tag. After initial purification and buffer exchange, this protein was incubated with TEV protease (1:100 $OD_{280}$) overnight at 4 °C. Following TEV cleavage, the protein was reverse purified by immobilized metal affinity chromatography to remove TEV and uncleaved protein.

CJ crystals can be grown and crosslinked by a variety of methods. For example, they can be grown (Fig. 2.1) in mTacsimate™ buffer and crosslinked by direct addition of 1% glyoxal and 25 mM dimethyl amine borane complex (DMAB). Tacsimate™ is an organic acid mixture from Hampton Research, optimized for protein crystallization, which we modified to remove compounds containing primary amines. The crosslinking reaction is quenched after two hours via addition of 0.3 M hydroxylamine and 25 mM DMAB at pH 5. Additionally CJ crystals can be grown in an ammonium sulfate buffer and crosslinked by direct addition of 40 mg/mL 1-Ethyl-3-(3-

dimethylaminopropyl)carbodiimide (EDC) and 100 mM imidazole. This crosslinking reaction can be quenched in a pH 10 buffer.[104] The above described growth and crosslinking methods are the two primarily used in this thesis. Buffer concentrations and pHs can be altered slightly to optimize crystal size, thickness, and quality for each batch of purified protein.

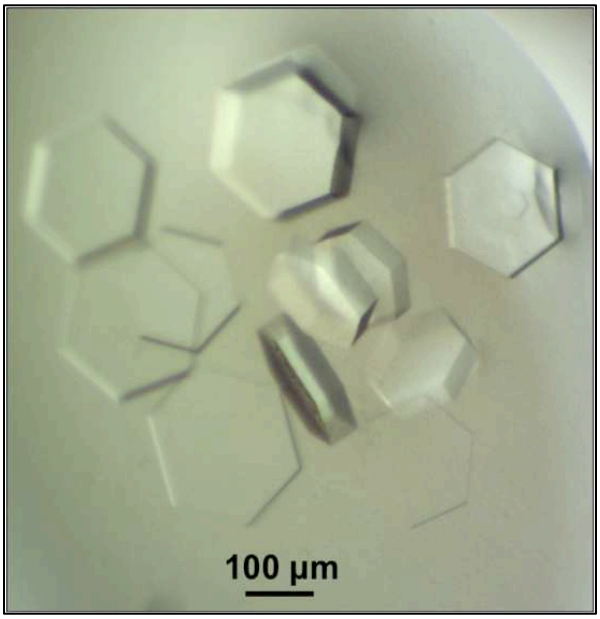


Figure 2.1 CJ crystals

Brightfield optical transmission image of a sitting drop growth well of CJ crystals in mTacsimate,™

*Gold loading experiments*

The first step in this project was to probe the ability of the protein crystals to "load" the guest gold nanoparticles. It is expected that the nanoparticles should load very quickly into the pores, as their diameter (~3 nm) is much smaller than that of the crystal pore (~13 nm) (Fig. 2.2).

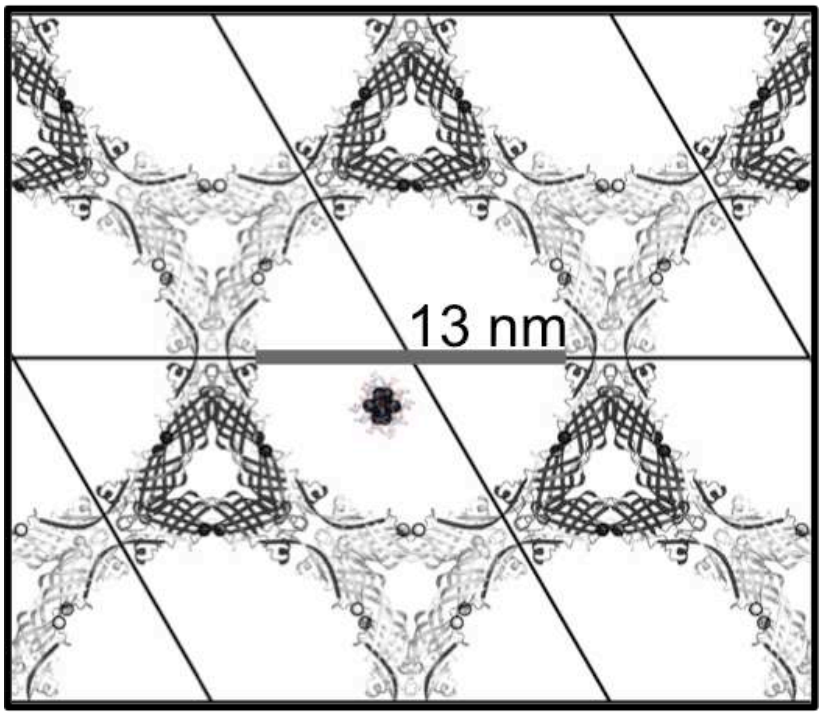


Figure 2.2 CJ Pymol rendering

Rendering of a CJ protein crystal pore (grey) in relation to a $Au_{25}$ cluster (navy) and surrounding glutathione ligands (red).

Loading and unloading experiments were first done using $Au_{25}$ clusters tagged with NHS-fluorescein molecules for ease of observation. The $Au_{25}$ clusters are surrounded by either 18 glutathione ligands ($Au_{25}(GSH)_{18}$), or 17 glutathione ligands and ~1 nitrilotriacetic acid ligand ($Au_{25}(GSH)_{17}NTA$). The fluorescent label was attached to the glutathione ligands via amine coupling. To conjugate, 1 mg of NHS-fluorescein was dissolved in 100 uL of DMSO. Two microliters of this solution was added to 100 uL of a 50 uM $Au_{25}$ solution. After incubation at $4^{o}C$ for 3 hrs, the unreacted dye was removed by centrifugation in a 3 kDa Amicon filter.

Preliminary data showed that NHS-fluorescein labeled $Au_{25}(GSH)_{17}NTA$ nanoparticles could be loaded and unloaded from crosslinked CJ protein crystals. The

top row of Figure 2.3 shows a brightfield transmission image of an empty CJ protein crystal (left), followed by a timelapse of a CJ protein crystal under 405 nm wavelength light in a well of the gold nanoparticle solution. After ~10 minutes, the crystal looks to be fully loaded with particles. Over time, the surrounding solution becomes darker as the gold nanoparticles adsorb into the crystal. Upon transfer to a drop of water (bottom row), the gold nanoparticle solution leaves the crystal over 60 minutes.

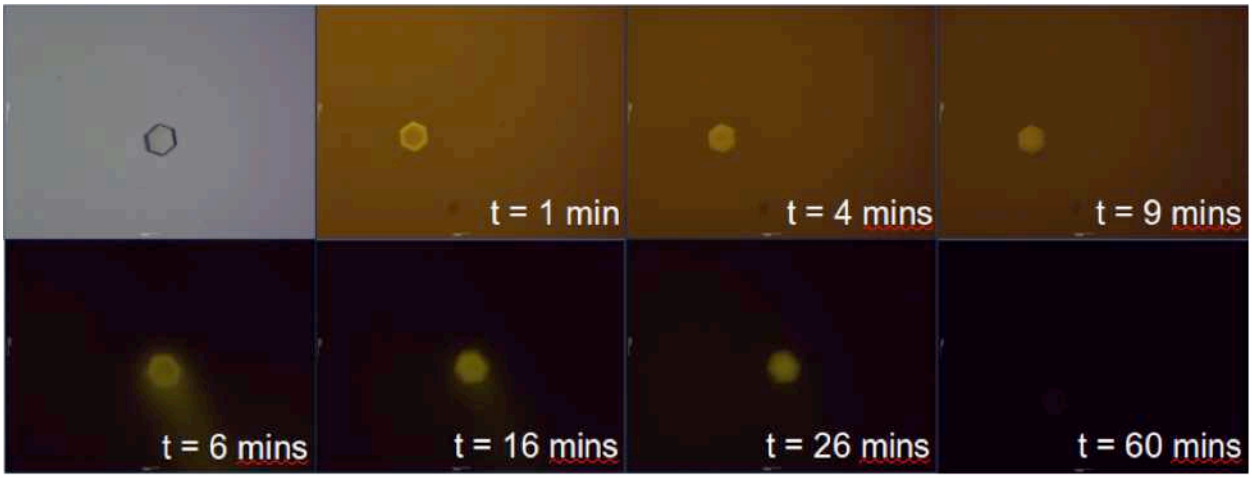


Figure 2.3 NHS-fluorescein tagged $Au_{25}$ loading

NHS-fluorsescein labeled gold nanoparticles loading (top row) and unloading (bottom row) from CJ protein crystal pores. The top left panel shows a brightfield transmission image of the CJ crystal prior in a storage buffer (1x PBS) prior to loading gold nanoparticles. The remaining panels are illuminated with 405 nm wavelength light.

However, these images do not account for photobleaching of the NHS-fluorescein. In some cases, after 24 hrs, the crystals still looked yellow under white light (Fig. 2.4), though they looked dark when illuminated with a 405 nm wavelength laser.

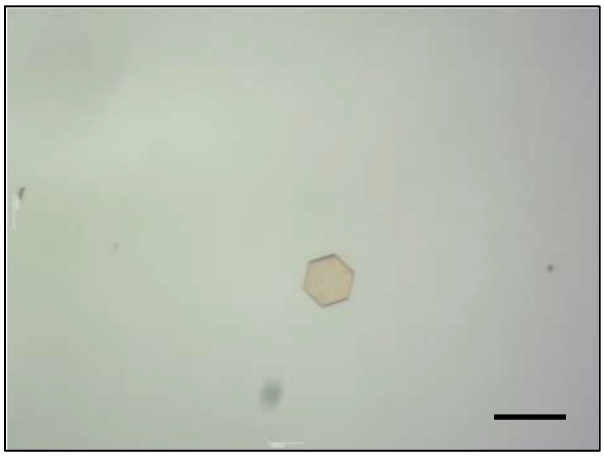

Figure 2.4 NHS-fluorescein unloading

Bright field optical transmission microscopy image of a CJ crystal previously loaded with NHS-fluorescein tagged $Au_{25}$ nanoparticles and placed in $H_2O$ for 24 hours prior to imaging. NHS-fluorescein labeled gold nanoparticles appear to stick strongly within the crystal pores for up to 24 hrs. An empty CJ crystal should look clear under white light, as shown in Figure 2.3. Scale bar is 100 μm.

In order to determine more accurately the diffusion patterns of $Au_{25}$ into and out of CJ crystal pores, we also directly imaged the unlabeled nanoparticles. $Au_{25}$ particles could be excited with a low power 405 nm laser pointer, and the emission (~700 nm) could be imaged through a 450 nm long pass filter from Edmund Optics.[105] Empty crystals have a blue background fluorescence, while crystals fully loaded with $Au_{25}$ clusters fluoresce red (Fig. 2.5).

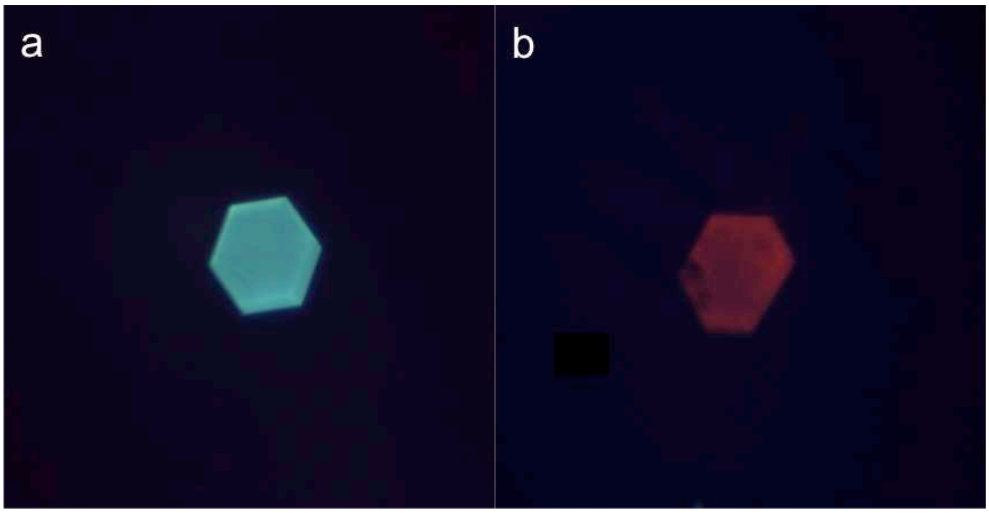


Figure 2.5 Visualizing $Au_{25}$ loading

CJ crystal excited with a 405 nm laser and image through a 450 nm longpass filter before (left) and after (right) loading $Au_{25}$. Scalebar is 100 μm.

Extensive trial and error testing was required to find conditions which encouraged diffusion, and even adsorption, of the gold nanoparticles into the crystal pores. For example, crystals that had not been "quenched" after crosslinking (by the removal of any remaining reactive aldehyde groups), were not able to load particles. We hypothesize this is because the primary amines on the glutathione ligands surrounding the gold nanoparticles can react with aldehyde groups on the surface of the crystal, thereby blocking the pores.

Additionally, there was some pH and salt dependence to loading; the optimum loading conditions were based on the buffers used for growth, crosslinking, and quenching the crystals (detailed later). Once we determined that crosslinked CJ crystals were able to load gold nanoparticles under certain conditions, we proceeded with attempts to immobilize the clusters within the crystal pores. A widely used method for binding Histidine-tagged proteins is through Nickel-NTA affinity.[106,107] The shared affinity

for Ni(II) binds a His-tag to a nitrilotriacetic acid (NTA) until the Ni(II) is chelated away (Fig. 2.6 & 2.7). In our case, $Au_{25}$ clusters could be ligand-exchanged to display an NTA group at the terminus of a 12-carbon chain. The CJ protein crystals contain C-terminal 6xHis-tags used in purification. Additionally, we crystallized a negative control CJ variant that does not contain His-tags.

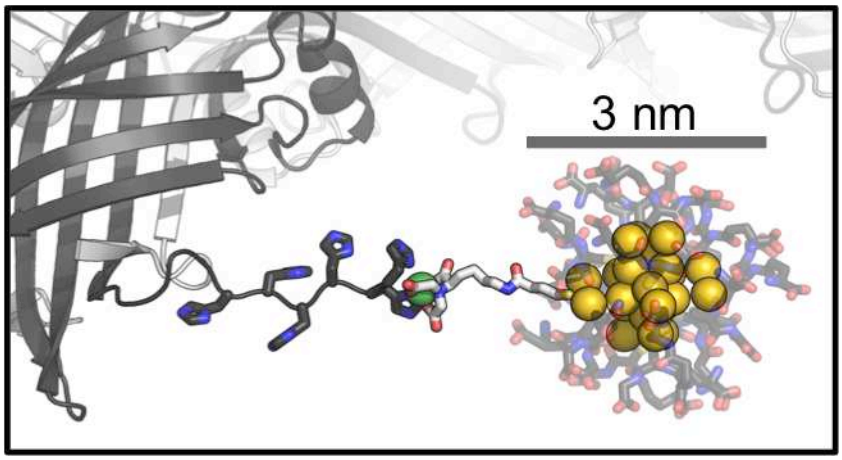


Figure 2.6 Rendering of the CJ-$Au_{25}$ attachment strategy

A nitrilotriacetic acid (NTA) ligand (light grey) on the $Au_{25}GSH_{17}$ cluster (yellow) chelates a divalent metal such as nickel (green). The His-tag (dark grey and navy) on the protein scaffold (dark grey) also coordinates the nickel ion, allowing for metal affinity immobilization of the gold clusters within the protein crystal pores.

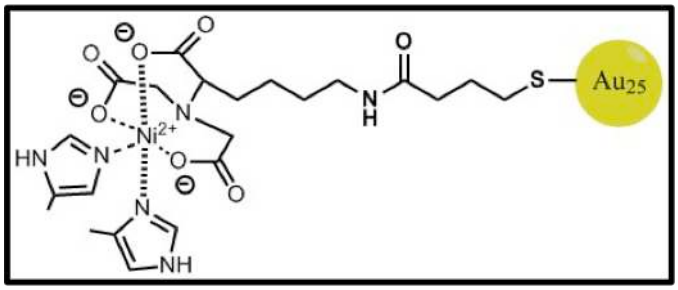


Figure 2.7 Schematic of the CJ-$Au_{25}$ attachment strategy

A more detailed look at the groups involved in the electrostatic attachment of gold clusters to CJ crystal His-tags.

Nanoparticles generally load into the crystals within about 30 minutes; however, the time it takes for the gold nanoparticle solution to completely penetrate the crystal varies with solution concentration and crystal thickness. Further efforts are underway to quantitatively characterize the diffusion of nanoparticles through crystal pores. For the purposes of these experiments, a standard loading time of 30 minutes was used, based on confocal microscopy data (detailed later).

Figure 2.8 shows a typical loading and unloading experiment with controls. Each panel contains a CJ crystal with (i) and without (ii) a His-tag. Panel (a) shows typical crystal fluorescence at the end of a 30 minute incubation in 1 mg/mL $Au_{25}(GSH)_{17}NTA$. Regardless of His-tag, crystals readily adsorb gold nanoparticles, becoming much brighter than the surrounding solution. Panel (b) shows the same crystals from panel (a) after transfer to 1 mM $NiSO_4$ and incubation for four days. The CJ crystal with a His-tag (i) retains $Au_{25}(GSH)_{17}NTA$ in the presence of Ni(II), while the crystal without a His-tag (ii) does not have affinity for the gold nanoparticles, and they diffuse into the Ni(II) solution. Panel (c) shows the same crystals after transfer to 0.1 M EDTA and incubation for 1hr. In the presence of excess metal chelator, even the CJ crystal with a His-tag (i) loses its affinity for the gold nanoparticles and they diffuse into the surrounding solution. Panels (d), (e), and (f) show the same series of solution changes, but in a gold nanoparticle solution that has not been ligand-exchanged to contain NTA moieties ($Au_{25}(GSH)_{17}$). Without the presence of an NTA, crystals do not retain affinity for the gold nanoparticles regardless of the presence of Ni(II) or His-tags. Additionally, if no Ni(II) is added during the experiment, $Au_{25}(GSH)_{17}NTA$ diffuses out of crystals with (i) and without (ii) a His-tag, even without the addition of EDTA (Fig. 2.9). Overall, Figure 8

and 9 demonstrate that the nanoparticle NTA, the scaffold His-tag, and Ni(II) all must be present to retain the nanoparticle within the crystal pore. Additionally, Figure 2.10 shows that this scheme of loading and unloading can be repeated without damaging the crystal or permanently trapping the particles. After the fifth repetition of loading and unloading, the crystal still fluoresces red and blue under a 405 nm laser.

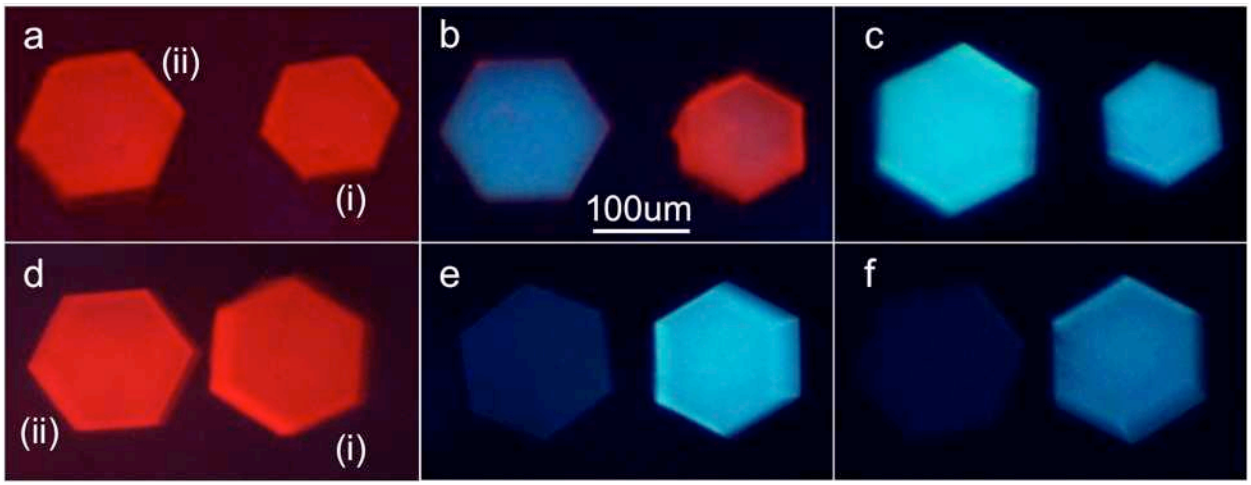


Figure 2.8 $Au_{25}$ immobilization controls

Each image contains a (i) CJ and (ii) CJΔH6 crystal. (a) At t = 30 in 1 mg/mL $Au_{25}(GSH)_{17}(NTA)$. (b)&(e) At t = 4 days in 1 mM $NiSO_4$ at pH 7.0. (c)&(f) At t = 1 hr in 0.1M EDTA at pH 7.0. (d) At t = 30 mins in 1 mg/mL $Au_{25}(GSH)_{18}$. Imaged with 405 nm laser and a 450 nm longpass filter.

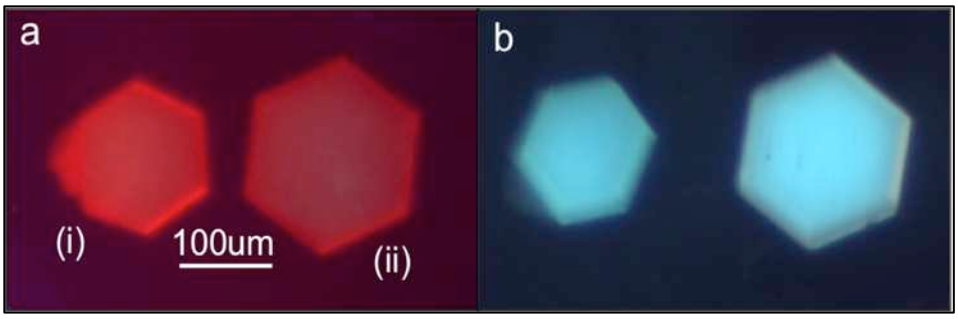


Figure 2.9 $Au_{25}$ immobilization control

Each image contains a (i) CJ and (ii) CJΔH6 crystal. (a) At t = 30 in 1 mg/mL $Au_{25}(GSH)_{17}(NTA)$. (b) At t = 1hr in 0.1M HEPES at pH 7.0. Imaged with 405nm laser and a 450 nm longpass filter.

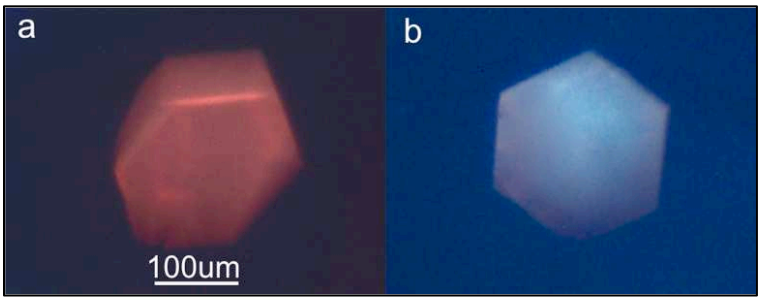


Figure 2.10 Loading and unloading repitions

A CJ crystal after the fifth repetition of loading (a) At t = 30 mins in 1 mg/mL $Au_{25}(GSH)_{17}(NTA)$. and unloading (b) At t = 1hr in 0.1M EDTA at pH 7.0.

*Confocal microscopy*

We used confocal laser microscopy to quantify loading of the crystals and confirm that the gold nanoparticle solutions penetrated the entire thickness of the crystals. All the confocal images were taken under identical optical settings and excited with a 561 nm diode laser. Imaging of a CJ crystal loaded with $Au_{25}(GSH)_{17}NTA$ for 30 minutes and incubated in 1 mM $NiSO_4$ for five days showed that gold nanoparticles were retained throughout the entire z-axis of the crystal. Figure 11 shows a z-stack series at 5 um increments from the top surface (left) to bottom surface (right) of the crystal. Figure 2.12 shows the corresponding fluorescence intensity at each position on the z-stack. After a five day incubation in Ni(II), gold was still loaded evenly throughout the crystal.

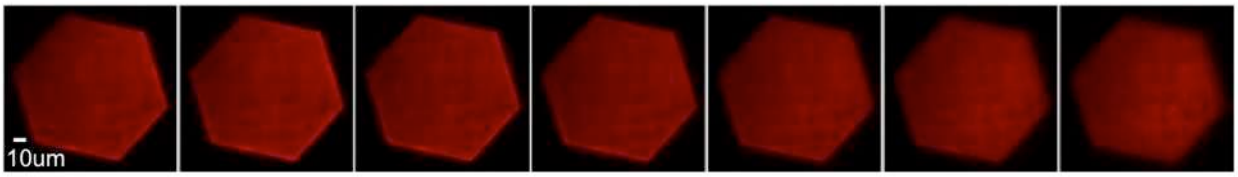


Figure 2.11 Confocal laser microscopy z-stack

Confocal laser microscopy z-stack through a CJ crystal loaded with $Au_{25}(GSH)_{17}NTA$ for 30 mins and bound with 1 mM $NiSO_4$ for five days. *Image: L. Hartje*

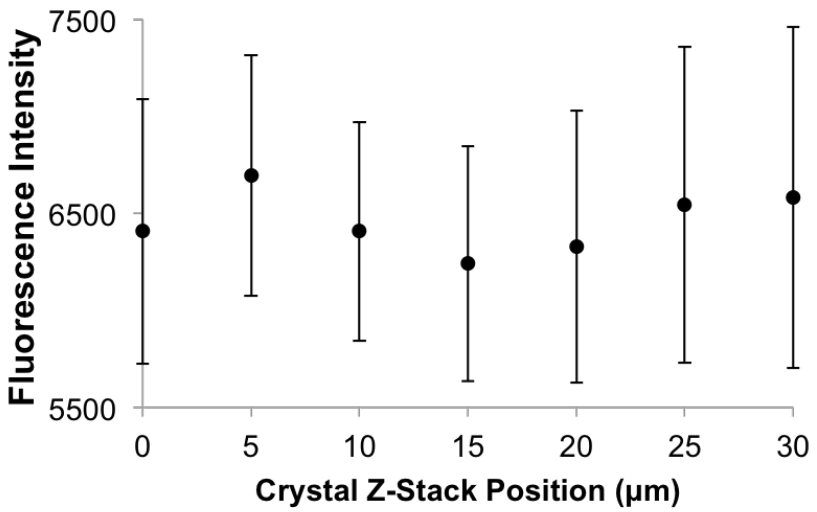


Figure 2.12 Fluorescence intensity through crystal

Fluorescence intensity of each position of the z-stack in Figure 2.11 as determined by the pixel intensity of the confocal laser microscope. *Image: L. Hartje*

In order to compare this data to the concentrations of the gold nanoparticle solutions used in loading, we created a fluorescence intensity standard curve for various concentrations of gold nanoparticle solutions. This standard curve could then be used to convert fluorescence intensities seen in the z-stack to solution concentrations (Fig. 2.13).

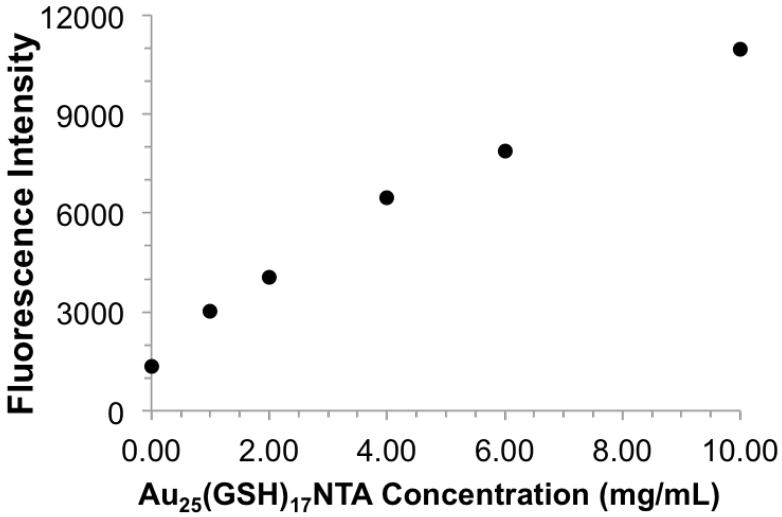


Figure 2.13 Standard curve

Gold nanoparticle solution concentration as a function of fluorescence intensity on the confocal laser microscope. *Image: L. Hartje*

We found that the gold nanoparticles were adsorbed at an average of 4.7 ± 0.7 mg/mL within the crystal pores. This concentration is roughly equivalent to one $Au_{25}(GSH)_{17}NTA$ cluster per very two unit cells. Even though the crystal adsorbed gold nanoparticles to almost five times the concentration in the surrounding solution (all crystals are loaded at 1 mg/mL $Au_{25}$), only about 1/24 of all His-tags bound a gold cluster (each unit cell has 12 His-tags)

*Elemental analysis*

Next, we further explored the quantification of gold nanoparticle loading under different conditions using elemental analysis services by Midwest Laboratories. For elemental analysis, samples were loaded with gold nanoparticles for specified times, the crystal dimensions were measured, and the samples were dissolved in aqua regia (1

part nitric acid: 3 parts hydrochloric acid). Aqua regia is capable of dissolving the gold clusters, so the mass of Au present can be measured. Calculating the volume of each crystal used allowed us to directly compared with the mass of gold per volume found in confocal laser microscopy.

Elemental analysis confirmed strong adsorption of gold nanoparticles into the crystal pores. Figure 2.14 shows the number of gold atoms per unit cell in the various samples. The first sample, empty crystals, serves as a negative control. The next sample, crystals loaded with $Au_{25}(GSH)_{17}NTA$ for five minutes before dissolving in aqua regia, shows few gold atoms per unit cell. Crystals were also loaded for 30 mins, 1 hr, 8 hrs, 24 hrs, and 48 hrs. At the most concentrated timepoints, 24 and 48 hrs, elemental analysis suggests an average of 12 nanoparticles per unit cell of the crystal. This corresponds to a 118.5 mg/mL concentration *in crystallo*.

For samples loaded with $Au_{25}(GSH)_{17}NTA$ for 30 minutes, then placed in 1 mM $NiSO_4$ for 1 hour before dissolving in aqua regia, the number of gold atoms per unit cell was slightly lower than for crystals simply soaked in gold nanoparticles for 30 minutes. The last samples were loaded with $Au_{25}(GSH)_{17}NTA$ for 30 minutes, then placed in 0.1 M EDTA for 1 hour before dissolving in aqua regia. These samples showed negligible gold atoms retained in the crystal pores.

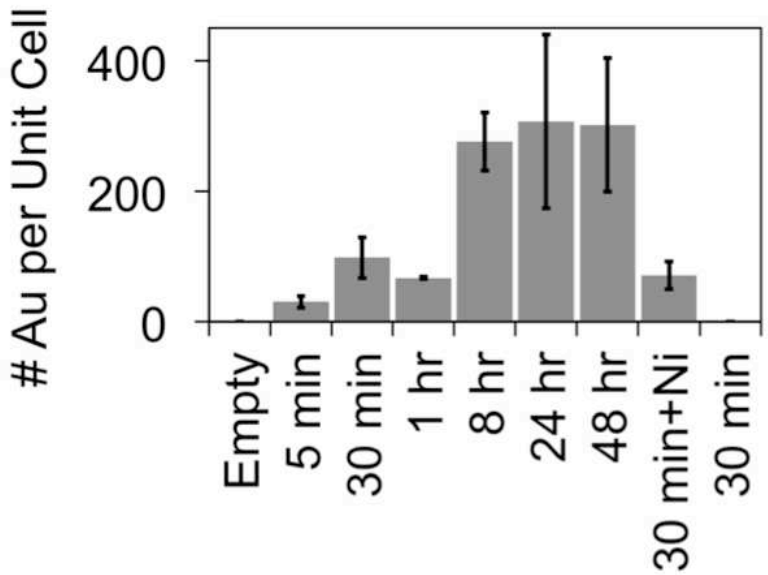


Figure 2.14 Elemental analysis

Number of Au atoms per unit cell of crystal as determined by elemental analysis. Crystals underwent the following treatment: none; $Au_{25}$ loading for 5 min, 30 min, 1 hr, 8 hr, 24 hr, or 48 hr; $Au_{25}$ loading for 30 min followed by 1 hr of Ni(II) entrapment; or $Au_{25}$ loading for 30 min followed by 1 hr EDTA unloading. Error bars show standard deviation of three replicates.

*Theoretical loading analysis*

Some analysis was performed to compare the quantified gold nanoparticle loading data from confocal laser microscopy with that of elemental analysis and theoretical calculations (Fig. 2.15). Although each unit cell of the crystal is 1411.8 $nm^3$, 273 $nm^3$ of that are excluded from solvent (giving the crystal it's 80.6% solvent content). A further 306 $nm^3$ are excluded from probes with volume equal to that of $Au_{25}(GSH)_{17}NTA$. Therefore, each unit cell of a CJ protein crystal contains about 833 $nm^3$ of volume accessible to the gold nanoparticles.

This information was used to calculate the expected concentration of gold nanoparticles per unit cell if pure diffusion was the cause of crystal loading. This value, 0.1 $Au_{25}$ cluster per unit cell, is well below the concentration for even the shortest loading time measured by elemental analysis; the five minute loading time gives an average of 1.2 $Au_{25}$ per unit cell. Adsorption to the crystal could account for the increased concentrations within the pores. After 48 hours of loading, elemental analysis results in an average of 12 $Au_{25}$ per unit cell, which is comparable to the theoretical concentration expected if the gold nanoparticles were closely adsorbed to the entire wall of the crystal pore (~17 $Au_{25}$ per unit cell).

Lastly, comparisons between concentrations calculated by elemental analysis and confocal laser microscopy fluorescence intensity standard curves follow a logical trend. The CLM data was collected after loading $Au_{25}(GSH)_{17}NTA$ and then allowing the crystal to sit in a Ni(II) solution for five days, the most rigorous test of the histag-Ni(II)-NTA binding. The crystal's fluorescence shows gold nanoparticle retention throughout, but the concentration of gold (0.5 $Au_{25}$ per unit cell) is less than that determined by elemental analysis. When a crystal is simply soaked in a gold nanoparticle solution for 30 minutes, elemental analysis results in an average of 4 $Au_{25}$ per unit cell. However, when the middle ground is tested (30 minutes of loading, followed by 1 hr of soaking in Ni(II)), elemental analysis gives ~2.5 $Au_{25}$ per unit cell.

Interesting future experiments may include further quantification the diffusion of gold nanoparticles through crystal pores in the presence or absence of Histags, NTA, and Ni(II). Although dissociation constants for single-his-tag-Ni(II)-NTA interactions

exist,[108,109] more CLM and elemental analysis data would help us move towards a robust diffusion model for gold nanoparticles within protein crystal scaffolds.

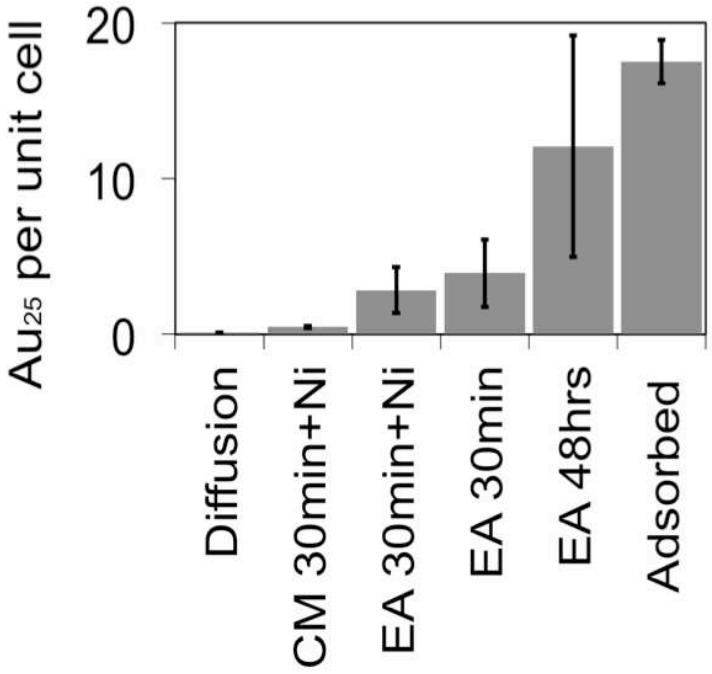


Figure 2.15 Elemental and theoretical loading analysis

Comparing the number of $Au_{25}(GSH)_{17}NTA$ clusters expected per unit cell of the crystal under various conditions. From left to right: Given pure diffusion into the crystal pores in a gold nanoparticle solution of 1 mg/mL. As measured by confocal microscopy (CM) after loading for 30 mins and releasing in the presence of Ni(II) for 5 days. As measured by elemental analysis (EA) after loading for 30 mins and releasing in the presence of Ni(II) for 1 hr. As measured by EA after loading for 30 mins. As measured by EA after loading for 48 hrs. As expected if gold nanoparticles were to adsorb to the wall of the crystal pore throughout the unit cell.

*X-ray diffraction*

Crystal quality after crosslinking and $Au_{25}(GSH)_{17}(NTA)$ loading and unloading was assessed by single crystal x-ray diffraction (Fig. 2.16). CJ crystals were prepared using standard protocol and loaded with 1 mg/mL gold nanoparticles for 30 minutes. After loading, one crystal was unloaded in the presence of 0.1 M EDTA pH 7.0 for 30

minutes. Both crystals were briefly swished through a cryoprotectant solution containing 100% mTacsimate$^{TM}$ and 10% glycerol at pH 7.5 prior to flash freezing in a liquid nitrogen stream (T=100 K). Crystal integrity was determined via a 10 frame (0.5$^{o}$/frame, 60 second exposure) data collection strategy on a local Rigaku Compact HomeLab with a micro-focus X-ray generator and a Pilatus 200K detector. Crystal diffraction was retained to ~4.2 Å resolution with 1.2° mosaicity. Retention of crystal integrity after full loading of gold nanoparticles indicated that the CJ protein crystal nanopores remained intact and provided a robust scaffold for reversible, site-specific gold nanoparticle capture.

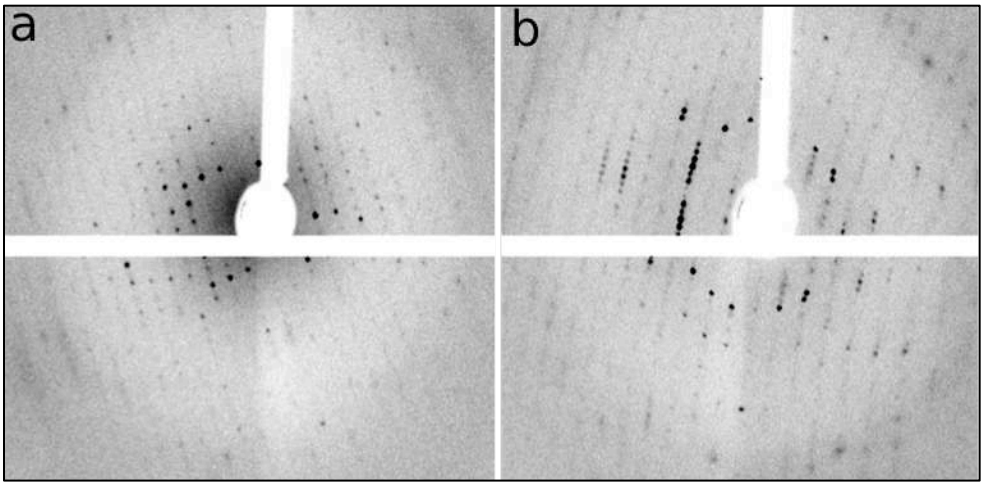


Figure 2.16 X-ray diffraction

X-ray diffraction images of CJ crystal after incubation in (a) 1 mg/mL $Au_{25}(GSH)_{17}$(NTA) for 30 min, followed by (b) 0.1 M EDTA at pH 7.0 for 30 min. *Image: T. Huber*

However, $Au_{25}(GSH)_{17}$(NTA) was not visible in the XRD electron density map. A more robust crosslink and loading method was attempted, allowing the crystals to load $Au_{25}$ clusters for two hours. At this time, the crystals appeared to have highly concentrated the gold nanoparticle solution, but no obvious peak corresponding to

ordered gold nanoparticles was seen after refinement of the structure. This result is consistent with the nanoparticles adopting heterogeneous positions within the crystal. In order to resolve the gold nanoparticle structure on the protein crystal scaffold, further efforts are underway. Specifically, we will attempt to replace the histag:NTA interaction motif with capture motifs that have fewer degrees of freedom.

*Solution-dependent gold loading*

Lastly, we investigated the effects of crosslinker, quench, and pH on the loading of $Au_{25}$ clusters in CJ pores. In Figure 2.17, each panel contains one CJ crystal grown, crosslinked, and quenched by the standard glyoxal/Tadsimate™ method and one CJ crystal grown, crosslinked, and quenched by the standard $AmSO_4$/EDC method. In each panel, the larger crystal is glyoxal-crosslinked and the smaller crystal is EDC-crosslinked.

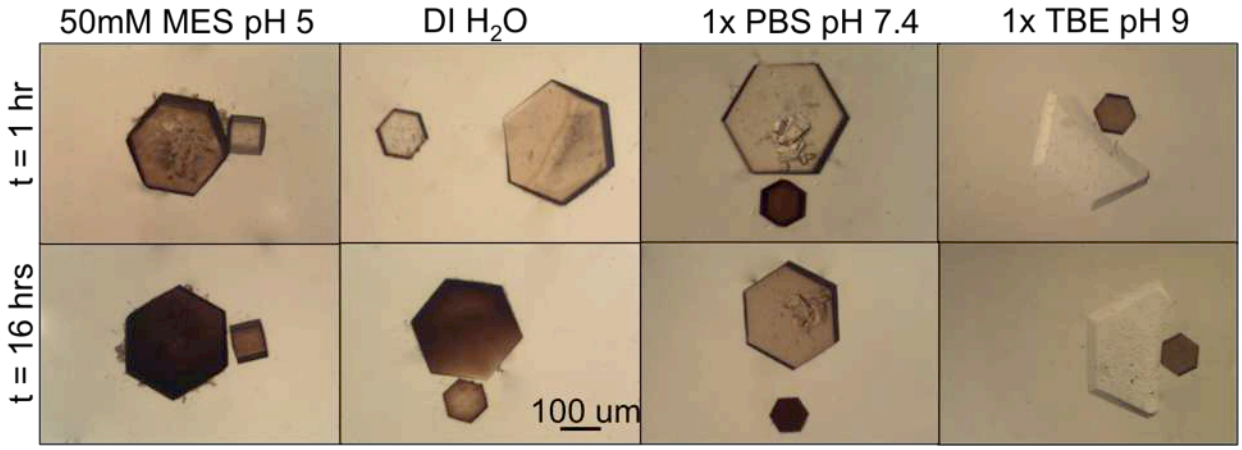


Figure 2.17 Solution-dependent $Au_{25}$ loading

$Au_{25}$ adsorption into crystals depends on buffer solution and crystal preparation conditions. Each panel contains one EDC crystal (small) and one glyoxal crystal (large), loading $Au_{25}(GSH)_{17}NTA$ in various buffers.

At higher pH, glyoxal crosslinked crystals do not load $Au_{25}$ overnight, but EDC crosslinked crystals do. At lower pH, glyoxal crosslinked crystals seem to adsorb more $Au_{25}$ than EDC crosslinked crystals. The presence of a buffer or salt seems to increase loading of $Au_{25}$ into EDC crosslinked crystals, whereas the opposite seems to be true with glyoxal crosslinked crystals when comparing water loading and PBS loading. Additionally, it is important to note that $Au_{25}(GSH)_{17}NTA$ will be less soluble at pH 5.0, because there may be interactions between the -COOH and $-COO^-$ groups. This can be seen in the aggregation in the far left panels.

The isoelectric point (pI) of an uncrosslinked CJ crystal is 8.55. The isoelectric points of both glutathione and nitrilotriacetic acid, the $Au_{25}$ ligands, are approximately 4.75. After glyoxal crosslinking, primary amines have been converted to either secondary amines (by DMAB) or oximes (by hydroxylamine). This removes some positive charges from the crystal surface, potentially making the crystal more negatively charged. The addition of salt, especially in the 1xPBS experiment, should mitigate the effects of those electrostatic interactions between scaffold and nanoparticle.

It’s difficult to draw conclusions from these types of experiments, as variables include pH, salt concentration, crystal growth conditions, crystal crosslinking, crystal quenching, nanoparticle preparation, and nanoparticle concentration. However, we have significant control over adsorption into the scaffold; depending on the desired application, conditions can be chosen which promote adsorption, passive diffusion, or exclusion of a guest from the crystal pores.

## CONCLUSIONS

We have immobilized gold nanoparticles using precisely spaced motifs within an array of 13 nm nanopores delimited by a highly porous (80% solvent) protein crystal. Scaffold formation was robust, and crystals could be grown and crosslinked with and without His-tags. Confocal microscopy indicated long-term, Ni(II) dependent capture throughout the entire thickness of the crystal. Elemental analysis confirmed increasing adsorption of gold nanoparticles within the protein crystal pores over time, as well as removal upon addition of EDTA. Both elemental analysis and fluorescence intensity from confocal microscopy show that gold nanoparticles are absorbed into the crystal beyond concentrations expected through pure diffusion. The attachment is specific and reversible, and the protein crystal retains x-ray diffraction quality throughout loading and unloading of nanoparticles.

To our knowledge, this report is the first example of successful, controlled adsorption of larger nanoparticles into pre-existing protein crystals. These arrays may find applications in sensors, catalysis, energy storage devices, and other nanoelectronics. They may also be used to further study the interesting and unique plasmonic properties of gold nanoparticles. Additionally, they will serve as the nucleation points for templated nanorod growth, as discussed in Chapter III.

Compared to the lithographic or synthetic templating methods described in the introduction, our porous protein crystal templating method is more easily designable for a variety of three dimensional arrays. Synthesis may also be faster and cheaper than with other methods. However, confirmation of the precise placement of particles within

the pores must be confirmed with x-ray diffraction and may require a more rigid capture strategy.

## EXPERIMENTAL

### *Reagents*

The following chemicals were purchased from Sigma-Aldrich and used without further purification: Gold (III) chloride trihydrate (HAuCl4, ≥49.0% Au basis), L-glutathione reduced (GSH, ≥98.0%). The following chemicals were purchased from TCI America and used without further purification: Nε -carbobenzoxy-L-lysine (Nε -Cbz-L-lysine, >98.0%). Other reagents were purchased from Alfa Aesar, Thermo Scientific, and Sigma-Aldrich and used without further purification. Lithium sulfate (Li2SO4, ≥98.5%). Trimethylamine N-oxide (TMAO, ≥98%). Hydroxylamine solution (50 wt. % in H2O). A blend of 1.83M malonic acid, 0.25M sodium citrate, 0.12M succinic acid, 0.3M D-L malic acid, 0.4M acetic acid, 0.5M sodium formate, and 0.16M sodium tartrate was titrated to pH 7.5 using sodium hydroxide, and was used in crystallization and crosslinking. This is a modified blend of TacsimateTM from Hampton Research and is referred to as mTacsimateTM throughout the paper. The modification removes ammonium from the solution, which contains primary amines that interfere with protein crystal crosslinking.

*Protein crystal preparation*

Periplasmic protein (Genebank ID: cj0420, Protein Data Bank code: 2fgs) from *Campylobacter jejuni* was selected from a scan of the Protein Data Bank for proteins that crystallize with large pores (Fig. S1). It was expressed in pSB3 in *E. coli* BL21 (DE3) pLySs using a glucose/lactose induction system at 17 °C for 36 hours. The cells were lysed by sonication and purified via immobilized metal affinity chromatography. Purified protein was buffer exchanged into 150 mM NaCl, 10 mM HEPES, and 10% glycerol at pH 7.5. A variant of CJ was cloned to insert a tobacco etch virus (TEV) protease cleavage site between the protein and an N-terminal hexahistidine tag. After initial purification and buffer exchange, this protein was incubated with TEV protease (1:100 $OD_{280}$) overnight at 4 °C. Following TEV cleavage, the protein was reverse purified by immobilized metal affinity chromatography to remove TEV and uncleaved protein. The purified protein was characterized with SDS-Page (Fig. S2). After crystallization, crosslinking, and washing, the crystals retained smooth, hexagonal morphology and clear color.

*Gold nanoparticle synthesis*

Glutathione (308.1 mg, $1x10^{-3}$ mol) was added to a solution of $HAuCl_4$ (98.7 mg, $2.5x10^{-4}$ mol) in 50 mL methanol. The solution was stirred to combine. The solution was initially a cloudy, yellow suspension, which after approximately five minutes of magnetic stirring turned to a clear and colorless solution. This solution was cooled at 0 °C while stirring for 30 minutes. To this, a solution of $NaBH_4$ (94.3 mg, $2.5x10^{-3}$ mol) in 12.5 mL ice $H_2O$ was added rapidly with stirring. The reaction was allowed to stir for one hour at

room temperature before the precipitate was spun down in 200 µL of 5 M $NH_4OAc$ and MeOH at 4000 rpm. The supernatant was discarded and the precipitate was washed twice more in the same conditions and then dried. Gel purification was performed on $Au_{25}(GS)_{18}$ on a 24% polyacrylamide gel (Fig. S3). $Au_{25}(GS)_{18}$ was extracted from the gel in $H_2O$ and precipitated in MeOH and 200 µL of 5 M $NH_4OAc$ and dried.

(1S)-N-(5-Carbobenzyloxyamino-1-carboxypentyl) iminodiacetic Acid (2). Briefly, bromoacetic acid (4.17 g, 0.03 mol) was dissolved in 15 mL of 2 M NaOH. This solution was cooled to 0 ºC. To this a solution of $N^{\varepsilon}$-Cbz-L-lysine (4.2 g, 0.015 mol) in 22.5 mL of 2 M NaOH was added drop by drop and stirred for two hours at 0 °C. Stirring was continued overnight at room temperature. This solution was then heated to 50 °C for two hours, after which, 1 N HCl (45 mL) was added to the cooled solution. The precipitate was filtered and dried, to afford 1.5776 g of a crude white solid (2, triacid).

(1S)-N-(5-Amino-1-carboxypentyl)iminodiacetic Acid (3). A solution of 2 (6.8 g, 0.017 mol) in 95 mL MeOH/5 mL $H_2O$ and a spatula tip full of 5% Pd/C catalyst was stirred with $H_2$ at 25 °C for 24 hours. Product was filtered through celite to remove the catalyst. The solvents were evaporated to give a colorless white paste.

(1S)-N-[5-[(4-Mercaptobutanoyl)amino]-1-carboxypentyl]iminodiacetic Acid (HS-NTA). The amino derivative (3, 1 g, 0.0038 mol) was dissolved in 10 mL $H_2O$ with $NaHCO_3$ (1 g, 0.0119 mol) and 4-butyrothiolactone (0.6 g, 0.0059 mol) and stirred for 15 hours at 72 °C. The resultant mixture was acidified to pH 3 with acetic acid and concentrated under reduced pressure. The crude product was crystallized in absolute ethanol, filtered and washed in absolute ethanol followed by pentane, and dried under vacuum to give a light beige solid (Scheme S1).

Ligand Exchange of $Au_{25}(GS)_{18}$. To dried and purified $Au_{25}(GS)_{18}$, five equivalents of HS-NTA was added and was dissolved in $H_2O$. The reaction was allowed to shake for 7.5 minutes.[5] The product was then precipitated out in methanol and 200 µL of 5 M $NH_4OAc$. Post centrifugation, the precipitate was dried under reduced pressure.

*Imaging*

All nanoparticle uptake and release was carried out at room temperature with 10 µL samples of 1 mg/mL $Au_{25}$ solution (with or without ligand exchange) in 50 mM MES at pH 5.0. Diffusion images were captured by exciting the particles with a low power 405 nm laser pointer and imaging the emission through a 450 nm longpass filter from Edmund Optics. Images of the $Au_{25}(GSH)_{17}(NTA)$ fluorescence standards and crystal z-stack in Fig. 3 were taken using an Olympus IX81 spinning-disk confocal microscope with Photometrics Cascade II camera, a 20×/0.5 numerical aperture objective with a 1x magnification changer, and Phasor holographic photoactivation system (Intelligent Imaging Innovations [3i], Denver, CO). Excitation was performed with a 561 nm diode laser and 692 ± 12.5 nm single bandpass emission filter to eliminate spectral crossover. Images were acquired and analyzed with SlideBook 6.0 software [3i]. To repudiate intrinsic crystal fluorescence, an empty crosslinked CJ crystal was imaged under the optical conditions used in Fig. 3 and found to exhibit average fluorescent intensity comparable to the 0 mg/mL $Au_{25}(GSH)_{17}(NTA)$ standard. For x-ray diffraction, crystals were protected in 50% mTacsimate™ and 22% TMAO at pH 7.5. A compact Homelab Rigaku with a microfocus X-ray generator and a Pilatus 200K detector was used at 60 second exposure and 93 mm detector distance.

*X-ray data processing*

CJ crystals were prepared using standard protocol and loaded with 1 mg/mL gold nanoparticles for 30 minutes. After loading, a similar crystal was unloaded in the presence of 0.1 M EDTA pH 7.0 for 30 minutes. Both crystals were briefly swished through a cryoprotectant solution containing 100% mTacsimate$^{TM}$ and 10% glycerol at pH 7.5 prior to flash freezing in a liquid nitrogen stream (T=100 K). Crystal integrity was determined via a 10 frame (0.5$^{o}$/frame, 60 second exposure) data collection strategy on a local Rigaku Compact HomeLab with a micro-focus X-ray generator and a Pilatus 200K detector. Data was integrated and scaled using HKL3000 program suite and resolution estimated to 4.26 Å after loading in gold nanoparticles and 4.27 Å after unloading in EDTA.

To attempt to resolve a CJ gold nanoparticle co-structure, a more robust crosslinking method was performed. CJ crystals were grown at concentration of 10 mg/mL in 3.4 M $(NH_4)_2SO_4$, 0.1 M Bis-Tris at pH 7.0. Crystals were transferred to a well containing 3.2 M $(NH_4)_2SO_4$, 1 mM EDTA, 10% glycerol, 50 mM Bis-Tris at pH 6.5 and allowed to wash for 30 minutes. Crystals were then transferred to an amine free crosslinking solution containing 5 M TMAO, 0.5 M LiSO4, pH 7.5 (5T05L) and allowed to wash for 30 minutes. Crystals were crosslinked by transferring to 5T05L containing 1% glyoxal and incubating for 4 hours. Reductive stabilization of crosslinks was performed by a 30 minute incubation in 5T05L supplemented with 100 mM DMAB. After reduction, free aldehydes were quenched and reduced by addition of 50% hydroxylamine solution to 100 mM and incubating for 30 minutes.

Crystals were loaded for 2 hours with gold nanoparticles under standard conditions. Visually, the resulting crystals appeared to have significant uptake of the gold nanoparticles (i.e. they turned red). Loaded crystals were swished through a cryoprotectant solution containing 5T05L prior to flash freezing in a liquid nitrogen stream. A full data collection set (360 frames, 0.5$^{o}$/frame, 60 second exposure) was collected on the local Rigaku HomeLab. The data was reduced and integrated using iMosflm,[6] scaled using Pointless.[7] Molecular replacement was performed using Refmac[8] with 2FGS from the PDB as a starting model. X-ray diffraction data and refinement statistics are provided in Table S3 of the Appendix.

Refinement of ambiguous electron density was kept conservative given the resolution. One strong, large, unmodeled electron density peak is between symmetry copies of Lys111 that could represent a glyoxal crosslinking product. It is difficult to model atoms here due to the 2-fold symmetry axis and the lack of chemical details about the crosslinking end product. The next largest unmodeled peak is, similarly, likely due to crosslinking at the interface that contains two Lys95 sidechains and two Lys98 sidechains. The next largest peak is the N-terminus, where fraying results in ambiguous electron density. Finally, a large peak is near the end of a possible ligand bound to the interior of the CJ barrel (CJ is a putative isoprenoid binding protein) that was here crudely modeled as an unsaturated alkane. Despite the 2 hr gold nanoparticle loading, after refinement there was no obvious peak corresponding to ordered gold nanoparticles in the porous structure of CJ.

*Elemental analysis*

The elemental analysis samples each consisted of three replicates, each containing three crystals loaded with gold nanoparticles and dissolved in 2 mL of aqua regia. Volumes were calculated by measuring side lengths and heights of the crystals. The first seven samples consisted of loading CJ crystals with $Au_{25}(GSH)_{17}(NTA)$ for the described length of time. For the eighth sample, CJ crystals were loaded with $Au_{25}(GSH)_{17}(NTA)$ for 30 minutes, then moved to a drop of 1 mM $NiSO_4$ in 20 mM HEPES pH 8.0. In the ninth sample, CJ crystals were loaded with $Au_{25}(GSH)_{17}(NTA)$ for 30 minutes, then moved to a drop of 0.1 M EDTA in 20 mM HEPES at pH 8.0. Elemental Analysis was performed at Midwest Laboratories, Inc.

# CHAPTER 3. PROTEIN CRYSTALS AS SCAFFOLDS FOR GOLD NANOROD GROWTH[†]

## SYNOPSIS

Precise and programmable bottom-up synthesis of inorganic nanoparticles represents a grand challenge of inorganic materials synthesis. Such structures are applied in nanomedicine, electronics, photonics, imaging, and sensing. Here we show that a protein crystal can serve as a scaffold to direct the growth of high aspect ratio gold nanorods. Nanorod growth is further controlled by the presence of pre-defined nucleation points within the crystal. The resulting structures can be released from the protein matrix.

## INTRODUCTION

### *Properties of anisotropic gold nanostructures*

A grand challenge in inorganic nanoparticle synthesis is the production of asymmetric, three-dimensional nanoparticles. While gold nanospheres and their arrays have many applications, anisotropic particles may be of even greater interest. Because of their reduced symmetry, these particles have more than one plasmon band and the energy differences between the resonance frequencies associated with the bands can

[†] Kowalski, A., Nemeth, R., Zintgraff, S., Sloan, S., Huber, T., Ciesielski, P., Ackerson, C., and Snow, C. *ACS Nano.* Under review. 2018.

be different. In fact, the higher the aspect ratio (the ratio of long to short axis of a rod or cylinder), the larger the energy separation between bands. Absorbance at a lower wavelength (around 500 nm) comes from the oscillation of electrons perpendicular to the long axis and is called the transverse plasmon absorbance, whereas the absorbance along the long axis happens at a higher wavelength and is called the longitudinal plasmon absorbance.[34] At the highest aspect ratios, the longitudinal plasmon resonance can move up to 1200 nm (the near-infrared range), which is important for biomedical applications as those wavelengths allow for the highest transmission through tissues.[110]

There is an almost linear correlation between the surface plasmon longitudinal band position and the aspect ratio, so small changes in aspect ratio can lead to large changes in color transmission. Additionally, color change occurs when gold nanorods are placed in solutions of varying refractive index. Gold nanospheres are less sensitive to those dielectric properties, because it is the longitudinal axis of the rod that increases absorption wavelength and range in increasingly dielectric media.[10]

Additionally, as with ligand coatings on gold nanospheres, any shell layer can have a plasmonic effect on a gold nanorod if the refractive index of the shell layer is different than that of the surrounding solution. Gold nanorods may be coated with a shell simply to protect two or more rods from aggregation and to increase dispersion, or for reasons relating to their application. For example, if a gold nanorod is coated in an antibody ligand layer, it will undergo a red-shift in the presence of an antigen, because the antigen will have a higher refractive index than the surrounding water or cell media.[111]

A recent study by Funston *et. al.* elucidated some of the relationships between pairs of gold nanorods at distinct orientations to one another. These orientations had a large effect on plasmonics where rods aligned end-to-end are red shifted while rods aligned side-to-side are blue shifted. The group additionally found that rods aligned at T-shaped junctions do not function well as waveguides; the energy transfer from the longitudinal mode of one rod is weak towards the transverse mode of the other rod. Conversely rods aligned in an L-shape geometry have strong coupling and plasmon resonance through the entire structure.[38]

Gold nanorods in solution can be aligned parallel to one another, in which case only the transverse or longitudinal band can be specifically excited. These bands can be tuned by manipulating the coupling between rods and the polarization of applied light.[112] The light scattering and extinction by non-spherical gold particles is complex. These properties been studied computationally/theoretically[113,114] and solved numerically[115,116], as analytical solutions are only feasibly when elliptical shapes are assumed. Only recently has there been significant effort in understanding the theory behind the optical properties of many distinct gold nanostructures, and their experimental confirmation is sometimes still hindered by lack of control of nanoparticle shape in three dimensions[116].

*Applications for gold nanorods and other gold nanostructures*

Like spherical gold nanoparticles, these anisotropic structures have many applications in sensors, solar cells, biological imaging, electronics, energy storage devices, and cancer therapies. Many applications are in biology and medicine,[117] as several studies have shown a lack of cytotoxicity resulting from injection of gold

nanorods into human cells.[118] Most nanorods used in medical applications are coated with polyethylene glycol to improve biocompatibility and resistance to protein adsorption in solution.[110] Because of gold nanorod's extreme plasmon sensitivity to changes in the local environment, they can function as sensors. For example, gold nanorods of different aspect ratios and coated with mercaptoundecanoic acid can bind antibodies. The nanorod plasmon band red shifts after this binding event, and nano- or even femto-molar detection limits are possible.[118]

Nanorods can also be conjugated to DNA for a variety of sensing applications. By attaching its complementary single-strand of DNA to a gold nanorod, researchers were able to detect the HIV-1 *gag* gene at concentrations as low as 100 pM. This response was very specific; even single base-pair mismatches would not give the same scattering. This area of research is especially interesting because the response is orders of magnitude more sensitive than comparable colorimetric assays for the same applications.

Other biomedical applications, similar to those of gold nanospheres, include tracking, imaging, drug delivery, and photothermal therapeutics.[118] One current area of research is in appropriate conjugation techniques for attaching biomolecules to nanorods, as surface modifications are required for almost every medical application. Most biological applications will require ligand exchange or covalent bonding either with thiolated biomolecules or coupling of a carboxyl group via carbodiimide crosslinking. Quicker and cheaper methods, like electrostatic adsorption or surface coating, may be desirable but long-term stability *in vivo* must be studied in more detail.[119]

A wide range of catalytic applications have emerged for gold nanorods. The mechanisms for many of these reactions are still not fully understood. The sharp edges and corners in anisotropic particles allow for more surface active sites.[120] Researchers believe that rod-shaped particles have high-energy facets that, when made available for reactions, allow rods to be even more efficient than spherical particles in oxidizing CO. The same goes for reduction reactions, in which anisotropic gold is even more favored.[121]

Photocatalytic reactions are some of the most interesting for anisotropic gold particles. The promise of splitting water, producing fuels, reducing greenhouse gases, and removing organic pollutants through solar energy driven reactions could provide many advantages for our society. Of particular interest are gold nanorod-coated titanium oxide sheets. Supported gold catalysts can perform photo-oxidation for the production of chemicals and medicines, and the degradation of pollutants. Highly branched and porous gold structures supported on gold or other electrodes are also useful for electrocatalysis, with increasingly anisotropic morphologies performing better.[121]

Other applications for gold nanorods including negative index materials, invisible cloaking *a la* Harry Potter, waveguides, SERS, and nanoelectrodes.[117,120,122] All these applications require control over spacing between rods, aspect ratio, and orientation.[120]

*Synthesis of gold nanorods*

The study of the synthesis of gold nanorods began as recently as 2001 when Jana *et. al.* introduced the seed-mediated approach for growth.[123] Since then, many groups have struggled with characterizing the growth mechanism of these rods and

other anisotropic particles. Broadly, growth requires some soluble gold precursor solution containing gold ions and a reducing agent. Additives include a gold seed particle to induce growth, a capping agent to control the size of the resulting particles, or a surfactant to direct growth in certain directions. A recent study of the seed-mediated growth mechanism of gold nanorods in a hexadecyltrimethylammonium bromide (CTAB) solution divided growth into five stages:[124]

(1) Seed particles, originally ~1.2 nm in diameter, grow isotropically to diameters of ~6 nm by reduction of chloroauric acid with ascorbic acid. (t = 2 mins)

(2) CTAB micelles form on {100} facets of the growing sphere faster than on the {111} facets, which arrests growth in those directions. A modeling study showed that {111} facets have the highest internal energy of adsorption of CTAB onto gold. The particles continue to grow but only on the exposed {111} facets at the top and bottom. (t = 5 mins)

(3) Growth occurs rapidly at the boundary between exposed {111} facets and micelle-aggregated {100} and {110} facets, creating a dumbbell shaped rod. (t = 20 mins)

(4) Growth slows dramatically as gold precursor and ascorbic acid are consumed and CTAB rearranges to smoothly cover the surface, blocking Au(0) from the growth solution. (t = 45 mins)

(5) The rod rearranges itself into a more thermodynamically stable shape, consisting of an octagonal cross-section with rounded, hemispherical ends. (t = weeks)

Although this is just one example, it highlights the general mechanism by which gold nanorod growth occurs in solution. It has been suggested that this synthesis protocol actually produces petahedrally-twinned nanorods; their ends are pentahedra-

shaped and their cross-sections are pentagons. The use of silver nitrate in the growth solution can remove this twinning phenomenon to produce single-crystal rods with octagonal cross-sections. However, pentahedrally-twinned nanorods have been grown to much higher aspect ratios, with lengths up to 1 um and diameters between 20 and 22 nm.[125] Additionally they typically have a better-defined crystallographic structure. However, their limiting factor is often their shape-yield purity, which is lower than 30%.[126]

Researchers found that using CTAB-capped instead of citrate-capped seeds increased the uniformity of the resulting rods and decreases the presence of spherical particles to less than 5%.[127] Overall, it is known that bromide, silver, ascorbate, and the $CTA^+$ cation all play a role in binding various facets of the growing gold, which affects of deposition rate of new gold onto those faces and thereby the overall shape of the resulting growth. Some studies have been done to prove their necessity, but the exact mechanism of the silver and bromide binding is not known.[127] A recent report by Murphy and coworkers suggests that silver nitrate's primary role is as a catalyst to preferentially promote the reduction of gold ions onto the end of the growing nanorods. This study again highlights the need for freshly prepared ascorbic acid without photodegradation.[128]

In solution, there are two basic methods of growth: seed-mediated and one-pot. In seed-mediated synthesis, ascorbic acid is used as a weak reducing agent. Ascorbic acid is not capable of reducing the gold precursor (chloroauric acid, $HAuCl_4$) all the way to Au(0), instead creating Au(I) ions in solution, unless the pH is above 9.0.[126] The presence of a seed particle catalyzes the complete reduction to metallic gold at the

surface of each seed. In this case, lowering the concentration of seed increases the aspect ratio of the resulting rods. The aspect ratio can also be controlled to some extent by altering the concentrations of $HAuCl_4$ and silver nitrate. Increased concentrations led to increased longitudinal plasmon peaks (up to 1300 nm), up to a certain point, after which the opposite trend was observed.[111,127] These in-solution methods all report a significant batch-to-batch variability that depends on proper seed synthesis, water supply quality, pH,[129] and ascorbic acid concentration.[126] Seeds synthesized with too much sodium borohydride are too large, and larger seeds lead to more spherical products. If the ascorbic acid concentration is too high compared to the gold chloride concentration, shorter rods will be produced (excess capping).[127] Nanorod growth can also be stopped at a desired length by the addition of sodium sulfide.[130]

A one-pot method, “seedless” method can also be used as a more simplified way to create gold nanorods. Sodium borohydride is added directly to the growth solution; this method is simpler but affords less control over the resulting structures.[126] Researchers have even grown nanorods in a continuous flow microfluidic device.[131]

There is interest in solution phase synthesis of gold nanorods as researchers attempt to develop protocols that produce higher yields and more purity. Currently samples are contaminated with spherical particles and large platelets that are difficult to purify away from the final solution in a large scale. Because of the extreme sensitivity of the process (e.g. to miniscule, unintentional changes in reductant concentration), these syntheses are highly empirical and difficult to fully understand.[127,132] For example, one group found that they lost 50% of their aspect ratio by shifting the ratio of ascorbic acid

to chloroauric acid from 1.03:1 to 1.18:1.[133] Additionally, other groups found that buying CTAB from two different companies changed their synthesis product entirely.[134]

Many times it is necessary to assemble gold nanorods after wet-chemical synthesis and purification. This can be done by electrostatic or covalent binding to surfaces, self-organization by controlled drying, and polymer composite-driven assembly.[127,132]

Although chemical gold nanorod synthesis is the most common, researchers have used electrochemical, photochemical, ultrasonic, and radiolytic synthesis methods with some success. Additionally, templated synthesis is a promising method to make gold nanorods, especially supported rods and arrays of rods in two and three dimensions, without the extra assembly steps mentioned above. The earliest templating methods involved using polycarbonate or alumina nanoporous membranes to confine gold growth. Through ion-track etching or anodization, uniform pores of 5 - 50 nm are created on the templates. Chemical reduction or electrochemical deposition fills the pores with gold rods or nanowires. However, there is often up to 30% variance in the final length of the rods or wires due to uneven deposition, and the inside surface of the template pores are typically rough. Both of these factors lead to broadening of the longitudinal surface plasmon resonance peak, which is not desirable for most applications. Additionally, growth is limited to the two-dimensional area of the template, which limits scalability.[127] For more scalability, Gao et. al. synthesized hollow silica nanotubes functionalized with interior amino groups. Metallic gold and anionic gold are both electrostatically attracted to amino groups, so gold nanorods can be specifically synthesized inside the silica tubes using a seed-mediated growth protocol.[135]

As with the construction of gold nanospheres arrays, biological templating is attractive for the synthesis and immobilization of gold nanorods and other structures in three dimensions.[18,136] The sheer diversity and functionality, as well as evolvability, of DNA and protein structures give an advantage over traditional synthesis methods. The Belcher lab has immobilized gold nanoparticle arrays on bacteriophages and used them as nucleation points for the creation of nanowires and other complex geometries.[84] Chen et. al. synthesized gold nanoparticles at specific locations on a peptide double helix.[137] Recently, researchers have assembled gold nanorods onto DNA tripods whose angles can be precisely altered, controlling the resulting plasmon shift of the nanorods.[14]

Using proteins specifically, groups have grown gold nanorods within lysozyme crystals[138,139] (though researchers later found clustered nanoparticles present rather than nanorods) and assembled magnetic superstructures in protein cages.[15,23] Researchers have even shown that gold's catalytic activity can be retained when the nanoparticles are grown within lysozyme crystal pores.[140] Additionally, silver nanowires have been synthesized within peptide nanotubes, which can be enzymatically degraded to release the discrete tubes.[141] Another group synthesized and assembled magnetite crystals within peptide nanofibers.[142]

Of theoretical interest is a molecular-level understanding of seed-mediated gold nanoparticle growth. Despite years of experimental and theoretical work, there are still gaps in our knowledge of this nucleation and growth phenomenon.[143,144] Wei, *et. al.* recently used lysozyme crystals as templates to control the growth of small gold clusters and elucidate the resulting x-ray diffraction pattern and 3D structural characterization.[145]

However, a second group attempted to repeat this result and was able to more accurately model sulfur atoms into the crystal structure, rather than Au(I) ions.[146] More recently, Ueno and coworkers were able to observe sub-nucleation and growth of gold nanoparticles within a ferritin protein crystal.[94]

The use of protein crystals as templates for the immobilization and controlled growth of gold nanostructures may be able to provide further crystallographic insights into growth mechanisms, and the highly dense arrays of metal structures created using these methods are promising. As researchers gain the ability to control protein assembly topology, infinite template morphologies can be imagined. Protein crystal can be highly solvent accessible and contain hundreds of millions of identical pores, allowing for extremely parallel growth of arbitrarily shaped nanostructures.

*Impacts of presented work*

Our particular method creates an organized array of nanorods within a protein crystal. A seeded or non-seeded method can be used, as can multiple different gold precursors and reducing agents. Inside the scaffold, the rods are protected from thermodynamic relaxation, but can also be released for downstream applications. These pentatwinned nanorods don't have the presence of silver, and can be synthesized at higher aspect ratios and better crystallographic order than single-crystalline rods. Additionally, the lack of CTAB used in this protocol removes a source of variability and a roadblock in that CTAB ligand layers must be removed for most applications.

Templated synthesis is a promising approach to retain more control over gold nanoparticle growth in three dimensions, as well as to scale the synthesis process

economically. There is growing excitement for the possibility of assembling designer nanomaterials from the bottom up. Plasmonic and electronic materials could be designed from scratch in what are essentially molecular growth reactors. From the crystal structures available in the Protein Data Bank,[96] its clear that there are nearly infinite possible morphologies for gold nanostructures using this method. Additionally, as researchers continue to gain the ability to control protein assembly topology,[16,91] any template could be created. They may find applications in everything from energy storage and plasmonics to detection and drug delivery, as well as providing insight into the control and structural details for nanoparticle growth processes.

## RESULTS

### *Gold growth with chloroauric acid*

The same protein crystal, CJ, was used in most growth experiments. The overall goal of this project was to show that gold nanorods could be grown within the crystal pores, and that growth was dictated by the presence of a nucleation site or "seed" within the scaffold. Protein crystals were prepared in a manner similar to that in Chapter I (see Appendix). Extensive trial and error experiments were completed, varying concentrations, buffers, pH, and reaction times, to gain some control over the growth of nanorods and other nanostructures in the crystal. Typical reactions consisted of a protein crystal, seed in the form of $Au_{25}$ or another gold nanoparticle, a soluble gold precursor, and a reducing agent. However, growth could occur under some circumstances in the absence of a seed and reducing agent.

The first experiments were performed at neutral pH in a sodium phosphate buffer. The protocol is as follows: Crystals are loaded with $Au_{25}(GSH)_{17}NTA$ as detailed in the previous chapter. This is the 'seeding' step. The crystal is then looped to a solution of 1 mM $NiSO_4$ for 10 minutes to trap the gold nanoparticles within the scaffold. Next, the crystal is looped to a solution of 50 mM sodium phosphate for 10 minutes to allow unbound gold nanoparticles to diffuse from the scaffold. This increases the chance of using only nucleation sites at defined points within the scaffold; future experiments (like X-ray diffraction) will require this specificity, as will applications that use 3D arrays of nanostructures. After 10 minutes, the crystal is looped to a solution of 10 mM $HAuCl_4$ for 10 minutes to allow the soluble gold precursor to diffuse into the crystal pores. Lastly, the crystal is looped to a drop of 10 mM ascorbic acid, at which point the $Au^{+3}$ ions can be reduced and grow onto the gold seeds already present in the crystal (Fig. 3.1).

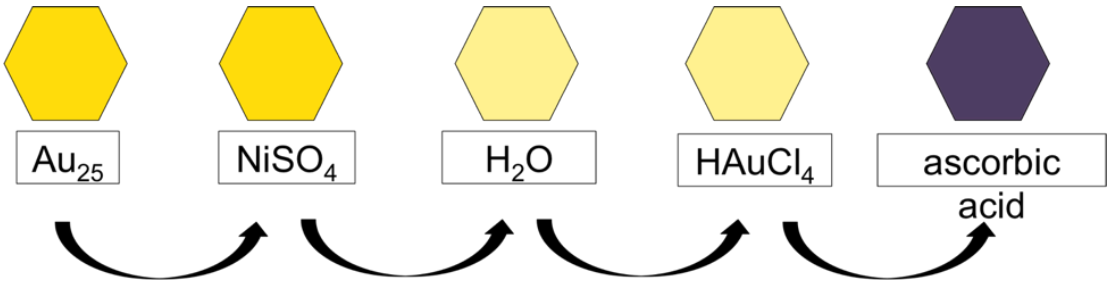


Figure 3.1 Schematic of typical gold growth protocol

$Au_{25}$ is first loaded and immobilized within the CJ crystal pores as described in the previous chapter. The crystal is then washed with water to remove any unbound gold and nickel. Next, gold salts are loaded into the crystal pores, followed by immersion in a reducing agent.

Two negative controls were performed with each experiment. One control did not have a seed or nucleation point present. Another control did not have any soluble gold precursor added to the crystal. No experiment that did not include $HAuCl_4$ or an equivalent gold salt showed any color change or indication of growth of the gold seeds overnight (Fig. 3.2). The yellow color of the crystal is indicative of the present of $Au_{25}$. The color of various gold nanoparticle solutions is dependent on the diameter of the particles (where increasingly larger nanoparticles appear pink, purple, then blue),[147] but even more importantly in our case, color is dependent on regularity or irregularity of shape, as well as proximity to neighbors in an aggregate[148]; we could quickly estimate the growth of larger particles (or that irregularly shaped structures were present) by the color change within the crystal; this was used to avoid performing electron microscopy or UV-Vis-NIR spectrometry on every one of the hundreds of samples we prepared. Only samples that looked "promising" (based on their color change) were further investigated.

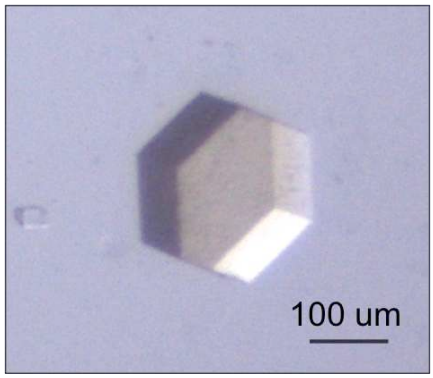


Figure 3.2 Gold growth negative control

A CJ crystal loaded with $Au_{25}(GSH)_{17}NTA$ for 30 mins, incubated with 10 mM $NiSO_4$ for 5 mins, and incubated in a drop of 10 mM ascorbic acid for 16 hrs. No observable color change occurs under white light without the presence of soluble gold precursor. Image taken with a brightfield optical transmission microscope.

It was easy to accomplish the first goal of this project; we immediately saw a color change in the crystal indicative of growth of the seed particles within the pores. However, controlling the growth based on presence or absence of seed ($Au_{25}$) proved to be very difficult. In multiple experiments, growth occurred with no obvious kinetic difference between the seeded and unseeded crystal. This was determined first by eye (Fig. 3.3).

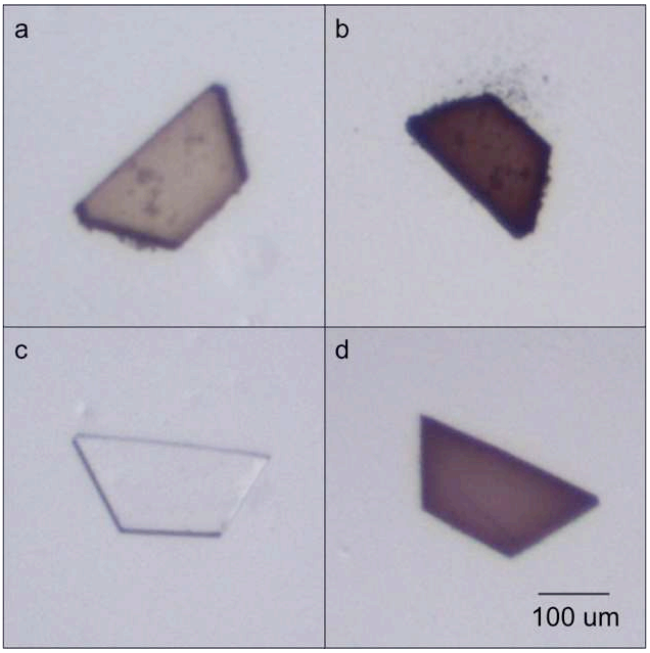


Figure 3.3 Seeded and unseeded gold growth

(a) A CJ crystal after a 30 min incubation in 1 mg/mL $Au_{25}GSH_{17}NTA$. (c) An empty CJ crystal. Both crystals from (a) and (c) were loaded with 1 mM $NiSO_4$ and 1 mM $HAuCl_4$ and placed in 1 mM ascorbic acid for 16 hrs prior to imaging (b & d). Image taken with a brightfield optical transmission microscope.

Many variables could account for this uncontrolled growth including Ni(II), pH, $HAuCl_4$ concentration, $HAuCl_4$ incubation time, ascorbic acid concentration, transfer versus direct addition of ascorbic acid, and crystal growth/crosslink/quench conditions. All of these variables were systematically observed for their affect on the resulting gold

growth within the crystal. Care was taken when making fresh solutions for each experiment and to use the same stocks whenever possible in an attempt to remove any extraneous variables. We have seen in many experiments that small changes in protocol can have inexplicable effects on the result.

We attempted seeded and unseeded growth controls in the presence and absence of Ni(II). We found that uncontrolled growth *could* occur in the absence of Ni(II), but that it *would* occur in the presence of Ni(II). For example, higher soluble gold concentrations would always cause uncontrolled growth, as would the presence of Ni(II) at any gold concentration. Although Ni(II) was a factor increasing the spontaneous nucleation of the soluble gold precursor, it was not the sole reason for uncontrolled growth. We hypothesize that in the reducing environment of the crystal, it's possible for the Ni(II) ion to act as a nucleation point for growth.

There was a fairly discernable trend related to pH of the reaction (Fig. 3.4). Typically reactions in $HAuCl_4$ at pH 5 gave the most growth, followed by pH 7, and lastly pH 9. For example, an empty crystal placed in a drop of 10 mM $HAuCl_4$ at pH 7.0 will begin to grow after less than 30 mins, whereas the same crystal placed in a drop of 10 mM $HAuCl_4$ at pH 9.0 will take up to 2 hrs to begin growth. Additionally, crystals reduced by ascorbic acid at pH 4.0 show more overall growth than those reduced by ascorbic acid at pH 7.0. This was an unexpected result, as ascorbate (above the pKa of 4.1) is known to be a better reductant for $HAuCl_4$. Additionally, some experiments show that above pH 9.0, ascorbic acid can reduce Au(III) all the way to Au(0), creating spontaneous nucleation points.[127] We hypothesize that Au(III) is simply more stable in a pH 9.0 borate buffer than at lower pH and was less likely to self-aggregate.

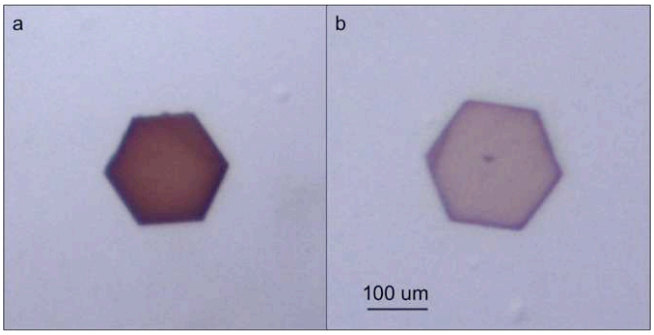


Figure 3.4 Effect of pH on gold growth

Crystal growth protocols undertaken at pH 7.0 (a) produced more observable color change than those at pH 9.0 (b). Both crystals were seeded with 1 mg/mL $Au_{25}$ for 30 mins, moved to a drop of 10 mM $NiSO_4$ for 5 mins, and then transferred to a drop of 10 mM $HAuCl_4$ at either pH 7.0 (a) or pH 9.0 (b). Images were taken after 2 hrs in $HAuCl_4$.

As expected, the soluble gold precursor had a strong affect on overall growth. At concentrations of 0.1 and 1 mM, immediate growth did not occur, and growth could be controlled by variables incubation time and reductant. For example, crystals with lower concentrations of $HAuCl_4$ could simply be incubated for a long period of time to encourage growth. Moreover, if crystals at 0.1 and 1 mM $HAuCl_4$ were transferred to a drop of ascorbic acid after a 10 min incubation, growth typically did not occur. At concentrations of 10 mM and higher, growth began to occur immediately and was less dependent on any other variables in this list. For example, growth can occur spontaneously at 10 mM without the presence of a seed, Ni(II), a reducing agent, or an overnight incubation in the $HAuCl_4$. The total amount of growth (as determined by incubations over 72 hrs), was then determined by the pH of the solution, as explained above.

Additionally, longer incubation times in $HAuCl_4$ encouraged more overall growth in crystals. This effect was strongly linked to the concentration of the $HAuCl_4$. Typically

no further color change was seen after incubation for 16 hrs. However, at the lowest concentrations, growth slowly occurred and plateaued at ~72 hrs.

Interestingly, the concentration of ascorbic acid didn't have as strong effect as other variables in this list. Ascorbic acid concentrations between 1 and 10 mM only further reduced gold when $HAuCl_4$ concentrations used were less than 10 mM. The ascorbic acid concentration was usually matched in molar ratio and pH to that of $HAuCl_4$.

The standard protocol was to transfer the crystal to a new drop of ascorbic acid after incubation in a specified amount of time in $HAuCl_4$. Other options included leaving the crystal in $HAuCl_4$ (not using a reductant), adding reductant directly to the well with $HAuCl_4$, and moving the crystal to a drop of water or other buffer instead of reducing agent. It was first discovered that crystals with 10 mM of more of $HAuCl_4$ did not require reductant and would grow spontaneously (without a seed) when left in $HAuCl_4$ or moved to a drop of water. Adding ascorbic acid directly to the well with $HAuCl_4$ always caused spontaneous growth, both within the crystal and throughout the well (Fig. 3.5).

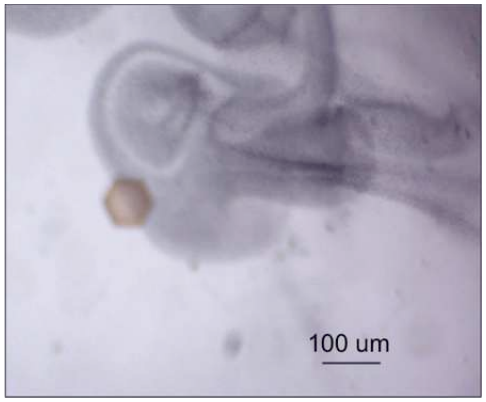


Figure 3.5 Spontaneous gold nucleation events

Spontaneous nucleation occurs immediately wells with 10 mM ascorbic acid and 10 mM $HAuCl_4$.

At first we were surprised by this result, because most previous research explains that below pH 9.0, ascorbic acid should not be able to reduce $HAuCl_4$ to elemental gold.[132] However, because of the high reduction potential of $AuCl_4^-$ (+0.93 V), self-nucleation is plausible at higher concentrations.[135] Since we had already spent a significant amount of time investigating the effects of various reaction conditions, we did not continue this exhaustive search once we realized that spontaneous nucleation of $HAuCl_4$ was incredibly difficult to control. We could certainly have tested even lower concentrations, new buffers, and more stringent stepwise growth protocols. I should note that the brief stepwise growth experiments we did include (where crystals were transferred to new, low concentration growth conditions at set intervals of time) did not lead to any less self-nucleation events.

Instead we focused on one of three causes for self-nucleation of $HAuCl_4$: ascorbic acid, the crystal crosslinking conditions, or the amino acids within the crystal pores. Since we already determined that growth is possible without the addition of ascorbic acid, we know that cannot be the only culprit of uncontrolled nanorod growth. Our methods for stabilizing the crystal via chemical crosslinking could, however, be affecting the growth mechanism. Conditions in which the crystals were grown, crosslinked, and quenched can change the overall charge inside the pores. This charge may affect the crystal's ability to adsorb molecules (including the gold seed and the soluble gold precursor). Additionally, several reducing agents, including dimethylamine borane complex (DMAB) and hydroxylamine, are used during our original crosslink and quench methods. Although the crystals are washed before use in any growth

experiments, it was still important to determine if this was a factor in uncontrolled growth.

The typical scheme (glyoxal crosslinking in the presence of DMAB, followed by hydroxylamine quench) is outlined in Chapter II. Here we introduce a crosslink using 1-Ethyl-3-(3-dimethylaminopropyl)carbodiimide (EDC) and a quench in 50 mM borate at pH 10.0. EDC is a scarless crosslinker; if after the 2 hr crosslink, EDC hasn't crosslinked a carboxyl group to a primary amine, the EDC compound will be removed by the pH 10.0 solution. After the crosslink and quench, the original chemical structure of the crystal should be retained. With a typical glyoxal crosslinking, unreacted aldehyde groups are converted to oximes or secondary amines, instead of being removed. Unused DMAB and hydroxylamine within the crystal may also not be completely removed by a wash step. They could be giving the crystal more overall reducing power. Figure 3.6 shows the difference between glyoxal and EDC crosslinked crystals after 16 hour incubation in 10mM $HAuCl_4$ at pH 7.0. After showing the negative effects on attempting to control growth with a glyoxal crosslinked crystal, all future experiments were performed with EDC crosslinking.

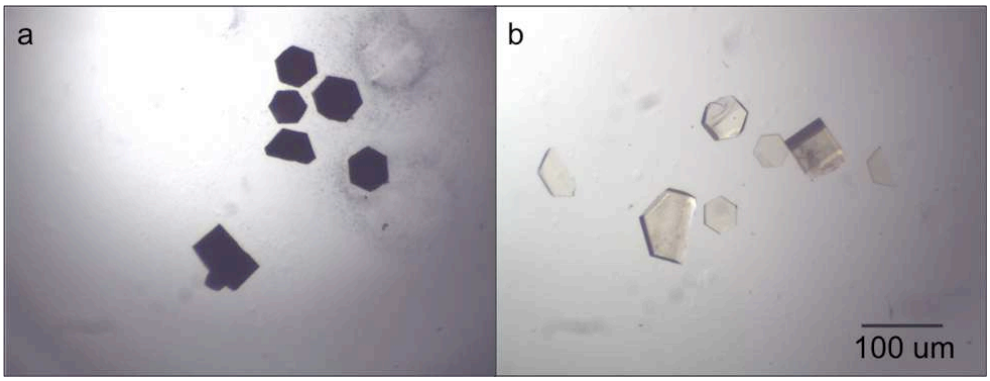


Figure 3.6 Effect of crosslinking on gold growth

(a) Glyoxal-crosslinked and (b) EDC-crosslinked crystals after 16 hrs in 10 mM $HAuCl_4$ at pH 7.0.

These experiments were very sensitive to small changes in reaction conditions which could lead to large changes in results. Details like dirty loops and wells can cause runaway growth and can be difficult to diagnose. Additionally, we have some anecdotal evidence that reactions involving $HAuCl_4$ are susceptible to changes in the humidity and ozone content during different seasons (chloroauric acid is hygroscopic). Other groups have run into these same technicalities when working with gold growth mechanisms.[126]

EDC crosslinked crystals showed better overall control of seeded vs. unseeded gold growth. Typically we saw some, but not repeatable, kinetic control over growth depending on the presence of $Au_{25}$ in the crystal (Fig. 3.7).

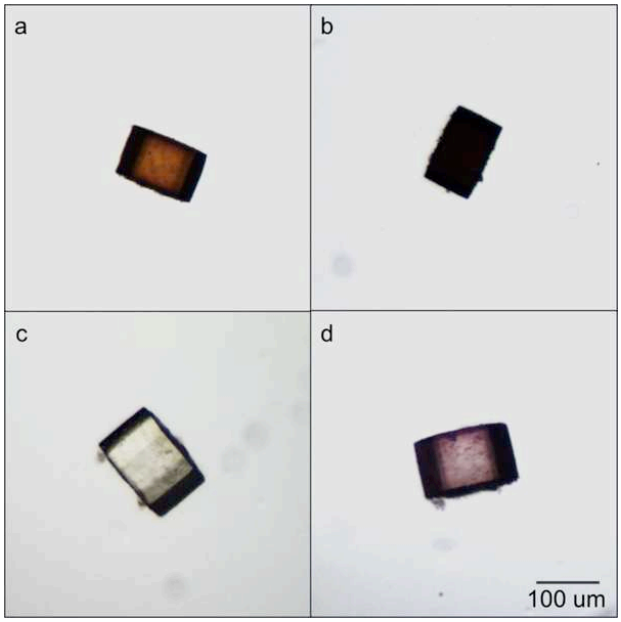


Figure 3.7 Seeded and unseeded gold growth

(a) Seeded versus (c) unseeded growth in EDC crosslinked crystal with 10 mM $HAuCl_4$ at pH 7.0 followed by (b & d) 10 mM ascorbic acid at pH 7.0 for 1 hr.

Despite limited success from changing the crosslinking protocol, it became clear that some amino acids lining the pores of the crystal had been acting as reducing

agents for the $Au^{+3}$ ions, which has precedent in the literature.[149–151] In several cases, bovine serum albumin (BSA) has been used to induce gold nanoparticle formation,[149,150] and specifically tyrosine residues contribute to gold salt reduction.[151]

Additionally this was confirmed by performing various experiments in solution. Without the crystal present, there is a kinetic difference between growth in the presence and absence of a gold seed. For example, a well of 10 mM $HAuCl_4$ could be left sitting overnight and not self-nucleate, but would nucleate if a crystal was present in the well (Fig. 3.8a). This is anecdotally evident by the fact that nucleation and growth was always occurring in and around the crystals in the well, not sporadically within the wells (Fig. 3.8b). However, as mentioned above, if any contaminate was introduced to the solution, $HAuCl_4$ was extremely sensitive to runaway nucleation.

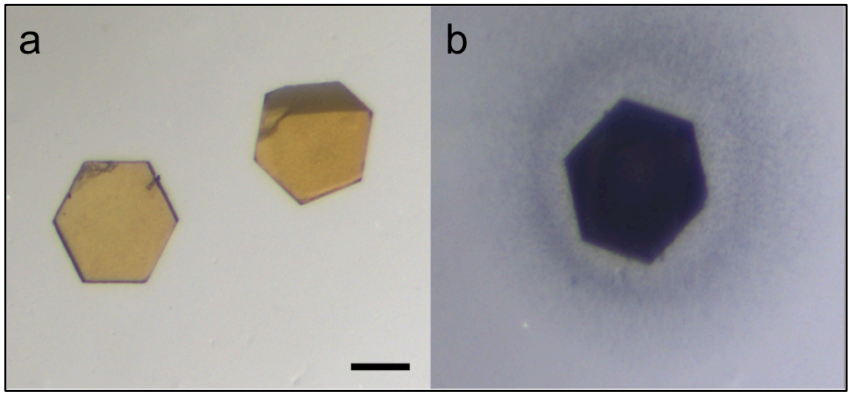


Figure 3.8 Au growth states

(a) Two unseeded CJ protein crystals after loading in 10 mM $HAuCl_4$ for 10 mins. (b) An unseeded CJ protein crystal, loaded with 10 mM $HAuCl_4$ for 10 mins, then transferred to 10 mM ascorbic acid for 1 hr. Scale bar is 100 μm.

With the new crosslinking protocol, we again investigated the effects of loading time of gold seeds ($Au_{25}$) and $Au^{+3}$ ions on the amount of growth within the crystal. In summary, with no seed present, crystals may sometimes turn completely black by eye,

but typically look more grey with particles crashed out in the surrounding well. When gold seeds were loaded into the crystal for only 5 mins before growth, the crystal took longer (up to overnight) to turn completely black. Whereas crystals that were loaded with $Au_{25}$ for 1 hr prior to growth typically turned fully black within 20 mins of placement in 10 mM ascorbic acid. Additionally, the length of chloroauric loading had an effect on overall growth. When the length of loading time was increased to 16 hrs, crystals did not turn completely black in any case during reduction (independent of seed loading time). Additionally more aggregation and nucleation within the drop was seen.

We also investigated the effect of $NiSO_4$ (used for locking the nitrilotriacetic acid ligand on the $Au_{25}$ particle to the Histidine tag on the crystal) on spontaneous nucleation. As we had noticed that with this method, $Au_{25}$ was not needed to produce nucleation. Without $NiSO_4$ present, spontaneous nucleation could be slowed, but not fully prevented, so $NiSO_4$ was used in future experiments to preserve the specific attachment of the gold seed within the crystal pore.

Additionally, we explored the effect of pH on overall gold growth. Most experiments were carried out at pH 7.0. When the pH was changed to 9.0, much less overall growth occurred. We hypothesized that this is because some gold structures are more stable at higher pH. At pH 5.0, much more aggregation occurred within the well, but did not aid in overall growth within the crystal.

We determined that multiple rounds of growth can be performed to encourage further darkening of the crystal and presumably more growth within the pores. Once a crystal had been through one round of growth ($Au_{25}$, $HAuCl_4$, ascorbic acid), it was placed back into a fresh drop of $HAuCl_4$, then again into ascorbic acid. This “stepwise”

growth caused darker crystals by eye after multiple rounds (Fig. 3.9), but we found that the rods present were no longer than those that could be produced by one round of growth. We suspect that prolonged exposure to the growth solutions may cause some etching of the longest, most fragile rods (Fig. 3.10).

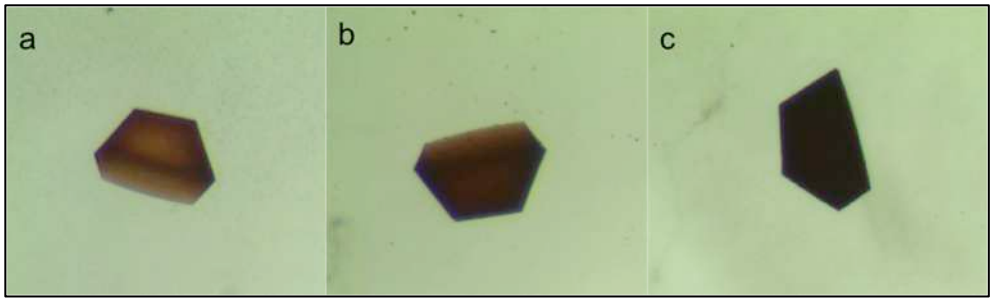


Figure 3.9 Effect of stepwise growth on overall gold growth

A CJ crystal after (a) one, (b) two, and (c) three rounds of growth with 10 mM $HAuCl_4$ and 10 mM ascorbic acid. Each round consisted of 10 mins in $HAuCl_4$ and 1 hr in ascorbic acid. Crystals are approximately 300 um in diameter at their longest point.

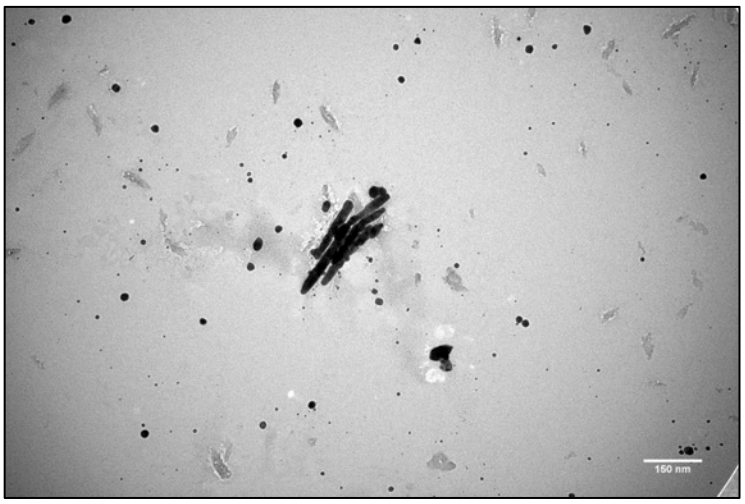


Figure 3.10 TEM of stepwise growth

Transmission electron microscopy of structures resulting when a CJ crystal is subjected to six “rounds” of growth and then dissolved. Scale bar is 150 nm. *Image: R. Nemeth*

To confirm some of these anecdotal growth observations made by optical microscope (regarding the effect of $Au_{25}$ and $HAuCl_4$ loading times), we dissolved many crystals and viewed the resulting structures under transmission electron microscopy (see below for dissolving protocols). Figure 3.11 shows the differences in gold products with and without the presence of $Au_{25}$ as a nucleation point and with and without ascorbic acid as a reducing agent. These results show that although gold nanoparticles (and sometimes rods) are formed in the absence of a gold seed, rods were more plentiful and longer when a seed is present.

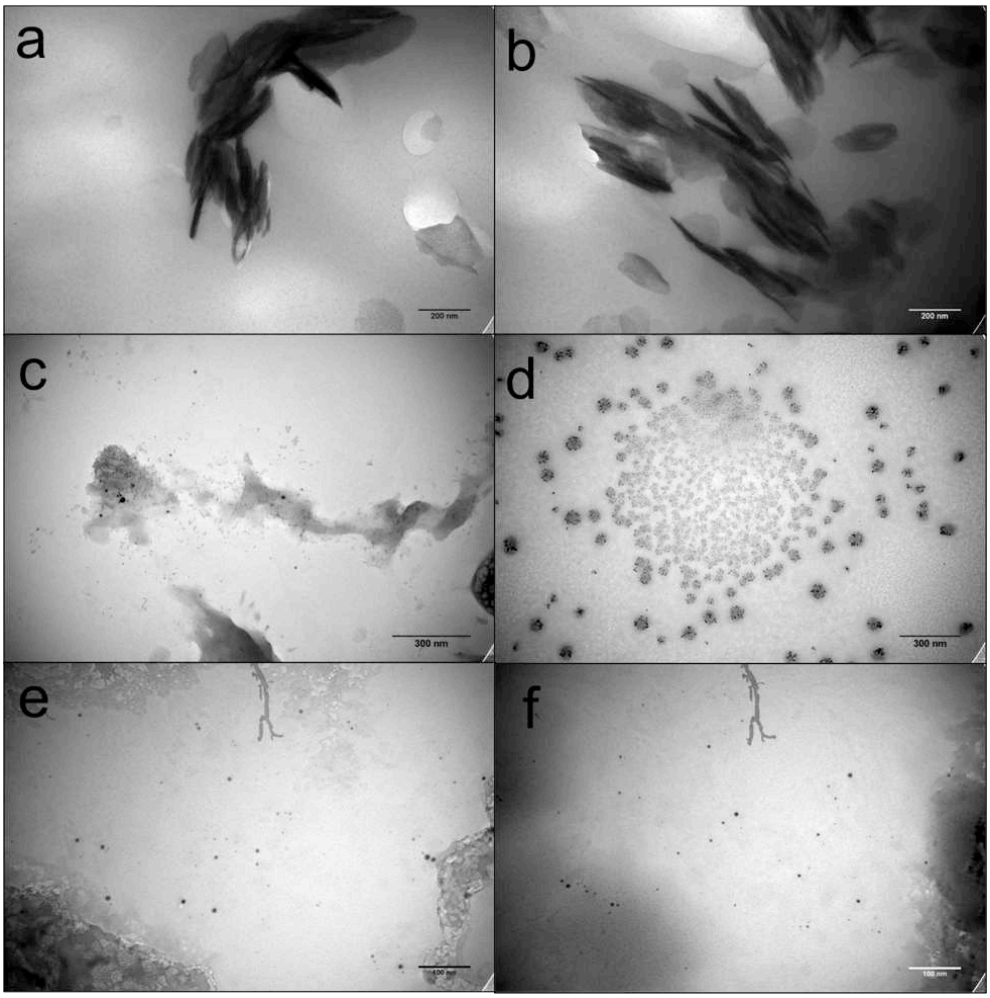


Figure 3.11 TEM of gold structures from seeded and unseeded growth

TEM of the resulting gold structures when a (a & b) seeded or (c & d) unseeded CJ crystals are grown in 10 mM $HAuCl_4$ for 10 mins, transferred to a drop of 10 mM ascorbic acid for 1 hr, and then dissolved. (e & f) TEM of seeded CJ crystal loaded with 10 mM $HAuCl_4$ for 10 mins and then dissolved shows that reduction is required for nanoparticle growth. Scale bars are (a & b) 200 nm, (c & d) 300 nm, and ( e & f) 100 nm. *Image: R. Nemeth*

Additionally, we confirmed our visual observation that leaving a CJ crystal soaking in $HAuCl_4$ overnight before reduction may prevent rod formation. We believe this is because more self-nucleation occurred, including outside the crystal, which

created only particles. Figure 3.12 shows typical TEM results from a normal versus extended $HAuCl_4$ loading time.

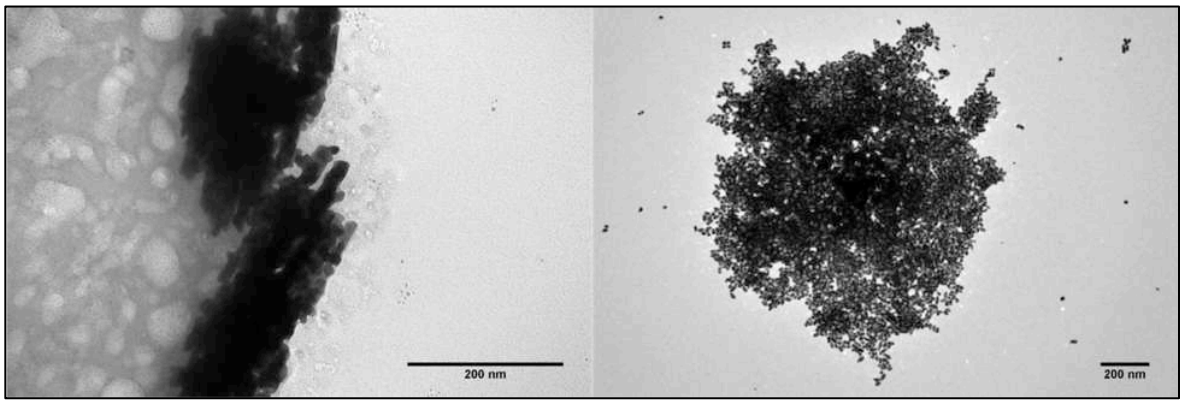


Figure 3.12 Effect of $HAuCl_4$ loading time on resulting gold structures

Left: A gold structures within a CJ crystal loaded with $Au_{25}(GSH)_{17}NTA$ for 30 mins, $HAuCl_4$ for 10 mins, reduced by ascorbic acid, then dissolved for imaging. Right: The results when the $HAuCl_4$ loading time is increased to 16 hrs. Scale bars are 200 nm. *Image: R. Nemeth*

The overall quantity of seeds present in the crystals before nucleation affected the products observed. We demonstrated this effect by varying the $Au_{25}$ loading time which can be seen in Figure 3.13. The sample with a longer $Au_{25}$ loading time appears to have only made smaller particles, while the sample with a shorter $Au_{25}$ loading time formed larger particles and rods with low aspect ratios. We believe the results of these experiments are caused by altering the amount of nucleation sites for growth. The longer loading time of the seed will result in more available seed sights once nucleation is initiated in the growth step, ultimately leading to more particles. When a short seed load time is used there may be less available nucleation sites leading to large particles and more rod formation.

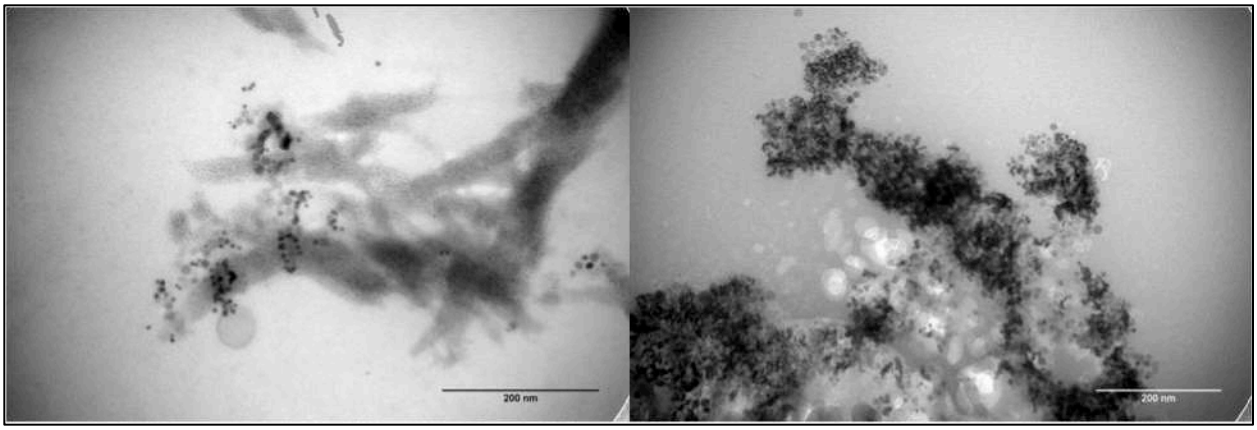


Figure 3.13 Effect of $Au_{25}$ loading time on resulting gold structures

Left: CJ crystals load with $Au_{25}$ seeds for 16 hrs before gold growth, scale bar is 200 nm. Right: CJ crystals load with $Au_{25}$ seeds for 30 mins before gold growth, scale bar is 200 nm. *Image: R. Nemeth*

Apart from looking at seed loading time effects we also carried out an experiment in which we varied the loading time of $HAuCl_4$ prior to reductant addition. 1, 3, and 4 min 10 mM $HAuCl_4$ soaking times were carried out and the resulting products after crystal dissolving were measured. No results were obtained for the 1 minute $Au^{3+}$ soak sample due to the lack of any products on the TEM grid. The 3 min $Au^{3+}$ soak sample showed the formation of particles with an average diameter of 8.8 nm with a standard deviation of 2.9 nm (n=75). Four minutes of $Au^{3+}$ soak time showed the development of rods with an average width of 25.0 nm with a standard deviation of 8.5 nm (n=33) and an average length of 79.8 nm with a standard deviation of 33.1 nm (n=34).

Although there was significant variation between trials, this method of growth produced the longest overall rods we saw (870 nm). There were numerous rods between 500 and 700 nm in length. Possible reasons for the variability in products include impurities in the well that may provide nucleation sites and variability in the

chloroauric acid samples. Figure 3.14 shows some examples of the types of structures we saw from this protocol. Panels a and b are high resolution transmission electron microscopy images of some of the longer rods grown in CJ crystals. Of note in panel b are the perpendicular segments that connect the four rods. CJ crystals have ~3 nm lateral pores that may account for this attachment. In panels c and d, there are many nanoparticles of varying sizes surrounding the rods. Panel e shows an only partially dissolved crystal still surrounding gold nanorods. Panel f shows some of the shorter rods produced by this growth method, and illustrates the bundles of rods that tend to form when the crystal is dissolved.

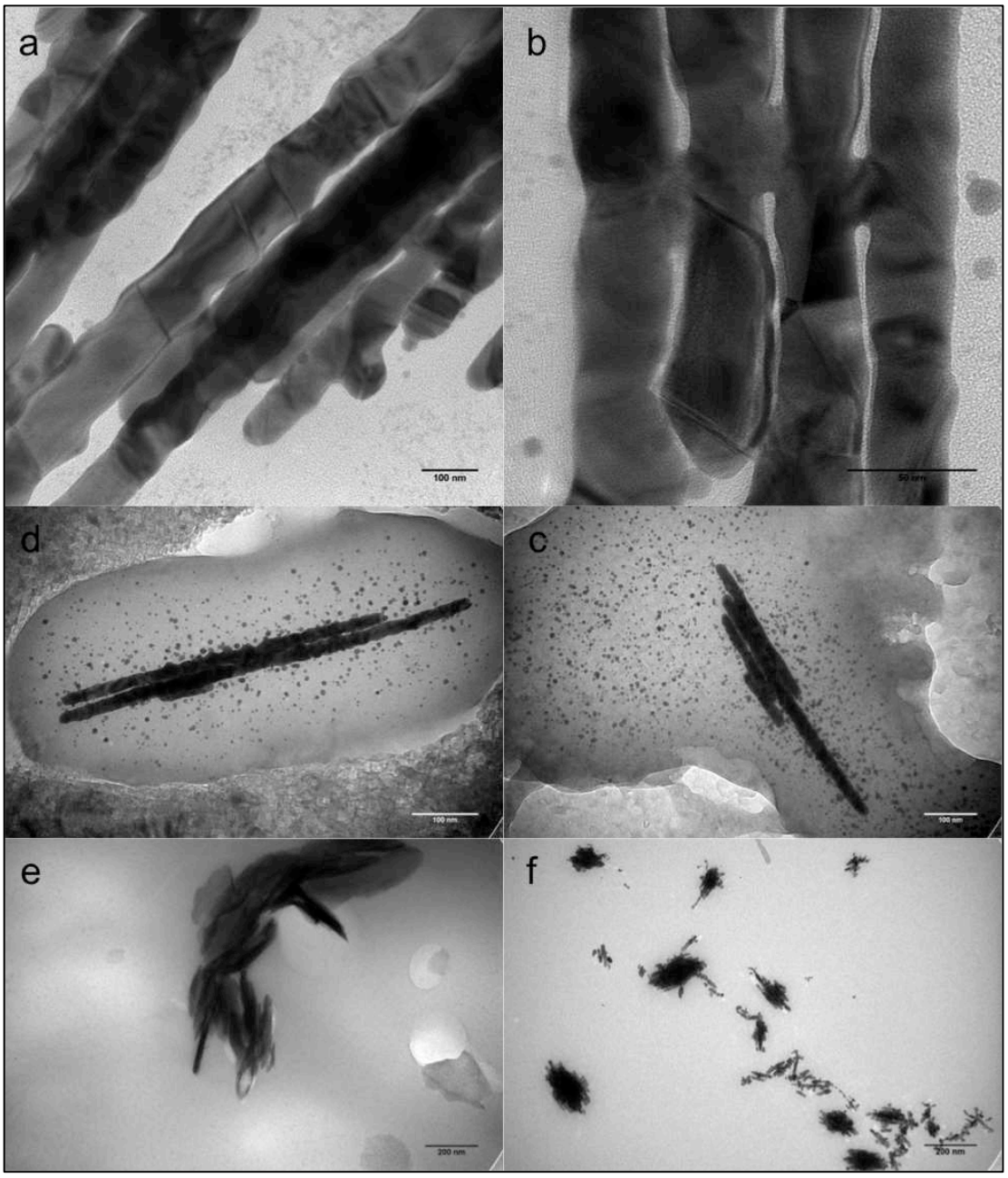


Figure 3.14 Gold nanorods resulting from gold growth within crystal pores

TEM of dissolved CJ crystals after seeded growth by $HAuCl_4$ and ascorbic acid. (a & b) High resolution TEM. Scale bar (a) 100 nm (b) 50 nm. Scale bar (c & d) 100 nm. Scale bar (e & f) 200 nm. *Image: R. Nemeth*

To demonstrate the versatility of this growth method, we grew gold structures within crosslinked CJ protein crystals using two other “seed” particles as nucleation

sites: $Au_{102}(pMBA)_{44}$ and 5 nm diameter gold nanoparticles (5 nm AuNP) with tannic acid surface ligands. In both cases, the seed particle was allow to adsorb into the crystal before transfer to 10 mM $HAuCl_4$, then 10 mM ascorbic acid. Color change was seen in 1 hr, suggesting the presence of larger gold structures within the crystals. The 5 nm AuNP seed also showed good control of growth between a seeded and unseeded crystal (Fig. 3.15 and 3.16).

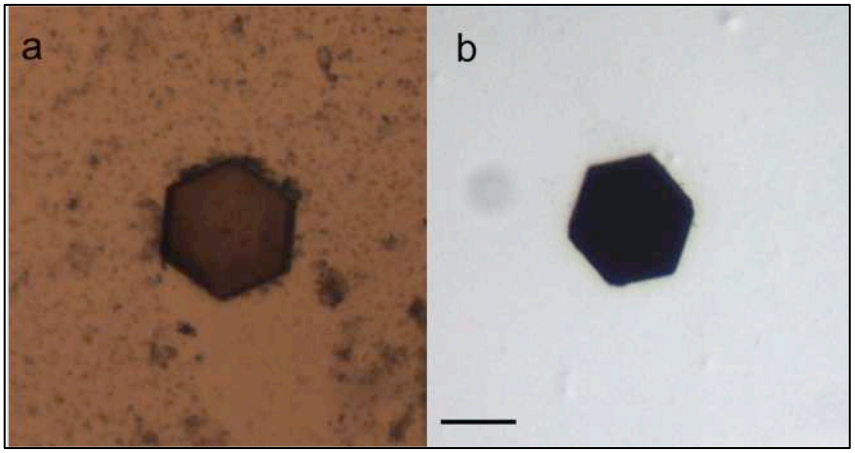


Figure 3.15 $Au_{102}$ as an alternate seed for gold growth

(a) CJ crystal in a solution containing $Au_{102}(pMBA)_{44}$ (b) The same CJ crystal after adsorption of 10 mM $HAuCl_4$ for 10 mins and 16 hrs in 10 mM ascorbic acid. Scale bar is 100 μm.

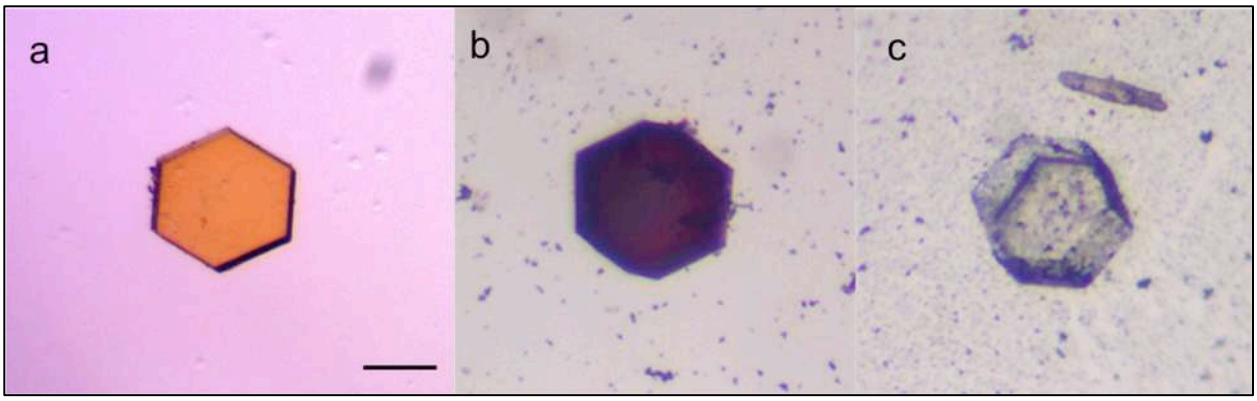


Figure 3.16 5nm gold nanoparticles as an alternate seed for gold growth

(a) CJ crystal after 3 days in 1 mg/mL 5nm AuNP. (b) The crystal from (a) after transfer to 10 mM $HAuCl_4$ for 10 mins then 10 mM ascorbic acid for 1 hr. (c) A similarly prepared CJ crystal that was not loaded with 5nm AuNP before transfer to $HAuCl_4$ and ascorbic acid. This crystal shows minimal preferential gold growth within the pores. Scale bar is 100 μm.

We also grew mixed metal nanostructures within the CJ crystal pores by using $Au_{25}$ as a nucleation site for silver growth, using a Silver Enhancer Kit (#SE100) from Sigma Aldrich. Figure 3.17 shows the results of one such experiment. Panels a-c show an $Au_{25}$ loaded CJ crystal in the silver growth solution over time, while panels d-f show a similar crystal in the growth solution over time, but without a pre-loaded $Au_{25}$ seed. Over 24 hrs, the seeded crystal undergoes a more significant color change than the unseeded crystal.

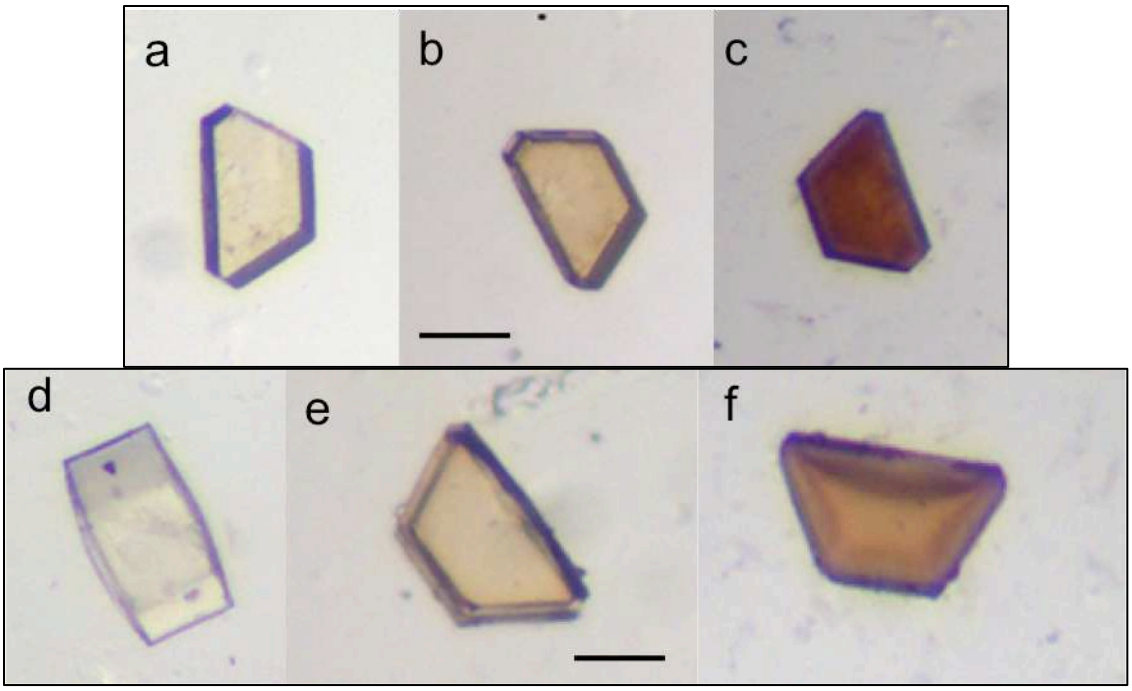


Figure 3.17 Ag growth from $Au_{25}$ seeds

A CJ crystal, $Au_{25}$ loaded (top row) or not (bottom row), in the silver growth solution at t = 0 (a & d), t = 15 min (b & e), and t = 24 hrs (c & f). Scale bars are 100 μm.

The longest gold nanorods grown using $HAuCl_4$ and ascorbic acid were 870 nm, but rods could also be as short as <100 nm (Fig. 3.18). A total of 2496 width measurements and 452 length measurements were taken over 452 rods under four different dissolving conditions. The average diameter of all rods grown within CJ protein crystals was 20.2 nm with a standard deviation of 4.7 nm, which is larger than the 13.1 nm diameter of the CJ crystal pore (Fig. 3.19).

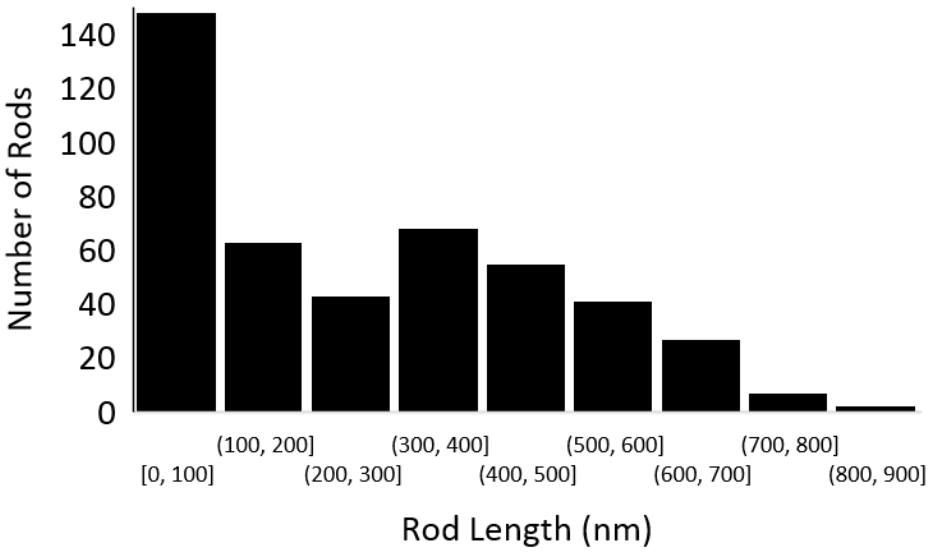


Figure 3.18 Rod length variation

Histogram of all rod lengths recovered from dissolved CJ protein crystals. Histogram includes all trials that used $Au_{25}$, $HAuCl_4$, and ascorbic acid for growth. Measurements taken with ImageJ.

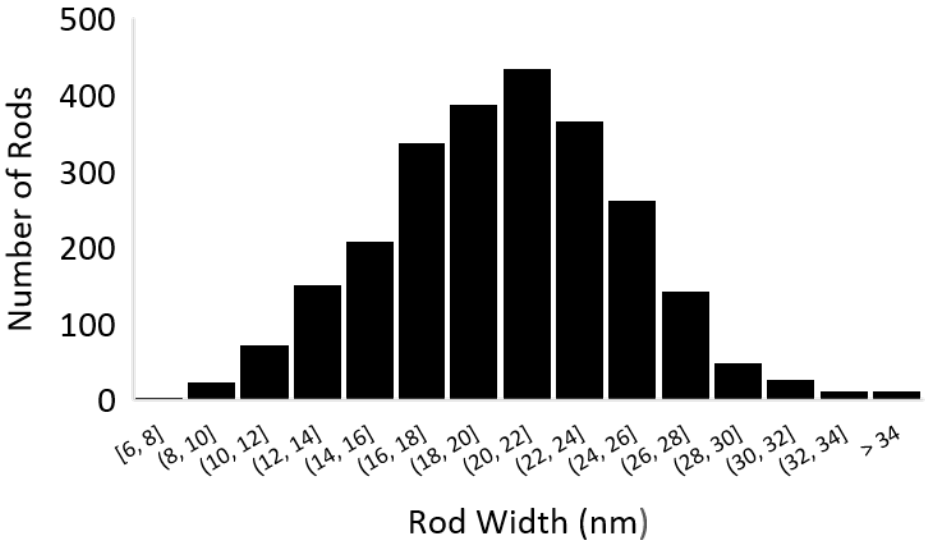


Figure 3.19 Rod width variation

Histogram of all rod widths recovered from dissolved CJ protein crystals. Histogram includes all trials that used $Au_{25}$, $HAuCl_4$, and ascorbic acid for growth. Measurements were taken at multiple points on all rods, as each individual rod also had width variations. Measurements taken with ImageJ.

Figure 3.20 shows the frequency of occurrence of rod length (a) and width (b) when 10 mM $HAuCl_4$ and 10 mM ascorbic acid are used to grow gold within an unseeded CJ crystal. Panels c and d of Figure 3.20 show the corresponding results for a seeded CJ crystal. The rod widths are comparable, but the seeded crystals have slightly higher occurrences of rods in general, specifically skewed towards longer rods. Panels e and f show the changes that occur when the crystals are sonicated to disperse the gold rod products. The widths of rods (Fig. 3.20 panel f) are narrower and shorter length rods (panel e) do not occur as frequently.

Rods resulting from other growth and dissolving methods are shown in Figure 3.21. The crystals in panels a & b were dissolved with 6 M guanidinium chloride (GdnHCl) and 0.1 M hydroxylamine. These two solutions are known to denature and cleave proteins, respectively. However, they also seem to etch the resulting gold nanorods, as the histograms show rods that are both shorter (panel a) and more narrow (panel b) than any in Figure 3.21, which were all dissolved by the standard high pH method (0.1 M NaOH and 0.1 M KCl at pH 13). A similar result is shown for dissolving in the presence of glutathione (GSH) in panels c and d. In panels e and f we show that growing the crystals over multiple rounds of exposure to $HAuCl_4$ and ascorbic acid does not produce longer rods.

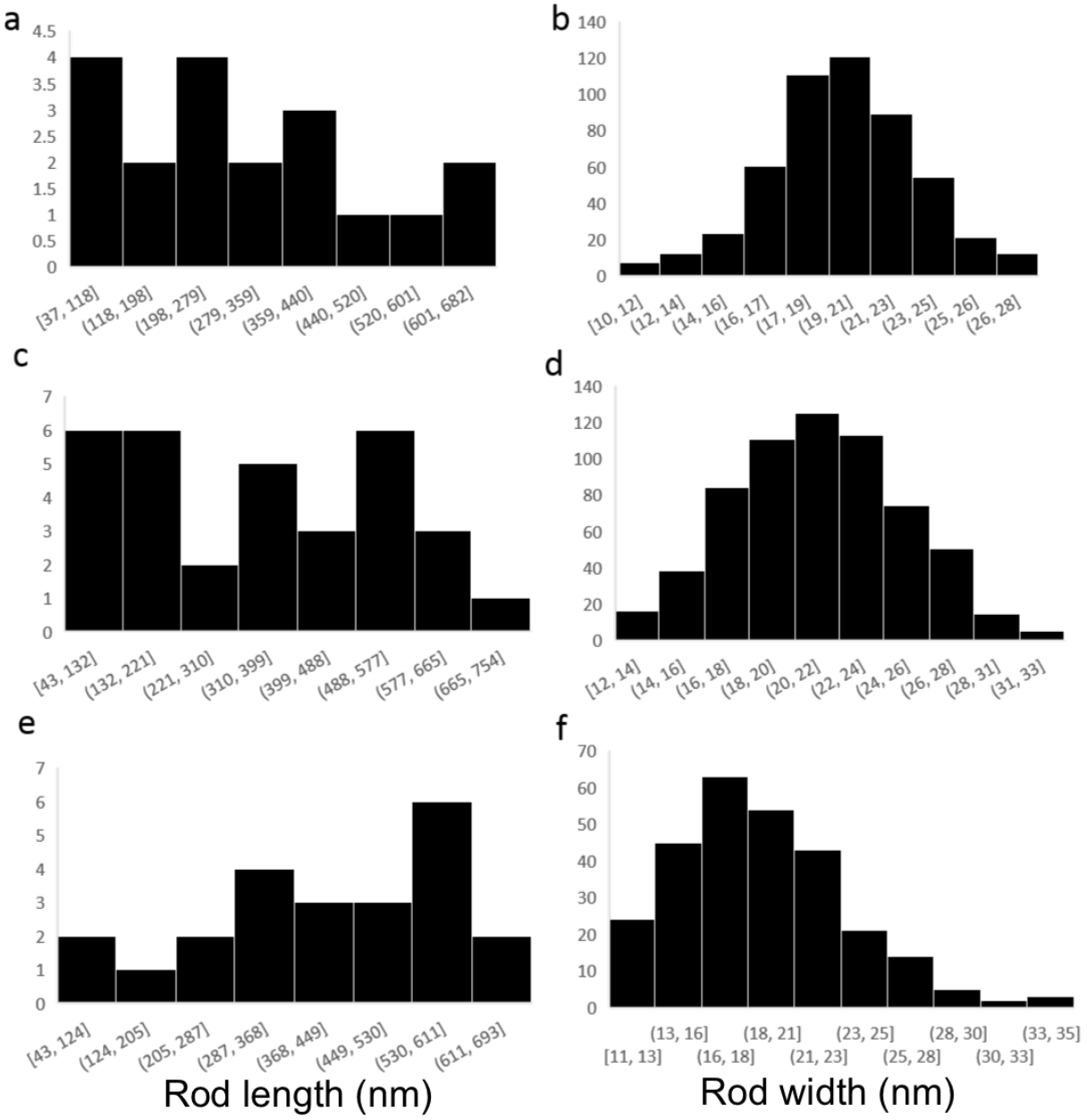


Figure 3.20 Histograms of rod lengths and widths from seeded and unseeded crystals

Frequencies of occurrence of rod length (a, c, e) and width (b, d, f) for unseeded, grown crystals (a & b), seeded, grown crystals (c & d), and seeded, grown, and sonicated crystals (e & f). All crystals were dissolved in 0.1 M NaOH and 0.1 M KCl at pH 13. Measurements made in ImageJ.

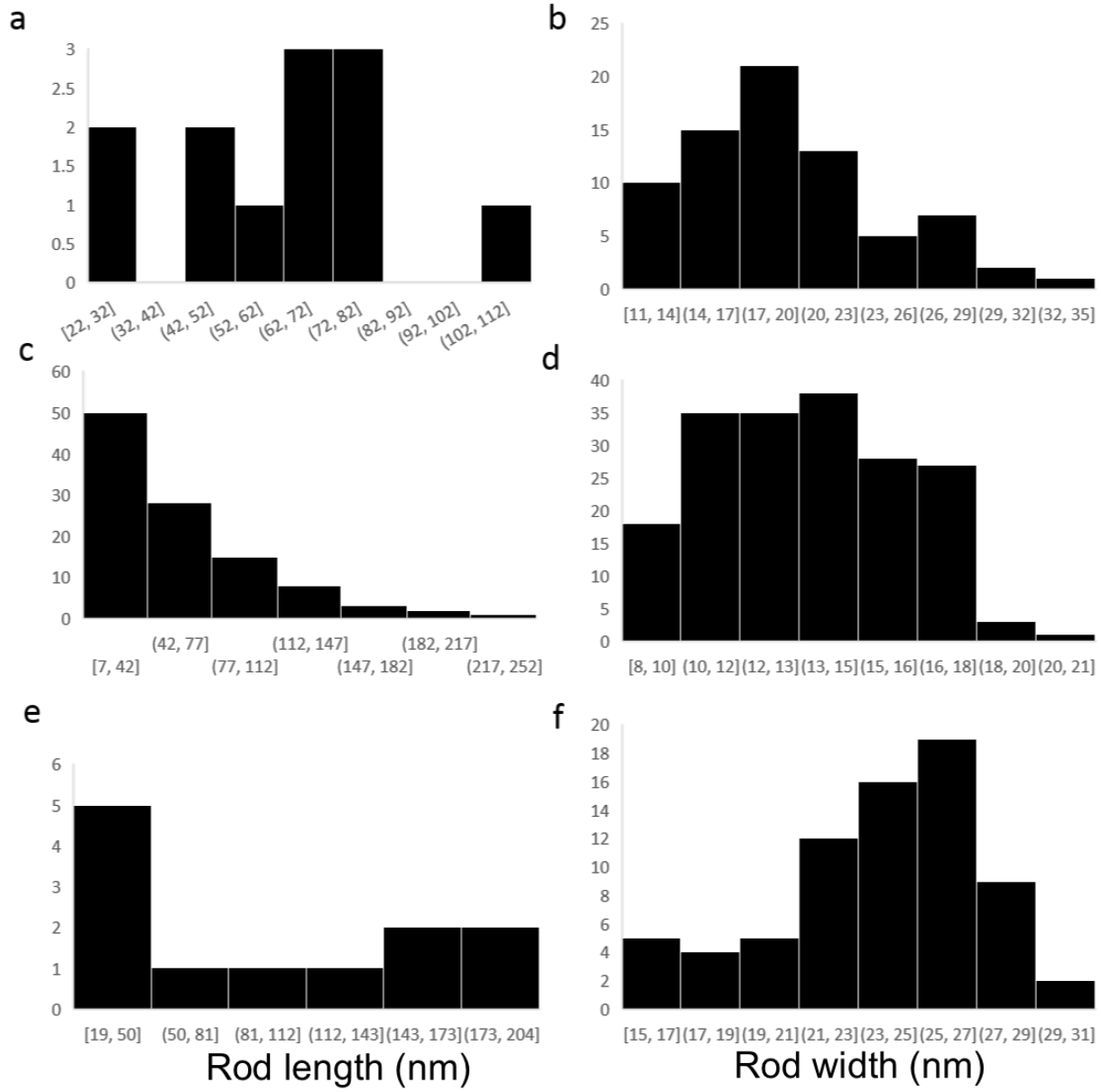


Figure 3.21 Histograms of rod lengths and widths from different dissolving protocols

Frequencies of occurrence of rod length (a, c, e) and width (b, d, f) for different crystal growth and dissolving methods: Guanidinium chloride and hydroxylamine at $37^0$C (a & b), glutathione at $37^0$C (c & d), and dissolving in 0.1 M NaOH after six growth cycles (e & f). All crystals were grown by the standard method of 10 mM $HAuCl_4$ and 10 mM ascorbic acid. Measurements made in ImageJ.

Figures 3.20 and 3.21 show that rods widths vary within each experiment. The average rod width over all growth methods and dissolving protocols was 20.2 nm with a standard deviation of 4.7 nm. Due to the variation in rod width within a single rod, multiple measurements were made per rod. In fact, the width variation for a single rod (Fig. 3.22) shows a very similar pattern to measurements made over multiple rods, meaning the width of each individual rod can vary by multiple nanometers from its widest to narrowest point.

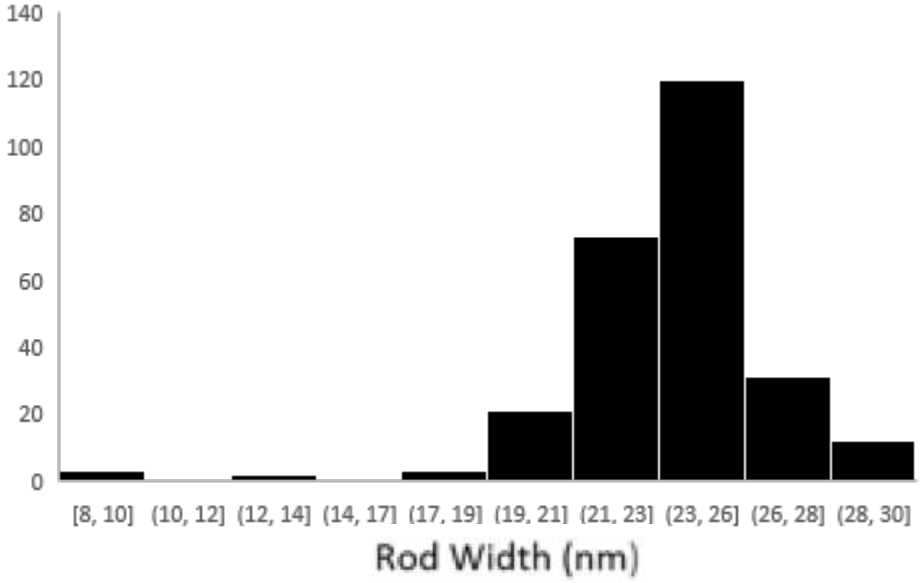


Figure 3.22 Single rod width variation histogram. Measurements made in ImageJ.

Frequency of occurrence of widths of a single rod extracted from a dissolved CJ crystal and measured in 250 places.

We noticed that during the growth process, the surface area of the crystal could expand by up to 20%, and we hypothesize than the protein can be pushed outward during rod growth.

The calculations below (Fig. 3.24) help explain how this phenomenon of pore and crystal swelling may take place. Before gold growth (top left) the 13 nm diameter pore is

within a translated unit cells of 18 nm side length. The total area is 281 $nm^2$, with the pore consisting of 133 $nm^2$ and the protein approximately 148 $nm^2$. With the new pore diameter of 20 nm, equal to that of the gold rods grown within, and assuming retention of the same unit cell angles, the new minimum total unit cell area is 462 $nm^2$ and the new protein area remains the same at 148 $nm^2$.

In fact, a 20 nm diameter circle is the largest circle that can be contained within a parallelogram whose non-circle area (grey areas) are limited to 148 $nm^2$. In other words, 20 nm is as large in diameter as the gold nanorods can become without breaking or expanding the unit cell in some way. For example (bottom right), a gold nanorod of hypothetical 21 nm diameter would require a total protein (grey) area of 158 $nm^2$ to be fully contained, which is larger than the protein area available per unit cell of the CJ crystal. Without significant denaturation, the overall volume of the protein within the crystal should not change.

We hypothesize here that the force of the fast and significant gold growth was able to move the protein ‘out of the way’ up until the point of actually breaking peptide bonds, denaturing the protein, or severing crosslinks between monomers. Looking more closely, the growth of the gold nanorods expands one corner of the unit cell (length a) by 1 nm while contracting the adjacent corner (length b) by 1 nm. The corners of these diagrams correspond to a tetramer (interface of four CJ monomers) within the crystal, which is also the location of some of the most flexible loops and helices in the crystal structure, most likely allowing for more than enough room to make these changes in area.

If every pore in the protein crystal were to expand from 13 nm to 20 nm in diameter during gold growth, we may expect at least a 60% expansion in the total crystal surface area, where instead we see up to 20% at most. We propose that a combination of crystal unit cell expansion during gold growth, as well as the distortion or collapse of neighboring empty pores, gives rise to the overall resulting increase of 20% CJ crystal surface area after gold growth. We see from elemental analysis that there are still many empty pores during gold growth that may be able to collapse, as we are only filling a small percent of the total CJ pore volume (Fig. 3.42).

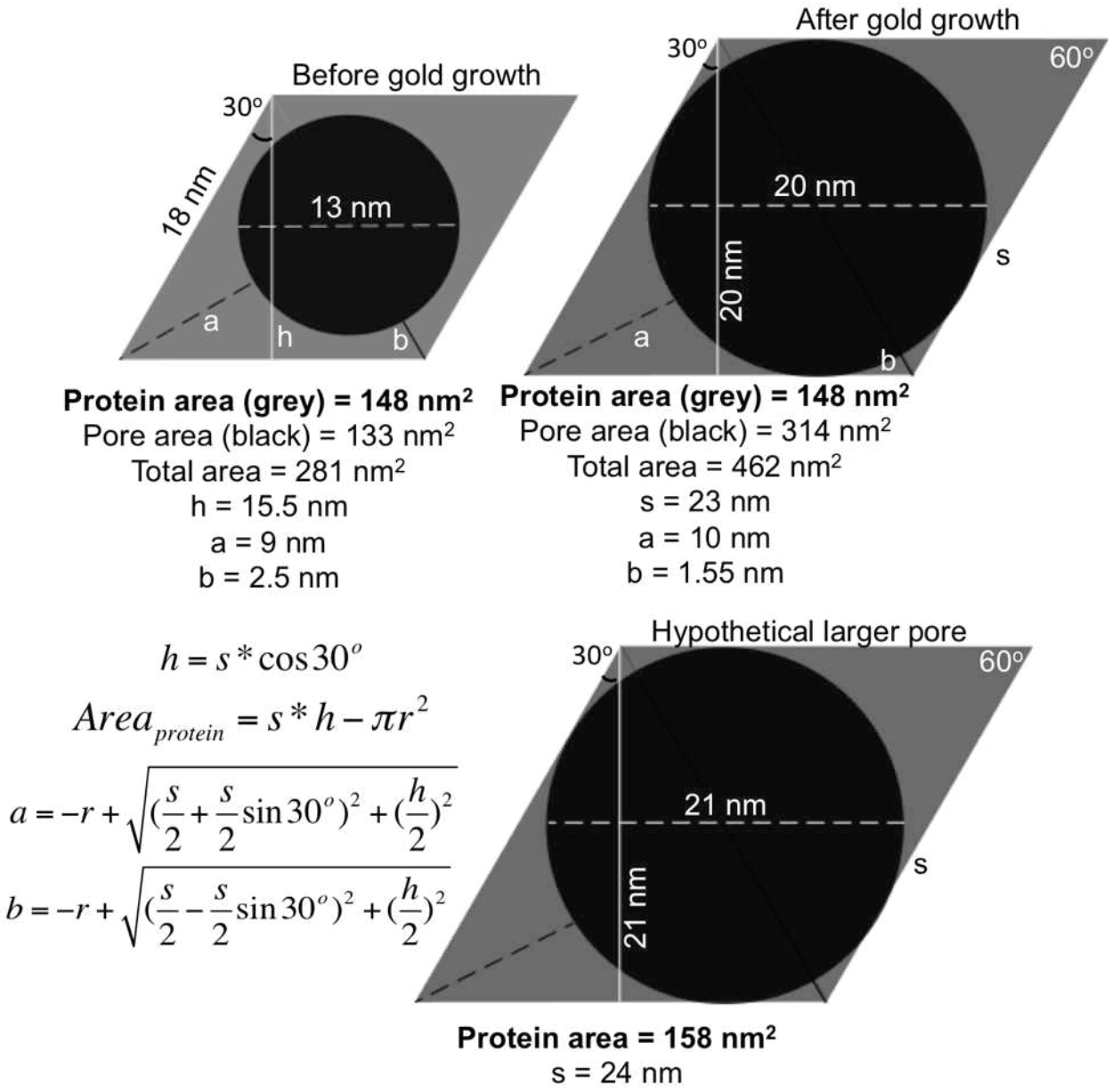


Figure 3.23 Proposed model for crystal expansion during gold growth.

The top left schematic shows the translated unit cell of an empty CJ crystal. The protein area, in grey, is 148 $nm^2$ and the pore area, in black, is 133 $nm^2$. In order for a rod to grow to 20 nm in diameter, the translated unit cell would need to resemble the schematic on the top right, where the protein area remains the same (no more protein is added to the crystal) but the pore area expands. For a pore to expand to more than 20 nm in diameter, a schematic like the bottom right would need to occur, in which the total protein area would have to become larger in order to incorporate the pore.

To further explore how the gold growth can distort the protein crystal pores, we used 1% glutaraldehyde as an alternate crosslinker to EDC. Glutaraldehyde is a more aggressive crosslinker, and we hypothesized that rods grown within the pores of glutaraldehyde-crosslinked CJ crystals would have smaller diameters than those grown in EDC crosslinked crystals. Most rods were superimposed on others in the bundle they existed in so only a small amount of these rods were able to be accurately measured. The average width of rods growth in this type of crosslinked crystal was 15.2 nm with a standard deviation of 1.7 nm (n=19). These results may suggest that rods grown in crystals with more rigorous crosslinking will have an overall smaller width due to a more the more rigid protein crystal.

*Gold growth with thiolated precursors*

One way to minimize the intrinsic reducing ability of the protein is to use a more stable soluble gold precursor. Sodium aurothiosulfate ($Na_3Au(S_2O_3)_2$), henceforth referred to as Au(I), is much less reactive than $HAuCl_4$ because of the surface gold-sulfur bonds. It requires a stronger reductant, like sodium borohydride ($NaBH_4$), to induce growth. Unlike with Au(III) ions from $HAuCl_4$, when a crosslinked crystal is placed in Au(I) overnight, no color change occurs (Fig. 3.25).

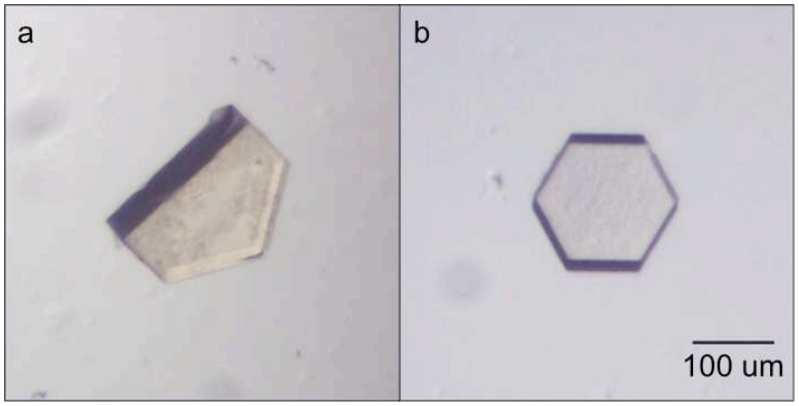


Figure 3.24 Effect of gold salt choice on autonucleation

An EDC crosslinked CJ crystal after incubation in (a) 10 mM $HAuCl_4$ or (b) 10 mM Au(I) for 16 hrs.

Various experiments were performed in solution by our collaborators in the Ackerson Lab (Department of Chemistry, Colorado State University) to find optimum ratios and concentration of both Au(I) and $NaBH_4$. All of these experiments were performed in water. Final solution concentrations were varied, but a 1:10 molar ratio of Au(I) to $BH_4$ was used in all experiments. There was some kinetic difference between seeded and unseeded growth using this method, as shown in Figure 3.26. The biggest downside to this method is the timescale. In order to prevent self-nucleation, low concentrations must be used, which means growth takes place over up to five days. Additionally, there is always some color change in the crystal that is not loaded with $Au_{25}$, indicating some self-nucleation even at the lowest concentrations. Some variability is typically apparent between experiments (Fig. 3.27), which we attribute to batch-to-batch inconsistency in the reductant. Other groups have reported that even fresh borohydride solution can have variable reactivity.[127]

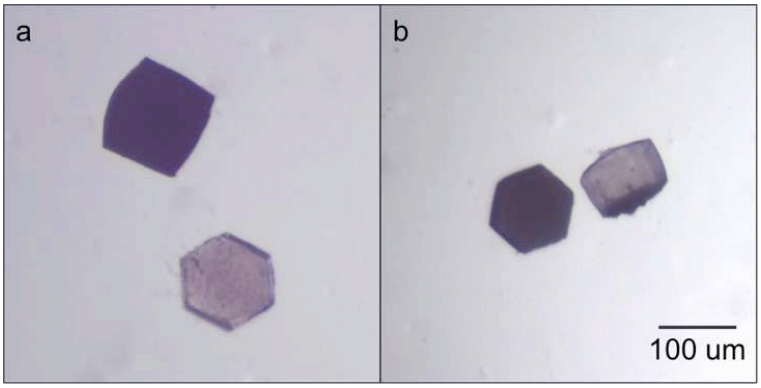


Figure 3.25 Seeded and unseeded growth with Au(I) salts

(a & b) Two examples of typical seeded (black) versus unseeded (grey) growth using Au(I) and $BH_4$ in EDC crosslinked crystals. Seeded crystals are black, unseeded crystals are lighter grey. Crystals were grown in a solution of 1 mM Au(I) and 10 mM $BH_4$ for 16 hrs.

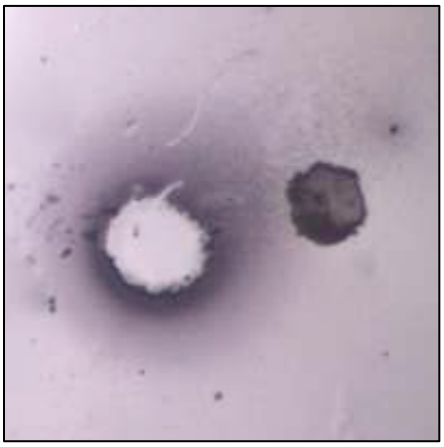

Figure 3.26 Autonucleation event with Au(I) salts

An unseeded, EDC crosslinked CJ crystal after 24 hrs in 1 mM Au(I) and 10 mM $BH_3CN$. Spontaneous nucleation occurs in and around the crystal, even without a seed present. Note: crystal has been moved to the right of its original location for imaging. Crystal is 100 μm in diameter.

We dissolved some of the most successful attempts at seed-mediated Au(I) gold nanorod growth to view by transmission electron microscopy (Fig. 3.28). We found that

the seeded crystal (panel a) contained many large particles and other amorphous structures, while the unseeded crystal (panel b) was almost entirely empty.

However, as with most of the growth methods outlined in this paper, there were inexplicable instances where unseeded crystals (which should not contain defined nucleation points for gold growth) spontaneously grew gold structures as evidenced by their color change (Fig 3.27).

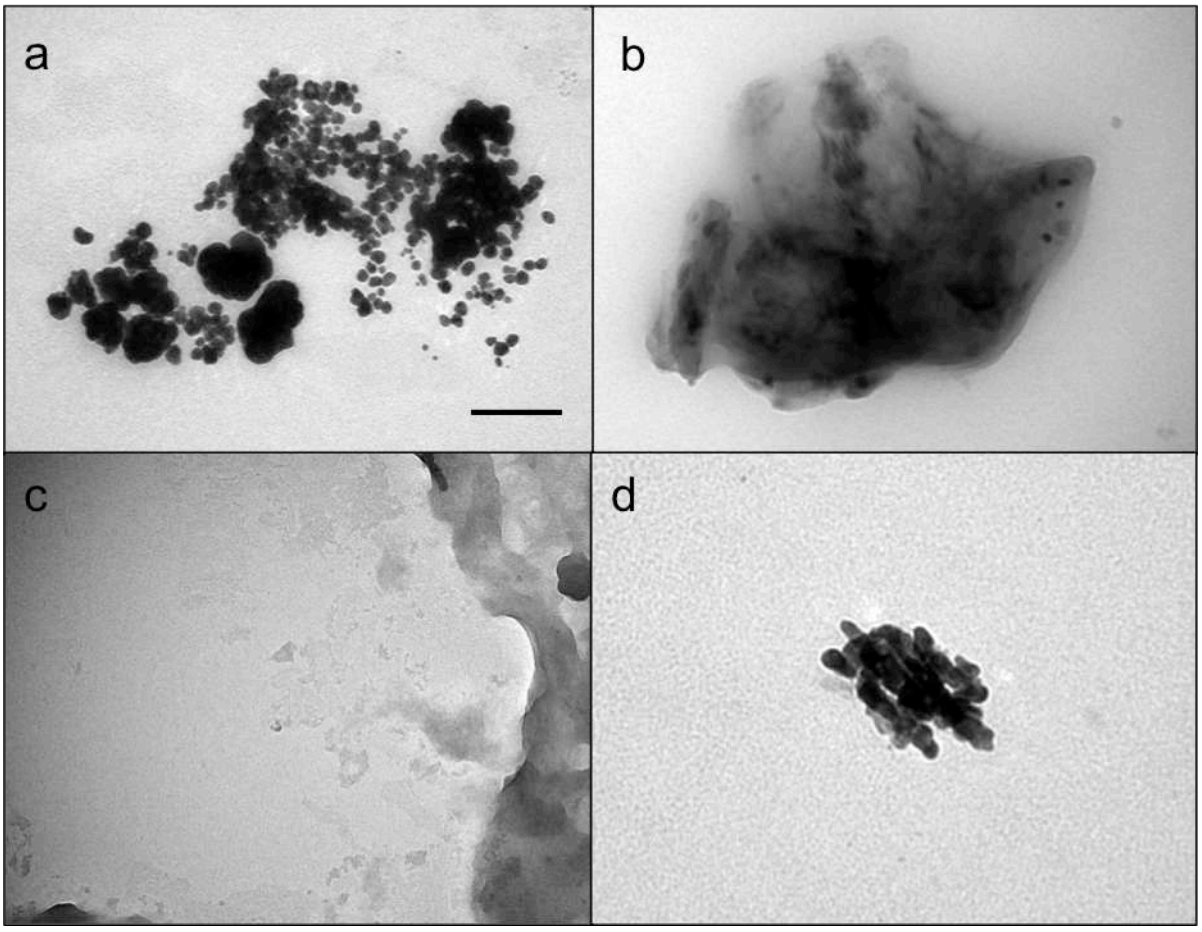


Figure 3.27 TEM of resulting gold structures from seeded and unseeded growth with Au(I)

Transmission electron microscopy of crystals from Figure 3.26. A CJ crystal that has been loaded with $Au_{25}$ (a, b, d), subjected to gold growth by Au(I) and $NaBH_4$, and then dissolved, contains mostly gold particles (a, b) and rod bundles (d). A CJ crystal that was unseeded upon gold growth (c) remains devoid of larger gold particles. Scale bar is 100 nm. *Image: R. Nemeth*

*Gold growth with surface passivating agents*

Another way to reduce self-nucleation of gold ions is to introduce protecting groups and capping ligands in the growth solution. Sometimes CTAB is used for this purpose (as well as to encourage rod growth instead of spherical growth),[134] but CTAB has low solubility in water and tends to destabilize our crystals.

Instead we modified a protocol from Gao et. al. in which gold and silver nanorods are grown within silica nanotubes by a seed-mediated approach.[135] Their use of potassium iodide (KI) and polyvinylpyrrolidone (PVP) allow the use of higher concentrations of $HAuCl_4$ and ascorbic acid without spontaneous nucleation. KI reacts with $AuCl_4^-$ to form $AuI_4^-$, which is a stable complex with a lower reduction potential than $AuCl_4^-$. PVP caps the $AuI_4^-$ monomers, further slowing growth and delaying self-nucleation. Additionally, PVP should prevent the final products from aggregating.[135]

In our modified protocol, after crystal stabilization by crosslinking, loading $Au_{25}(GSH)_{17}NTA$, binding with Ni(II), and washing, crystals are placed in a growth solution. The growth solution consists of 40 uL of 0.38% PVP w/v (3500 MW), 15 mM KI, 7.6 mM ascorbic acid, and 2.85 mM $HAuCl_4$, well stirred. The growth solution stays stable (clear in color) for at least two hours. When the crystals are placed in the growth solution, a crystal loaded with $Au_{25}(GSH)_{17}NTA$ will turn black within 10 mins, while an empty crystal will remain clear indefinitely (Fig. 3.29).

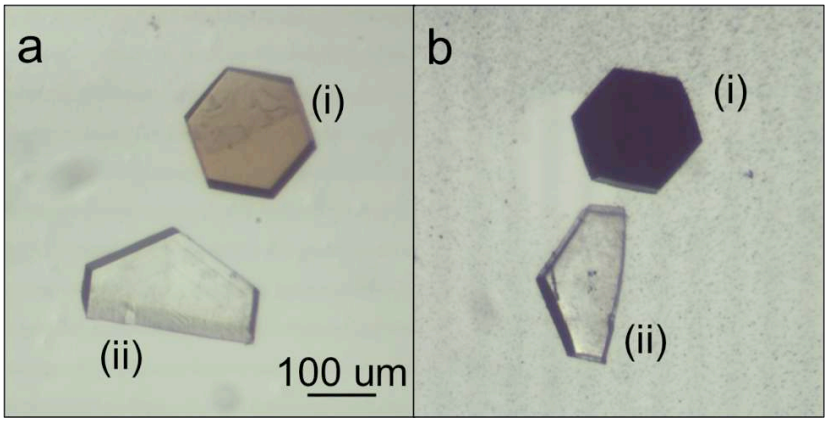


Figure 3.28 Effect of surface passivating agents on controlled gold growth

(a) A seeded (i) and an unseeded (ii) CJ crystal in the PVP and KI growth solution at t = 0 mins. (b) The same crystals in the growth solution at t = 10 mins

Figure 3.30 shows TEM of the structures resulting after the crystal scaffold was dissolved. The heavily grown crystals may not have been completely dissolved by our methods, but the periphery of the structure does suggest the presence of some short rods and bundles.

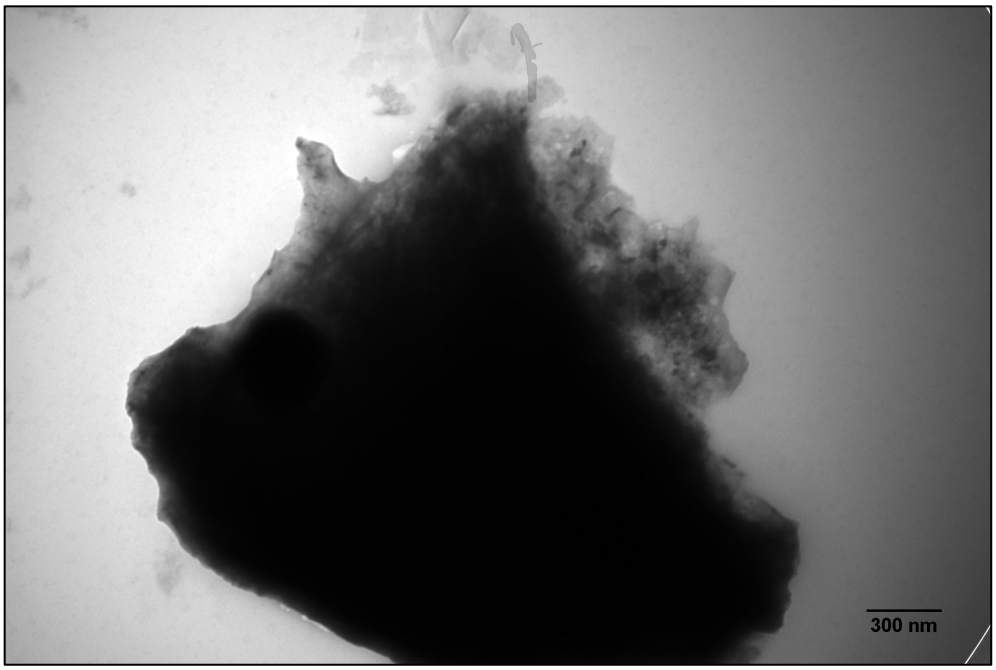


Figure 3.29 TEM of partially dissolved protein matrix

TEM images of the structures resulting after a crystal is subjected to the above growth protocol and then dissolved. The image resembles an incompletely dissolved crystal, where the interior gold structures are still connected by partially denatured protein. Some structures around the periphery resemble short rods and bundles. Scale bar is 300 nm. *Image: R. Nemeth*

We checked these samples for complete growth through the interior of the crystal by cutting open CJ crystals (Fig. 3.31); we saw that the interior of the crystal was filled with gold.

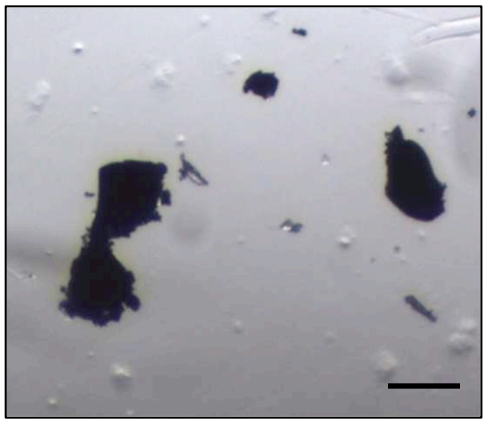

Figure 3.30 Gold growth throughout a crushed crystal

A crystal grown in the presence of PVP and KI and cut into three pieces to reveal gold growth throughout the interior. Scale bar is 100 μm.

*Gold growth in 3oc4 crystals*

In order to demonstrate the versatility of this method for synthesizing gold nanostructures in arbitrary shapes, we prepared an alternate protein crystal scaffold. The protein crystal (PDB code 3oc4), crystallizes with 9 nm and 5 nm cylindrical axial pores and 5 nm lateral pores (Fig. 3.32).

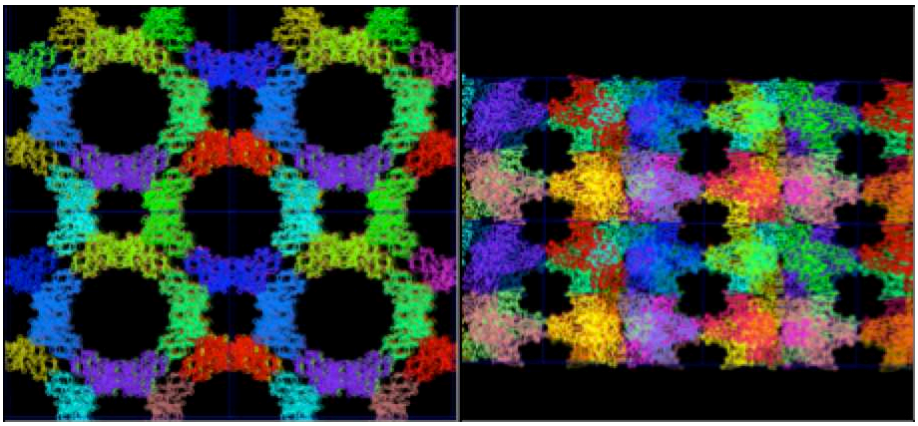

Figure 3.31 3oc4 Pymol schematic

Molecular Python (Pymol) schematics of the top (left) and side (right) view of a 3oc4 crystal. The crystal contains 9 nm axial pores (left) and 5 nm lateral pores (right).

We hypothesized that we could grow gold nanorods by the same method within the pores of 3oc4, and when the crystal was dissolved, we would see gold nanostructures that matched the dimensions of the scaffold. Figure 3.33 shows the general topology of a 3oc4 crystal, as well as its color after loading 10 mM $HAuCl_4$ for 1 hr (a) and 10 mM ascorbic acid for 1 hr (b). Figure 3.34 shows the results of dissolved TEM of these crystals. We can see ~ 5 nm diameter rods embedded within sections of undissolved protein.

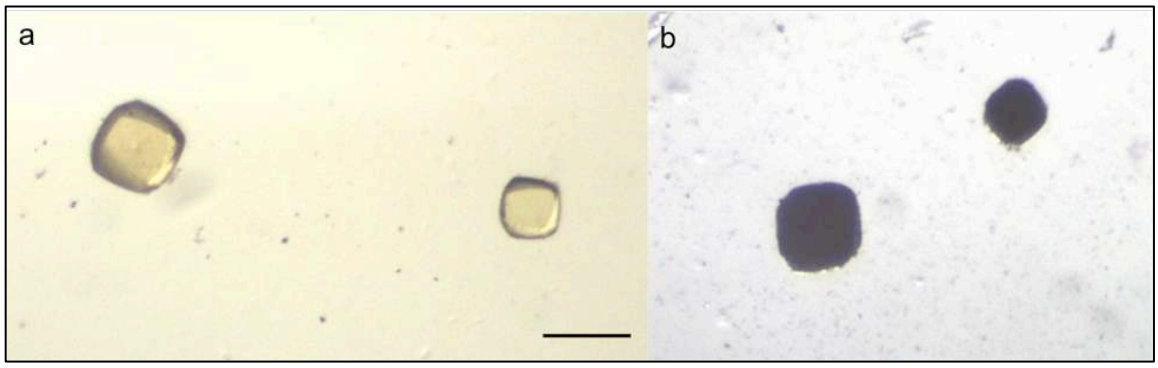


Figure 3.32 Gold growth within 3oc4 crystals

(a) Crosslinked 3oc4 crystals previously loaded with $Au_{25}$, now adsorbing 10 mM $HAuCl_4$ for 10 mins. (b) The 3oc4 crystals from (a) after 1 hr in 10 mM ascorbic acid.

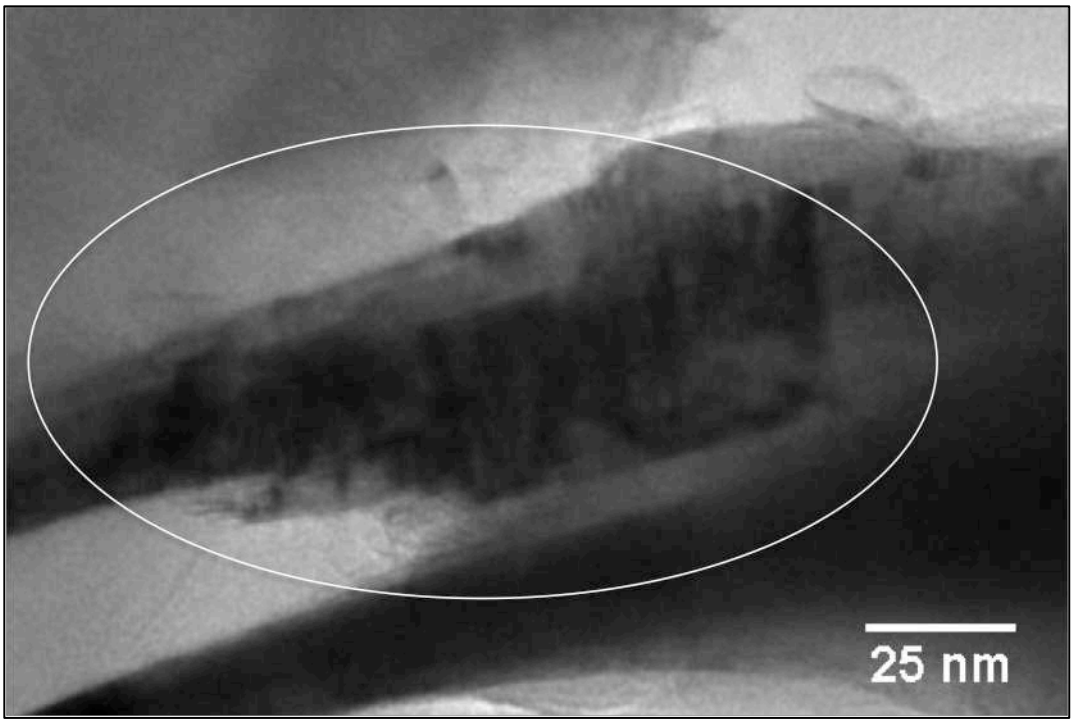


Figure 3.33 TEM of 3oc4 protein/gold matrix

TEM of rods released from 3oc4 crystals that have been loaded with $Au_{25}$ and soaked in 10 mM $HAuCl_4$ for 10 mins followed by 10 mM ascorbic acid for 1 hr. Image shows rods ~5 nm in diameter partially embedded within denatured protein. *Image: R. Nemeth*

*Dissolving crystals for TEM of released nanorods*

Visualization of rods was done by transmission electron microscopy, most commonly after the rods were freed from the scaffold by dissolving the protein crystal. Uncrosslinked CJ protein crystals are easy to dissolve simply by placing them in a solution of lower salt than their growth condition; however, chemical crosslinking by EDC or glyoxal adds considerable stability. For example, we have shown that crosslinked protein crystals can survive a challenging range of solution conditions, including organic solvents and extreme pHs (Fig. 3.35).

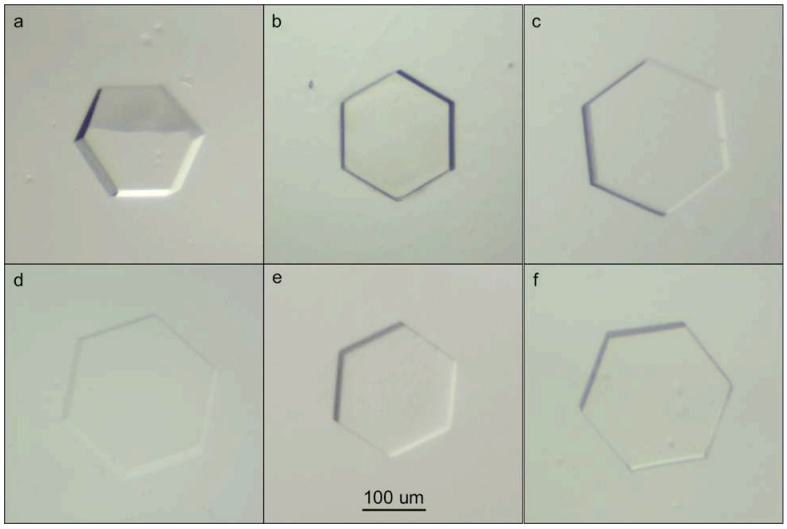


Figure 3.34 Stability of CJ crystals after crosslinking

A glyoxal crosslinked CJ crystal after 2 mins in (a) $H_2O$, (b) 100% acetone, (c) 100% DMSO, (d) 100$^oC$ $H_2O$, (e) aqua regia, and (f) pH 11 NaOH buffer. Aqua regia is a 3:1 v/v mixture of pure hydrochloric acid (HCl) and nitric acid ($HNO_3$).

We attempted a variety of dissolving methods to find which one retained the best gold nanoparticle structure. The standard protocol was to soak crystals in 200 µL of 0.5 M NaOH. In this condition, dissolving could take up to 7 days for the largest, most heavily grown crystals. The following section summarizes the dissolving methods explored in collaboration with the Ackerson lab in the Chemistry Department at Colorado State University. Extended dissolving time can allow for product etching and the conversion of nanorods to nanoparticles, which is supported by previous studies.[152]

We were able to add head (up to 40$^oC$) and stirring (200 rpm) without significant damage to the products. This sped up the time required to dissolve crystals. A three-minute water bath sonication of the dissolving samples had no noticeable effect on the quality of the nanorods observed. Adding 0.1 M glutathione (GSH) to the dissolving solution helped to break apart gold nanorod clumps, by providing a surface stabilizing

agent. However, if the rods were left exposed to GSH for too long while dissolving, the GSH could etch the rods, leading to an average diameter of 13.5 nm, instead of the typical 19.4 nm. In general, these methods were only employed for large crystals that were heavily grown with gold; these samples were the most difficult to dissolve.

Examples of promising but unsuccessful dissolving methods included the use of a 0.1 M cyanogen bromide solution that should cleave the protein backbone adjacent to the C-terminus of methionine residues in the protein crystals. CJ has 3 methionines per monomer. However, the chemical crosslinks and interconnects in the rods still prevented the crystals from dissolving. A combination of 4.2 M guanidine hydrochloride (GdnHCl) and 15% hydroxylamine denatured the protein and cleaved ester bonds in EDC crosslinks, respectively. This was successful, but we found that hydroxylamine was significantly etching rods and making it difficult to interpret our products on TEM (Fig. 3.36).

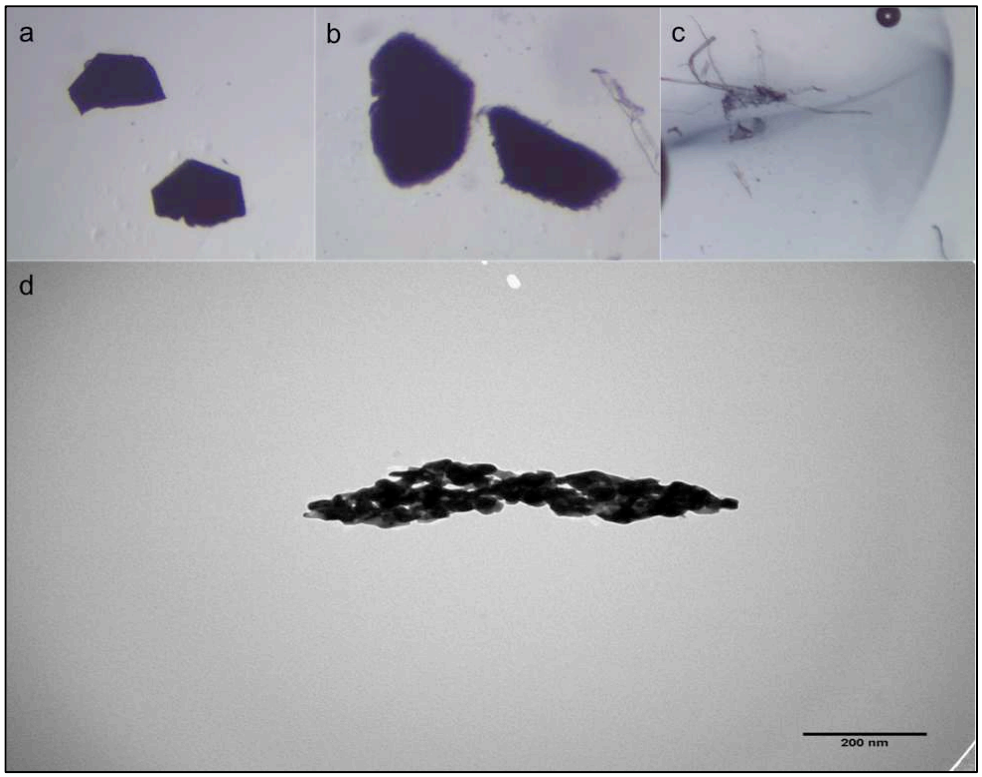


Figure 3.35 CJ crystal dissolving timelapse

A gold grown CJ protein crystal in a 10 uL drop of 4.2 M GdnHCl and 15% hydroxylamine at (a) t = 0, (b) t = 4 hrs, and (c) t = 16 hrs. By 16 hrs, the crystal has dissolved and gold nanostructures remain visible in the drop of liquid. (d) TEM images of the gold structures resulting from the above sample. Although this solution completely dissolved the protein crystal, it also appeared to etch the gold products. Some hint of rods remain, but are difficult to interpret. Original crystals (a) were approximately 200 μm in size, and expand in GdnHCl (b). Scale bar for (d) is 200 nm.

We often found that using much smaller crystals aided in our ability to quickly dissolve the samples and release the gold nanorods for imaging. Typical CJ protein crystals are between 100 um and up to 1 mm. By altering the crystal growth conditions, crystals under 1 um in diameter can be grown.

These “microcrystals” are prepared by a batch method. Instead of individually transferring or looping each crystal into a new solution, a 1 mL sample of microcrystals can be moved to each new solution (i.e. crosslinking, quenching, $Au_{25}$ loading, etc.) by

centrifugation and supernatant removal. By this method, we were able to synthesize many microcrystals filled with gold at one time. Additionally, these microcrystals dissolve much more quickly than their larger counterparts. Microcrystals were dissolved using a standardized method: 10 µL of microcrystals suspended in $H_2O$ were added to 500 µL of dissolving solution (0.5 M NaOH, 0.1 M GSH) and put in an oven at 35$^{o}$C for 4 hours. The products were centrifuged at 14,000 rpm for 30 minutes and the supernatant was discarded. Products were then re-suspended in water.

*In-crystallo imaging*

In order to confirm that these rods were actually being grown within the crystal pores, we attempted to image intact crystals after the gold growth protocol.

Embedded and ultramicrotomed grown samples were unsuccessful. It was apparent when cutting the thin sections that the difference in mechanical properties between the gold and the protein/resin was causing the sample to warp or shear when cutting, which is a common problem when imaging composite materials.

Next, we attempted scanning electron microscopy (SEM) on gold grown crystals that were cut into pieces to expose the interior of the crystal. Figure 3.37 shows that while cutting/smashing the crystals clearly caused damage to the protein, the bright spots of high electron density suggest the presence of gold structures throughout the crystal.

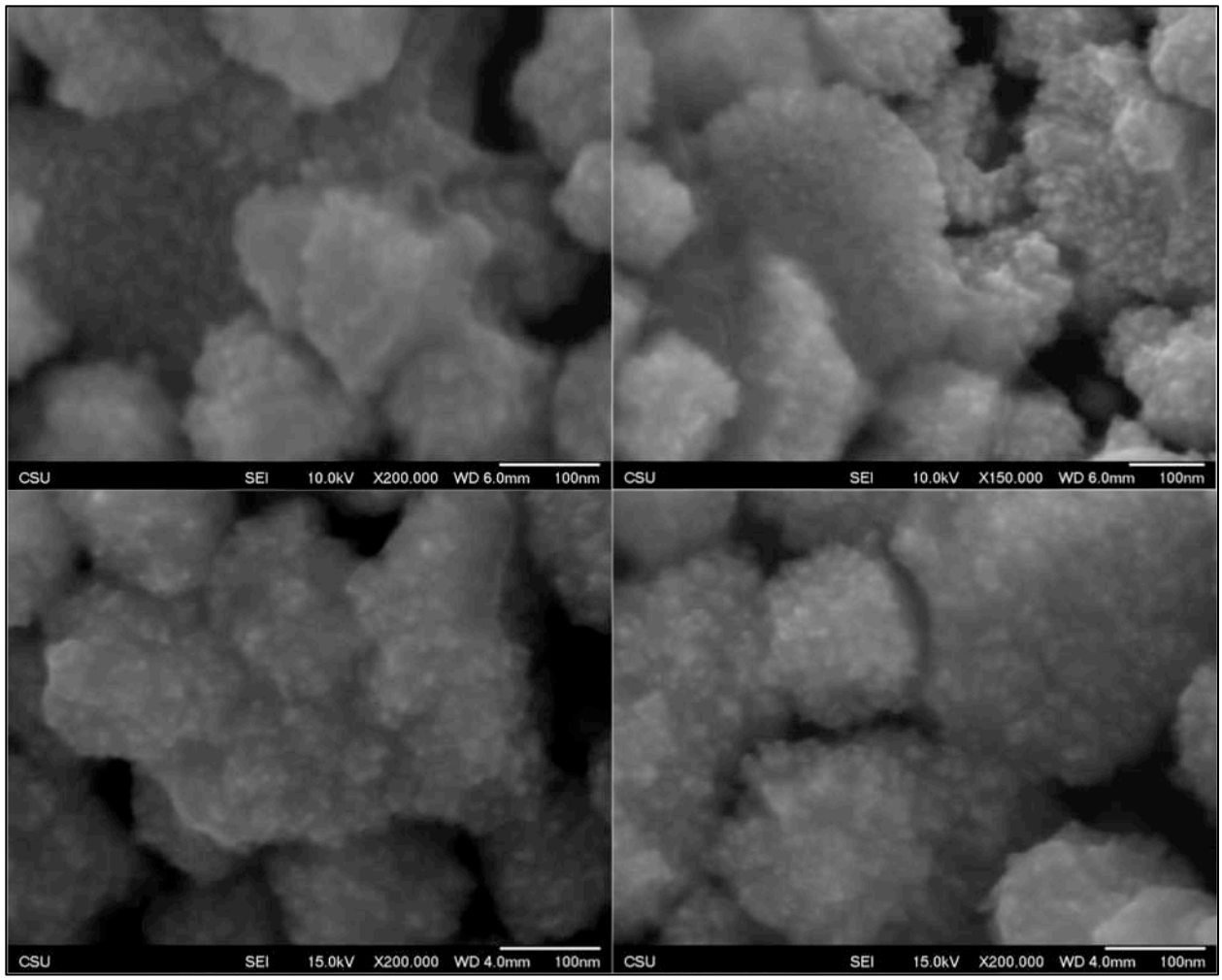


Figure 3.36 SEM of a smashed CJ crystal/gold matrix

Scanning electron microscopy images of various portions of a gold grown CJ crystal cut to expose the interior of the crystal.

Given the possibility for distortion during cutting, we next fractured grown crystals under liquid $N_2$ to help preserve their structure. Specifically, liquid $N_2$ was poured into a well containing gold grown crystals. A frozen crystal manipulation tool was used to crush the crystal sample. The frozen pieces were then transferred to a TEM grid. Figure 3.38 shows the results of this imaging method. Panel a suggests the presence of a ~20 nm electron dense rod that is half exposed and half crystal embedded after the

shattering procedure. Panel b again suggests the presence of ~20 nm electron dense rods still completely embedded in the crystal after shattering. Panel c shows evidence for potential lateral pore growth with parallel ~3 nm rods embedded within the crystal. Panel d shows a zoomed in view of the thin rods from panel c.

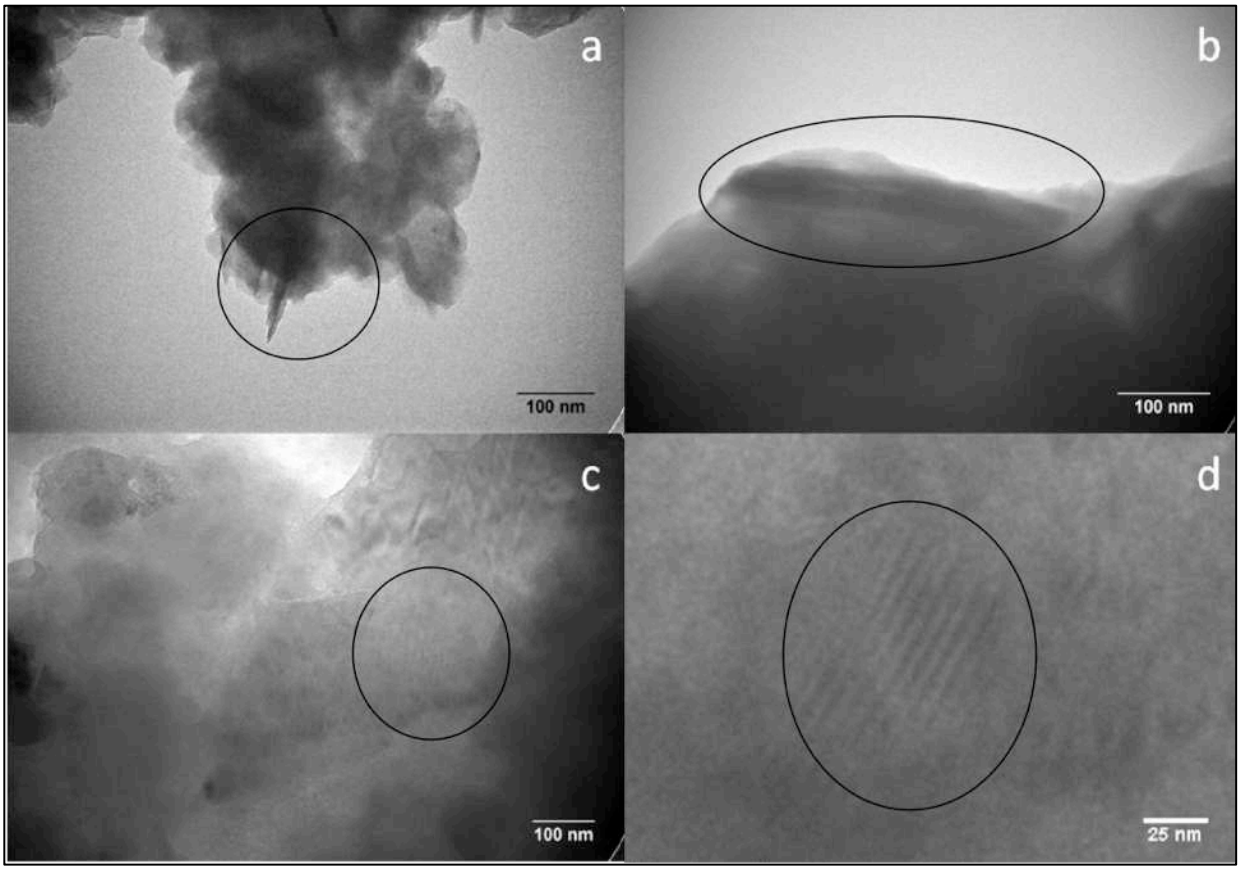


Figure 3.37 TEM of crystal/gold matrix

TEM images of gold grown CJ protein crystals frozen under liquid $N_2$ and shattered to reveal the interior of the crystals. (a) Gold nanorod, partially crystal embedded and partially exposed. (b) Two nanorods trapped within the crystal. (c) Evidence for axial pore growth within the crystal. (d) Zoomed in section of the approximately 3 nm rods embedded in the crystal from panel c.

Additionally we attempted to confirm the presence of gold through energy-dispersive X-ray spectroscopy (EDS) of thick sections of grown crystals. We again resin

embedded gold grown CJ crystals (by the same method described for the ultramicrotome), but instead used a glass knife to cut thick sections (2-3 um) of the sample. These were placed on a grid for SEM/EDS imaging. By EDS, we were able to detect significant presence of gold within the interior of the crystal. However, the crystal and resin surrounding the embedded sample was very beam sensitive and prevented viewing and focusing on the sample for extended periods of time due to beam damage.

Because we are able to grow microcrystals that are less than 1 um in diameter and theoretically less than 200 nm in thickness, we attempted to visualize intact, gold grown crystals by TEM (Fig. 3.39). Unfortunately at room temperature the samples are too sensitive for the amount of beam power that would be required to image at the needed resolution. Additionally, we believe that the distance between axial pores in the CJ crystal (<3 nm) nears the resolution limit to detect separation between gold rods in adjacent pores.

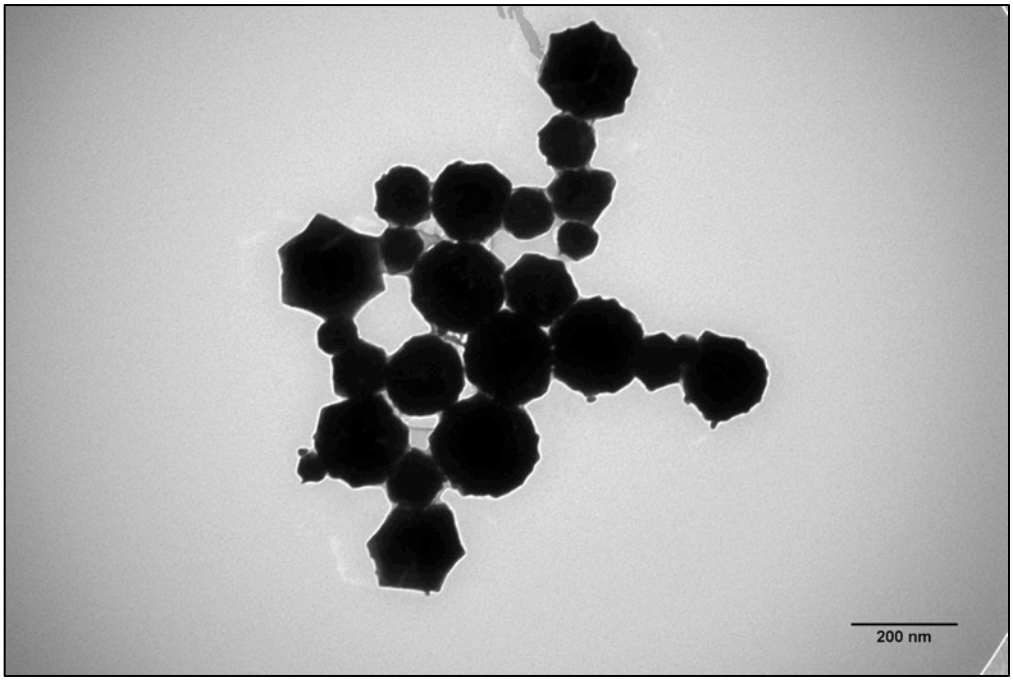


Figure 3.38 TEM of intact microcrystals after gold growth.

*UV-Vis-NIR spectroscopy*

A common method for bulk characterization of gold nanostructures is UV-Vis-NIR spectroscopy. Because the absorbance spectra from gold is highly related to the size and shape of the nanostructures, it may be possible to determine the composition of a sample through spectroscopy.

In order to monitor the real-time absorbance of a crystal during a typical gold growth protocol, we fabricated a simple spectroscopy system (Fig. 3.40). A Flame spectrometer (Ocean Optics) was SMA-coupled to a bare, 200 μm inner diameter fiber optic cable (Ocean Optics). An identical fiber optic cable was coupled to a stabilized Tungsten/Halogen light source (ThorLabs, SLS201L). Both cables were superglued to a glass slide with a ~200 μm gap between, where a crystal could be placed in a 20 μL drop of solution. The slide could be sealed with a glass coverslip and vacuum grease to prevent evaporation during the experiment. While reading, the entire setup was covered with a box to prevent spectra variations from ambient light.

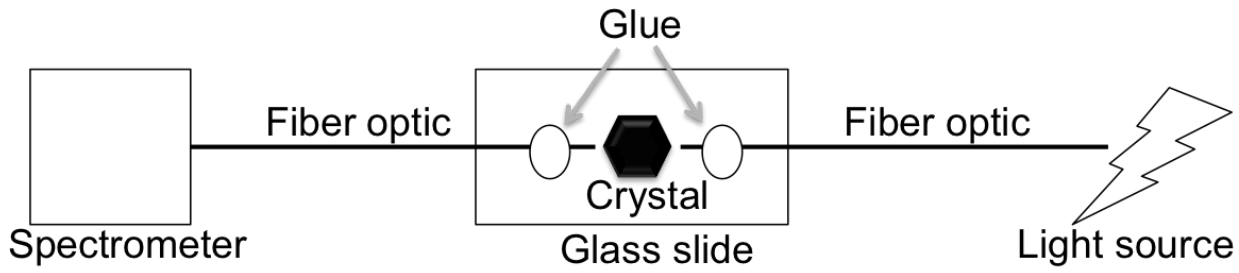


Figure 3.39 Spectrometry setup

A Flame spectrometer (Ocean Optics) was SMA-coupled to a bare, 200 μm inner diameter fiber optic cable. An identical fiber optic cable was coupled to a stabilized Tungsten/Halogen light source (ThorLabs, SLS201L). Both cables were superglued to a glass slide with a ~200 μm gap between.

Gold growth was monitored over time for a crystal loaded with $Au_{25}$ and 10 mM $HAuCl_4$, then placed in a drop of 5 mM ascorbic acid between the fiber optic cables on the glass slide. The crystal was placed in either lateral and axial orientations (Fig. 3.41).

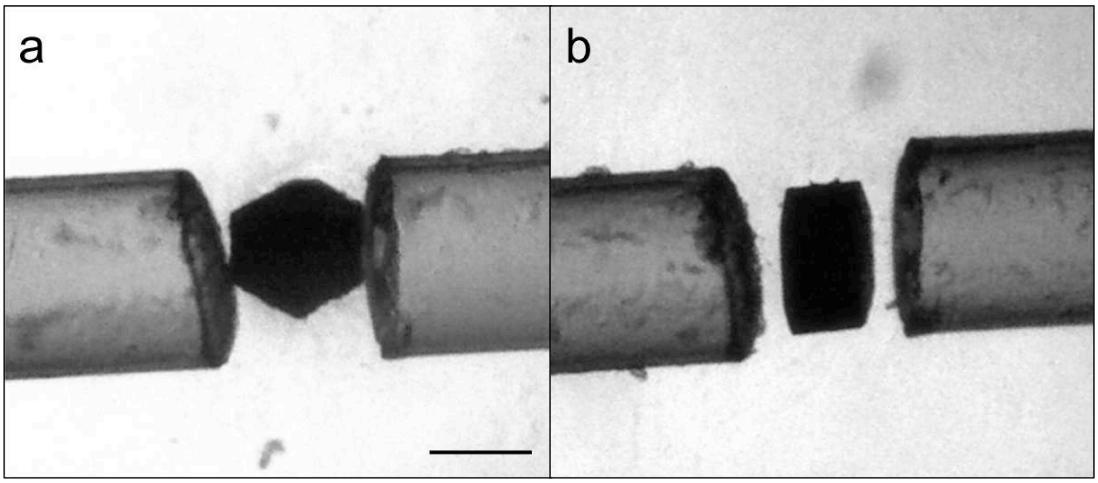


Figure 3.40 Crystal orientations for spectrometry

A crystal was placed either laterally (a) or axially (b) between two fiber optic cables. Both images depict a crystal following the growth protocol, where the crystal looks black by eye. Scale bar is 100 μm.

Prior to testing gold nanorod growth using the stabilized Tungsten/Halogen light source, we built a prototype spectrometry in a similar setup using a 60W incandescent lightbulb, which is a broadband lightsource with a much weaker output than the Tungsten source. Figure 3.42 shows results from timelapses of gold growth within a CJ crystal in the lateral orientation (a) and in the axial orientation (b) using the incandescent bulb. In the lateral orientation, the light is perpendicular to the 13 nm diameter pore of the crystal and thus the electric field is parallel to rod growth. Surface plasmon resonance from gold nanorods should be apparent in this direction. In the axial orientation, absorbance should come from primarily surface plasmon resonance of gold nanoparticles within the pores. In the lateral orientation (3.42a) the absorbance peak around 450 nm indicates the presence of $Au_{25}$. Over time, the absorbance of this peak

grows only slightly, indicating more particles of this size do not form. Instead, a broad peak from 600 - 900 nm, already present at the early timepoints, grows over time. Broad absorbance peaks from 500 - 900 nm are characteristic of gold nanoellipses and nanorods. The broad spectrum indicates the presence of many gold species, which supports our findings through TEM that there are a variety of gold nanoproducts formed with each growth protocol. At the t = 0 min timepoint, it's possible that growth has already begun as the crystal was placed in the reducing solution and oriented between the fiber optics prior to the start of the experiment. At the later timepoints, the optical density of the sample seems to obscure any discernible peaks.

In the axial orientation, the 450 nm wavelength peak is pronounced at t = 0 min, again suggesting the presence of $Au_{25}$. This peak grows significantly over time and shifts right, suggesting that more particles are forming in this orientation and growing slightly (to 13 - 20 nm in diameter) over time. In this orientation, the density of the crystal also saturates the absorbance at later timepoints. Additionally, it is likely there is bulk gold growth on the surfaces of the crystal at later timepoints, which contributes to the broad spectrum absorbance. The absorbance values from the lateral and axial orientation cannot be directly compared as the path length of the sample was different in each orientation (as seen in Figure 3.41).

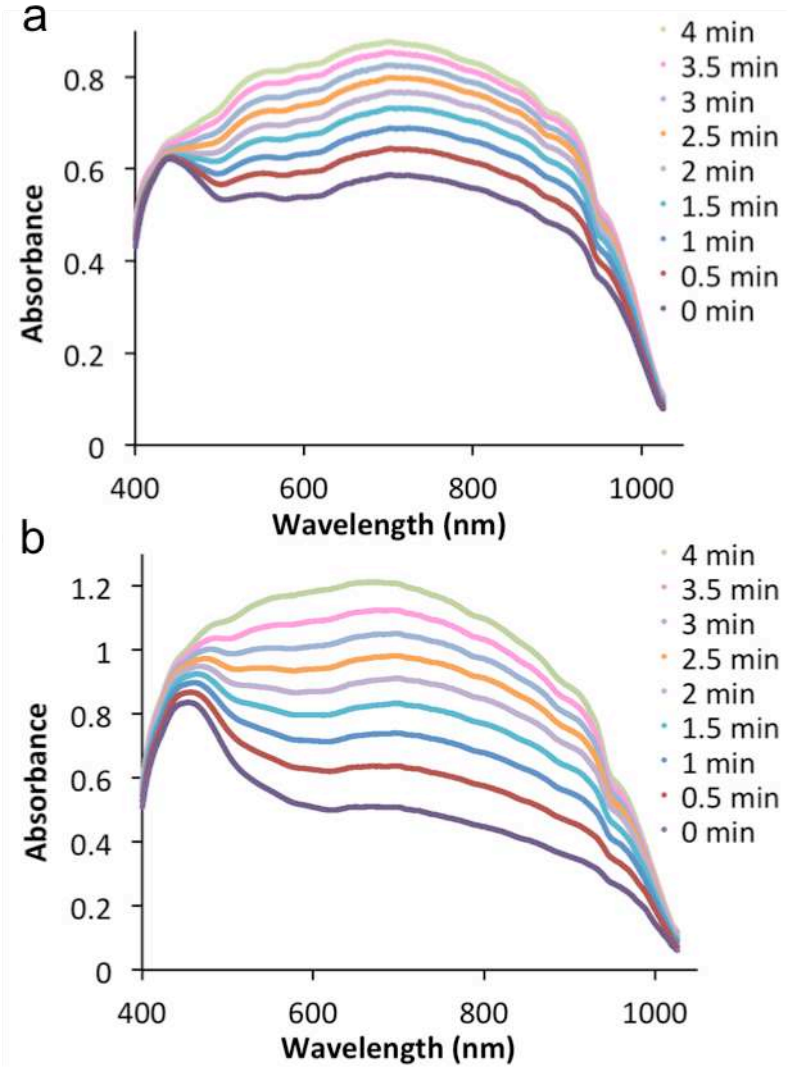


Figure 3.41 Lateral (a) and axial (b) gold growth within a crystal.

Results from gold nanorod growth using the spectrometry setup in Figure 3.40 with a 60W incandescent bulb. The crystals were loaded with $Au_{25}$, then 10mM $HAuCl_4$ prior to incubation in 5 mM ascorbic acid for growth monitoring. Crystals were placed in the lateral (a) or axial (b) orientations. Absorbance was calculated as the negative logarithmic of the transmittance as measurement by a Flame Spectrometer from Ocean Optics.

Figure 3.43 shows the results from gold growth within a crystal using the Tungsten/Halogen light source. Overall with this lightsource, a much lower percent of the light is absorbed by the sample. At early timepoints in the lateral orientation (Fig.

3.43a), a large peak is apparent around 500 nm wavelength, indicative of the presence of many small gold nanoparticles between 13 - 20 nm in diameter. There is broad absorbance from 500-900 nm even at the first times which rises as the optical density of the sample grows.

In the axial orientation (Fig. 3.43b), where rods are parallel to the direction of light, there is again a large peak from 450-500 nm, indicating many gold nanoparticles within the sample. At the early timepoints, there is no indication of larger gold structures in the sample. Over time, the 500 nm peak grows and shifts towards longer wavelengths, suggesting that the particles are growing slightly in diameter.

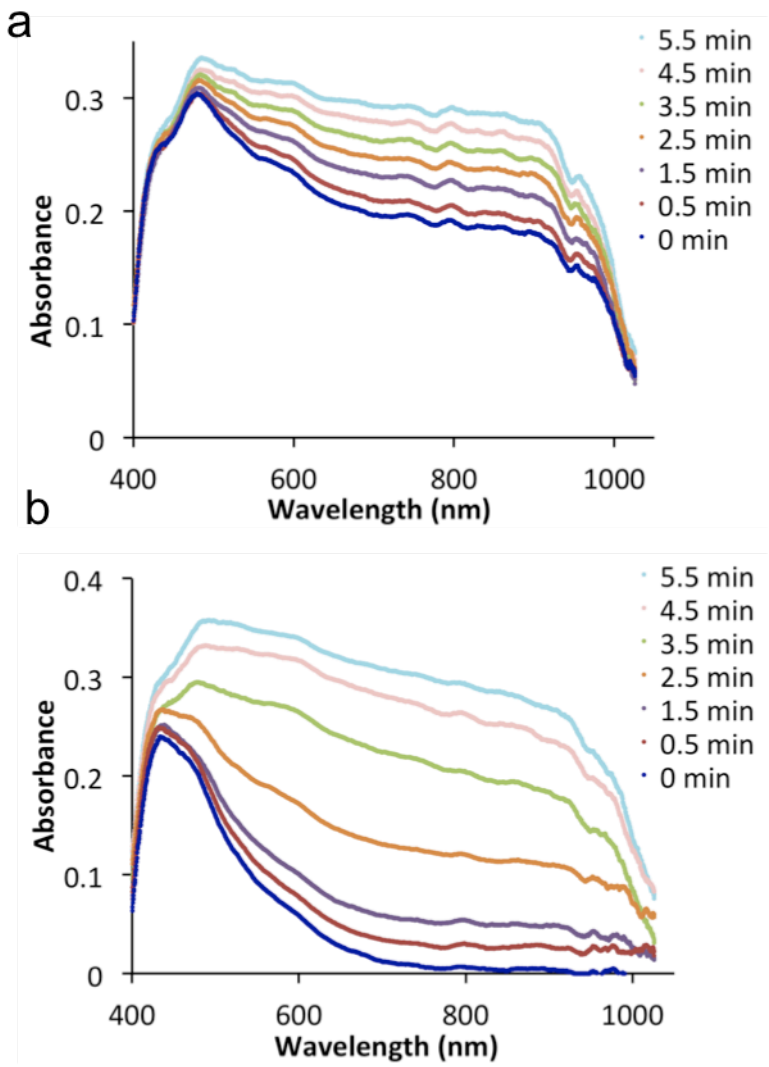


Figure 3.42 Lateral (a) and axial (b) gold growth within a crystal.

Results from gold nanorod growth using the spectrometry setup in Figure 3.40 with a Tungsten/Halogen light source. The crystals were loaded with $Au_{25}$, then 10mM $HAuCl_4$ prior to incubation in 5 mM ascorbic acid for growth monitoring. Crystals were placed in the lateral (a) or axial (b) orientations. Absorbance was calculated as the negative logarithmic of the transmittance as measurement by a Flame Spectrometer from Ocean Optics.

*Elemental analysis*

Elemental analysis was performed on protein crystals after gold nanorod synthesis within the pores, in order to analyze the overall quantity of gold within the crystal. The elemental analysis samples consisted of three replicates, each containing three crystals and dissolved in 2 mL of aqua regia. Volumes were calculated by measuring the surface areas and heights of the crystals using a calibrated optical microscope. Samples were prepared by loading crosslinked CJ crystals with $Au_{25}(GSH)_{17}NTA$ overnight, binding the seed with Ni(II), moving the crystal to a drop of 10 mM $HAuCl_4$ for 1 hr, and lastly reducing the gold in a drop of 10 mM ascorbic acid until black. Elemental analysis was performed at Midwest Laboratories, Inc. Further information regarding *in crystallo* gold loading concentrations and theoretical gold packing calculations can be found in Chapter II.

Overall we found that after standard growth by 1 mg/mL $Au_{25}$, 10 mM $HAuCl_4$, and 10 mM ascorbic acid yielded ~700 gold atoms per crystal unit cell, which is more than twice the concentration achieved by adsorbing 1 mg/mL $Au_{25}$ into the pores for 48 hrs. However, removing the $Au_{25}$ seed and allowing for spontaneous nucleation and growth by 10 mM $HAuCl_4$ and 10 mM ascorbic acid could result in the formation of gold nanorods, but only resulted in an average of ~200 gold atoms per crystal unit cell. This suggests overall fewer nucleation events, leading to the formation of *some* rods and larger clusters but an overall lower amount of gold within the crystal, which is consistent with our observations by electron microscopy.

In comparison, theoretical analysis based on the solvent accessible volume of the crystal pore indicates that a volumetric maximum number of Au atoms per unit cell

would be approximately 60,000. This is an extremely liberal estimate as it uses the atomic radius of gold to calculate the volume occupied by each gold atom, and it assumes that gold atoms can occupy all solvent accessible space. If the Au-Au bond length (0.2884 nm) is included in this estimate, the number of Au atoms per unit cell at closest packing drops to ~9,000. It is likely that there is significantly more pore space available for gold growth (Fig. 3.44).

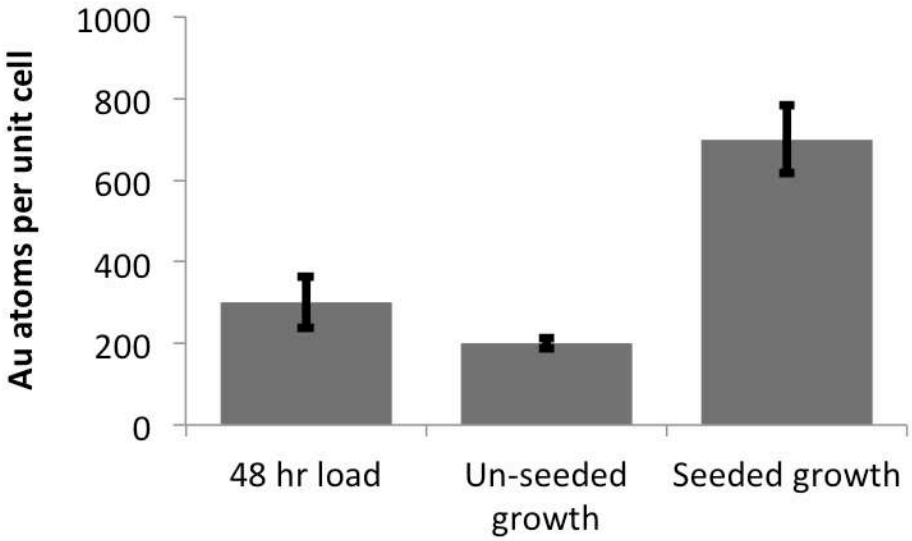


Figure 3.43 Elemental analysis of gold quantity after growth

There are an average of ~300 Au atoms adsorbed into the crystal per unit cell after 48 hrs of loading in 1 mg/mL $Au_{25}$. If standard growth is performed on unseeded crystals (10 mM $HAuCl_4$ followed by 10 mM ascorbic acid), there are only an average of ~200 Au atoms per unit cell. With seeded growth, where crystals are soaked in 1 mg/mL $Au_{25}$ for 30 minutes prior to growth, there are an average of ~700 Au atoms per unit cell. Error bars show standard error of three samples.

## CONCLUSIONS

We have successfully controlled the nucleation and growth of high aspect ratio gold nanorods using 25-atom gold clusters as seeds and protein crystals as designable templates. We have identified conditions such that the growth of rods depends on the presence of a seed and the resulting shape depends on the crystal scaffold used. Growth can occur using a variety of seeds, salts, and reducing agents. Furthermore, the surrounding scaffold can be dissolved, releasing the rods for downstream use. This is a promising new paradigm for the production of designable gold nanostructures.

Like any other nanorod synthesis method described in the introduction, our method deals with product contamination by undesired structures like nanoparticles and ellipses. Although all synthesis methods require a purification step, the nanorods synthesized within our porous protein crystal template do not contain surface ligands which may be toxic and require an additional purification step prior to biological uses. The greatest benefit of using a protein crystal as a template for nanostructure synthesis is that crystals exist with a variety of pore shapes and sizes, which means anisotropic nanostructures of arbitrary morphologies may be synthesized.

## EXPERIMENTAL

### *Reagents*

The following chemicals were purchased from Sigma-Aldrich and used without further purification: Gold (III) chloride trihydrate ($HAuCl_4$, ≥49.0% Au basis), L-glutathione reduced (GSH, ≥98.0%), Boric Acid ($H_3BO_3$, ≥99.5%), Methanol ($CH_3OH$, ≥

99.8%), N,N,N,'N'-Tetramethylethylenediamine (TEMED, ≥ 99%), N-(3-Dimethylaminopropyl)-N'-ethylcarbodiimide (EDC, 98%), polyvinylpyrrolidone (PVP, 40MW), and Ammonium Persulfate (APS, ≥ 98%). The following chemicals were purchased from TCI America and used without further purification: $N^{\varepsilon}$-carbobenzoxy-L-lysine ($N^{\varepsilon}$-Cbz-L-lysine, >98.0%). Other reagents were purchased from Alfa Aesar, Thermo Scientific, and Sigma-Aldrich and used without further purification. Lithium sulfate ($Li_2SO_4$, ≥98.5%). Trimethylamine N-oxide (TMAO, ≥98%). Sodium Thiosulfate Anhydrous ($Na_2S_2O_3$, ≥99%), Sodium Hydroxide (NaOH, ≥99%). Tris Hydochloride ($C_4H_{11}NO_3$, ≥99%), Ethanol (EtOH, ≥88%), Ammonium Acetate ($NH_4OAc$, ≥99%). L-Ascorbic Acid ($C_6H_8O_6$, ≥99%) and Nitric Acid ($HNO_3$, 70% Aqueous Solution) were purchased and used without further purification from Macron Chemicals. Ethylenediamine Tetraacetic Acid (EDTA, ≥99%) and Sodium Borohydride ($NaBH_4$, ≥ 96%) were purchased and used without further purification from EMD Millipore. Acrylamide/Bis Solution (40%, 19:1) was purchased and used without further purification from Bio-Rad.

*Protein Crystal Preparation*

Full sequence information as well as expression and purification protocols for protein CJ (Genebank ID: cj0420, Protein Data Bank code: 2fgs) can be found in the published supplemental information here.[1] CJ was crystallized overnight by sitting drop vapor diffusion in 3.2 to 3.6 M ammonium sulfate and 0.1 M BIS-TRIS at pH 6.5. Crystals were then transferred to a drop of 4.2 M trimethylamine N-oxide (TMAO) and 50 mM imidazole to wash the crystal and equilibrate to the crosslinking solution. Crystals were crosslinked in 4.2 M TMAO, 50 mM imidazole, and 100 mM 1-Ethyl-3-(3-dimethylaminopropyl) (EDC). After two hours in the crosslinking solution, incomplete

crosslinks were quenched in 50 mM borate at pH 10 for 15 mins. After crosslinking and washing, crystals retained smooth, hexagonal morphology and clear color.

Oxidoreductase protein (Protein Data Bank code: 3oc4) from *Enterococcus faecalis* was selected from a scan of the Protein Data Bank for proteins that crystallize with large pores. It was expressed in pSB3 in *E. coli* BL21 (DE3) pLySs using a glucose/lactose induction system at 17 °C for 36 hours.[2] The cells were lysed by sonication and purified via immobilized metal affinity chromatography. Purified protein was buffer exchanged into 150 mM NaCl, 10 mM HEPES, and 10% glycerol at pH 7.5 and characterized with SDS-Page.

3oc4 was also crystallized overnight by vapor drop diffusion in 1.5 to 2 M sodium formate and 0.1 M sodium acetate at pH 4.6. Crystals were washed and equilibrated in a drop of 4.2 M TMAO and 50 mM imidazole for 10 mins. Next, crystals were crosslinked in 4.2 M TMAO, 50 mM imidazole, and 100 mM EDC. After two hours in the crosslinking solution, the crystals were quenched in 50 mM borate at pH 10 for 15 mins. After crosslinking and washing, crystals retained smooth, elliptical morphology and clear to slightly yellow color.

*Gold synthesis*

$Na_3Au(S_2O_3)_2$ was synthesized using previously published methods.[3] Approximately 2 ml of 15 M NaOH was added dropwise to 3.65 ml of 0.1 M $HAuCl_4$ dissolved in $H_2O$ until a white precipitate formed at approximately pH 8.5. After stirring for 5 mins, 10.16 mL of $Na_2S_2O_3$ (5.18 g) dissolved in water was added at once and was allowed to continue stirring for 5 mins. Approximately 1.8 ml of 4 M $HNO_3$ was added

dropwise until a red color change was no longer seen after each drop addition. The reaction was filtered and washed x4 with 100 mL EtOH. The precipitate was dissolved in 20 mL $H_2O$ followed by EtOH precipitation using 80 mL of solvent. The precipitate was filtered and washed x3 with 80 mL of EtOH.

$Au_{25}(GSH)_{18}$ was synthesized using previously published methods.[4] 98.6 mg $HAuCl_4$ were dissolved in 50 mL of MeOH. 0.3062 g of reduced glutathione (GSH) were added to the solution and stirred until colorless. The contents were placed in an ice bath for 30 mins along with 12 mL of 0.2 M $NaBH_4$. The $NaBH_4$ was added rapidly to the solution under vigorous stirring. The reaction was allowed to stir for 1 hr. The contents were spun at 4000 rpm for 10 mins. The supernatant was discarded and pellets were dispersed in 2 mL of $H_2O$ followed by the addition of 200 uL of 5 M $NH_4OAc$ and 48 mL MeOH. After spinning at 4000 rpm for 10 mins the supernatant was again discarded. The previous steps were repeated x2 and the pellet was allowed to dry. The clusters were further separated using 24% Tris-Borate-EDTA (TBE) buffered polyacrylamide gel electrophoresis (PAGE) run at 125 V for 4.5 hrs.

$Au_{25}(NTA)(GSH)_{17}$ was synthesized using a common ligand exchange reaction. Briefly dried and purified $Au_{25}(GSH)_{18}$ was dissolved in $H_2O$ and five equivalents of HS-NTA was added. This reaction was allowed to shake for 7.5 minutes.[5] The products were then precipitated using MeOH and 200 µL of 5 M $NH_4OAc$. After collection using centrifugation the precipitate was dried under reduced pressure.

*Electron microscopy*

To obtain TEM images of released gold nanorods, solutions of the grown and dissolved protein crystals were spun at 14,000 rpm for 30 minutes and the supernatant was decanted. The remaining solution (approximately 10 uL) was used to suspend the rods and 4uL of this solution was mounted onto 200 mesh $Cu^{+2}$ grids with a 50 nm carbon coating (Ted Pella Inc.). TEM images were taken on a JEOL-1400 Transmission Electron Microscope at an accelerating voltage of 100 kV. A tilt series from $\pm 60^{o}$ was collected on a rod bundle in $0.5^{o}$ increments suing the JEOL-1400 TEM mentioned above.

*Embedding and ultramicrotoming*

We used a variety of methods to attempt to view the gold nanostructures within intact crystal pores. Our first attempts involved ultramicrotoming resin embedded crystal samples for observation by transmission electron microscopy (TEM). Gold grown crystals were embedded following previously published methods.[11] Briefly, a hard grade Epon resin mixture containing 50% resin monomer, 35% nadic methyl anhydride, and 15% dodecenyl succinic anhydride was lowly introduced to the crystal solution, beginning with 5% resin mixture in acetone (v/v). Over three days this was increased to 100% with shaking. Accelerator (dimethylaminemethyl phenol) was added to the resin at the 100% step. The resin mixture, with crystal embedded, was cured over two days at $60^{o}$C. The samples were cut to ~ 90 nm thick on a Riechert Ultracut E using a glass or diamond knife and imaged by TEM as described above.

*UV-Vis-NIR spectroscopy*

A Flame spectrometer (Ocean Optics) was SMA-coupled to a bare, 200 um inner diameter fiber optic cable (Ocean Optics). An identical fiber optic cable was coupled to a stabilized Tungsten/Halogen light source (ThorLabs, SLS201L). Both cables were superglued to a glass slide with a ~200 um gap between, where a crystal could be placed in a 20 uL drop of solution. The slide could be sealed with a glass coverslip and vacuum grease to prevent evaporation during the experiment. While reading, the entire setup was covered with a box to prevent spectra variations from ambient light.

A crystal was loaded with 1 mg/mL $Au_{25}$ for 30 mins, then transferred to a drop of 10 mM $HAuCl_4$ for 5 mins. The crystal was placed on the glass slide between the fiber optic cables in a 20 uL drop of 5 mM ascorbic acid. The orientation was either “axial” (large pores parallel to the fibers) or “lateral” (large pores perpendicular to the fibers). Transmission pixel intensity data was collected every three seconds for 10 minutes at a 50 ms integration time with a sliding window average of 30 in order to smooth the data.

# CHAPTER 4. ENZYME CAPTURE AND CATALYSIS IN PROTEIN CRYSTALS[‡]

## SYNOPSIS

Immobilization of enzymes offers many benefits including increased stability, activity per volume, and recyclability. Enzymes have been immobilized on natural and synthetic substrate surfaces, within hydrogel matrices, on the surface of metallic nanoparticles, and within DNA nanocages and crystals. They have been shown to have increased activity over their free counterparts, be more resistant to thermal and protease degradation, and lose only a fraction of their activity over multiple uses. In this work we show that porous protein crystals can also act as immobilization scaffolds and nanoreactors for a model enzyme pathway. The enzymes adsorb strongly to the crystals and retain activity within the crystal pores over multiple recycles. Crystals of a higher surface-to-volume ratio show lower diffusion limitations and thereby increased activity. Lastly, immobilized enzymes within the crystal pores show increased thermostability compared to free enzyme.

[‡] Kowalski, A., Johnson, L., Dierl, H., Park, S., Huber, T., and Snow, C. *Biomaterials Science.* In revision. 2018.

# INTRODUCTION

## *Enzyme research and applications*

Over 200 different enzymes are produced at the industrial scale worldwide. They are applied in industries such as food production, pulp and paper, textile, detergent, dairy production, brewing, and organic synthesis.[153] Hydrolytic enzymes are the most common industrially, including proteases, amylases, and cellulases in the detergent, dairy, textiles, and baking industries.[154] Enzymes, or biocatalysts, offer many advantages for manufacturing, including mild reaction conditions, biodegradability, high selectivity, and high activity.[155]

The development of more advanced fermentation techniques has allowed the targeted production of pure enzymes at the industrial scale. More recent developments in recombinant DNA technology, protein engineering, high-throughput screening,[156] and directed evolution have resulted in new or optimized enzymes.[154]

Improvements to industrial biocatalysis may come from the continued development of enhanced enzymes, but may also be impacted by advances in downstream processing and enzyme recycling. Efficient and cost-effective bioseparations processes will be required for product separation. Additionally, some enzymes are too costly for commercial applications and must be recovered and reused. Reduced enzyme prices, either by reuse or production improvements, may dramatically increase the number of applications found for biocatalysts.[156]

*Enzyme optimization via immobilization*

Despite their high activity and sustainability advantages, the industrial application of enzymes is hindered by a lack of long-term operating stability and difficulty of re-use. These challenges have motivated the research and development into immobilized enzymes.[155] The two main advantages of immobilized over free enzymes are ease of product separation and ease of enzyme recycle. Additionally, some immobilization schemes offer protection of the enzymes from heat or degradation, as well as enhanced turnover rate and long-term stability.[157] In most immobilization strategies, the enzyme can also be removed quickly from the reaction solution, which allows for more precise control over the length of reaction and percent conversion to products.[158] If designed correctly, enzyme immobilization technology has the potential to improve almost any enzyme property including specific activity, selectivity, stability, and cost.[159]

*Advantages and drawbacks of specific immobilization techniques*

Enzymes can be immobilized in a variety of ways: bound to a solid support, entrapped within a porous network, attached to the surface of nanoparticles, or crosslinked to each other (e.g. crosslinked enzyme aggregates and crystals).[155]

Researchers have used natural polymers, such as cellulose, starch, and collagen, to immobilize or entrap enzymes.[160] In one example, a starch gel was employed to immobilize a peroxidase enzyme to either the surface and interior of the starch matrix. The researchers found that surface support immobilization and entrapment held distinct advantages and disadvantages. When entrapped within the starch support, the enzyme retained about 50% of its free activity, compared to 63%

when only surface immobilized. However, the entrapped enzyme retained 75% of its initial activity after the seventh repeated use, while the surface immobilized enzyme was less long-term stabilized and retained 69% of activity after seven recycles. This example suggests that entrapment within a gel or matrix may inactivate or block some of the enzyme, but may still be advantageous for long-term use under harsher industrial conditions.[161]

*Nanoparticle and nanotube immobilization*

As magnetic nanoparticle technology continues to be developed, researchers are looking to nanoparticles as immobilization supports. Magnetic nanoparticles provide many advantages: biocompatibility, high surface-to-volume ratio, ease of separation by exposure to a magnetic field, and the potential for targeted protein or enzyme release.[157]

In a recent notable example, Fortes *et. al.* immobilized laccase, a common industrial enzyme, to silica-coated iron oxide ($Fe_3O_4$) nanoparticles with functionalized with amine groups. Laccase enzymes could then be glutaraldehyde-crosslinked to the surface amine groups. With magnetic separation, this group was able to recycle the enzyme-laden nanoparticles six times and retain 75% of initial activity. This is quite impressive given this number accounts for both enzymes deactivated over time, as well as entire nanoparticles lost during the recycle steps. Additionally, the nanoparticle-immobilized enzymes had higher thermal stability than free laccase, which may be relevant to industrial conditions.[162] However, abrasion within a stirred tank reactor may break the silicate coating over time and wash away the enzyme.[157]

In a related example, Asuri *et. al.* recently demonstrated the use of water-soluble carbon nanotubes as enzyme immobilization supports. Enzymes could easily be covalently attached to the oxidized walls of multi-walled carbon nanotubes. Although the immobilized enzymes retained only 50-60% of their activity in aqueous solutions when compared to a free enzyme solution, they could be reused over 100 times and retain 70% of their initial activity. Separation was simple by filtration due to the high length of the carbon nanotubes.[163]

*CLEC and CLEA immobilization*

High enzyme loading is a requisite for industrial efficiency when creating a bioreactor. Nanoparticles, with high surface-to-volume ratio, may be more desirable immobilization agents than large matrices or gels. However, even more efficient may be supportless immobilization strategies like crosslinked enzyme aggregates (CLEAs) and crosslinked enzyme crystals (CLECs).[155]

CLECs have a higher activity per unit volume than their free counterparts, as the enzyme concentration within a CLEC is much higher than a free enzyme solution. Additionally, CLECs are more stable in organic solvents and aqueous media and can easily be recycled and separated from products through filtration or gentle centrifugation.[164] CLECs, in development since the 1990s, have more recently been overtaken by CLEAs. CLECs, despite their advantages, require a high purity starting material, which an lead to higher prices.[165] CLEAs, which are physical aggregates of a crude enzyme preparation often crosslinked with glutaraldehyde, eliminate some costs associated with crystal-quality purification schemes.[165]

In one recent example, Matijosyte *et. al.* created a laccase CLEA which showed significantly higher activity than corresponding free laccase enzyme. Again the CLEA could be recycled four times without significant activity loss.[165] CLEAs have also been shown to have less sensitivity to high pH, high temperatures, and organic solvents than free enzymes.[166] More recently, the concept of CLEA immobilization has been combined with the separation advantages of magnetic nanoparticles. Bhattacharya *et. al.* developed a CLEA consisting of lignocellulolytic enzymes crosslinked with magnetite and calcium magnetite. In the presence of $Fe^{+2}$ and $Fe^{+3}$ ions, CLEA activity and stability were significantly higher than either free enzyme or CLEA in the absence of magnetite. This suggests ions contribute to both enzyme activity and stability at high temperatures. These CLEAs were also successfully recycled using a magnetic field to separate the CLEA from the product and excess substrate.[167]

*Guest immobilization to biological supports*

In thinking about the environmental benefits of green chemistry, biocompatibility, and biodegradability, researchers are not only interested in using protein enzymes to replace less sustainable chemical catalysts. There is also a push to immobilize these enzymes on biomolecules which are themselves cheap, efficient, and biodegradable. This work began in the 2000s with the increased understanding of enzyme organization and compartmentalization in nature. Researchers began to determine that most reactions within cells occur by enzyme complexes that are membrane-bound as opposed to free-floating. In this way, metabolic pathways were made more efficient by placing related enzymes in proximity to each other. This proximity could allow for

increased specificity, regulation, and efficiency through intermediate channeling.[168] Cellular evolution of organized enzyme systems also can prevent off-pathway reactions, limit toxic intermediates, and increase enzyme turnover.[169]

In attempting to mimic natural compartmentalization and immobilization, researchers have used a variety of biological tools. Enzymes have been tethered to synthetic, eukaryotic protein scaffolds which allowed control over metabolic flux.[170] RuBisCO, an important carbon fixation enzyme, was encapsulated within a carboxysome shell for increased pathway flux.[171] DNA has been used to control the assembly of multiple enzymes,[172] and the resulting systems have shown increased enzymatic activity when compared to unscaffolded enzymes.[173] Lipids[174] and membrane-bound organelles[175] have also shown promise for the organization and compartmentalization of enzymes.

In one example, Fu *et. al.* tethered glucose oxidase and horseradish peroxidase enzymes at specific locations on a DNA nanostructure. They were able to precisely control the location of the two enzymes with respect to each other and study the effect of distance on the catalytic efficiency of the two-enzyme pathway. They found that when closely spaced, the two enzymes had significantly increased activity, which dropped correspondingly as the distance between them as increased to 20 nm.[176]

Researchers have since further optimized this general design strategy by additionally linking a cofactor onto a “swinging arm” between the two enzymes of interest. Fu *et. al.* now used glucose dehydrogenase and malate dehydrogenase to demonstrate that activity could be increased when NAD+ was tethered to the end of a

single DNA strand between the two immobilized enzyme. The tethered NAD+ increased the efficiency of hydride transfer.[177]

In another example, a full DNA crystal was used to encapsulate an RNase A enzyme. The enzyme was active within the crystal, but the expected substrate and product diffusion limitations within a large crystal led to non-Michaelis-Menten activity profiles.[178] More recently, Zhao *et. al.* demonstrated that it was possible to increase catalytic activity of an enzyme pathway when immobilized within a DNA nanocage instead of a DNA crystal. In this work, the researchers attached a single glucose oxidase and horseradish peroxidase within a design DNA cage. The immobilized enzymes showed increased activity when compared to their free counterparts, as well as increase stability against destruction by proteases. Surprisingly, the group determined that the activity increase came mostly from the optimized electrostatic environment of the DNA cage itself rather than the proximity it allowed between the two enzymes in the pathway.[179]

Virus capsids, protein cages, and protein crystals have also been used to entrap or immobilize enzymes. In one of the first examples, researchers encapsulated nanoceria particles ($CeO_2$) within ferritin cages to act as superoxide dismutase mimics for reactive oxygen species scavenging. By encapsulating the nanoparticle within a protein cage, the group was able to increase the biocompatibility of the enzyme mimic and increase its overall oxygen scavenging activity.[180]

More recently, Liljestrom *et. al.* developed the electrostatic self-assembly of a biomacromolecular superlattice consisting of cowpea mosaic virus and avidin protein. Through specific avidin-biotin interactions, they demonstrated that this protein crystal

could be pre- or -post modified with enzymes such as horseradish peroxidase, which remained active upon immobilization.[27]

Similarly, Abe *et. al.* recently engineered a polyhedral crystalline protein assembly which can serve as a long-term enzyme storage container. Within the container, the enzymes remained active even in typically denaturing pH ranges. At the optimal pH for enzyme activity, the polyhedral crystal dissolved and released the encapsulated enzymes.[181]

*Impacts of presented work*

In this work, we show the first example of a large-pore protein crystal as an immobilization scaffold for a multi-enzyme pathway. CJ, the same protein crystal that in previous chapters was used to reversibly trap gold nanoparticles and synthesize gold nanorods, is now used to capture glucose oxidase and horseradish peroxidase enzymes within the pores. These enzymes adsorb strongly to the pores, allowing for high loading capacity beyond concentrations in solution. The enzymes can either be electrostatically bound via shared metal affinity or physically entrapped by creating a protein shell around the crystal. Although enzyme activity is lower within the crystal than in solution, we show that this may stem from diffusion limitations rather than enzyme inhibition due to steric constraints or active site blocking. In smaller crystals with a higher surface-to-volume ratio, activity is increased. Additionally, these enzymes retain the typical benefits of immobilization, including recyclability and increase thermal stability.

The use of protein crystals as microreactors for enzymatic pathways and scaffolding for enzyme immobilization has several impacts. The pores of these crystals are larger than most metal-organic frameworks or DNA crystals, which may decrease diffusion limitations in the future and allow for the entrapment of even large enzyme guests. Additionally, the designability of proteins and protein crystals is ever increasing. It may be possible to design crystals containing solvent channels of specific, desired physical and chemical qualities in order to optimize enzyme immobilization and activity.

## RESULTS

### *Quantification of enzyme loading into protein crystals*

Protein CJ was expressed, purified by metal affinity chromatography, and crystallized in ammonium sulfate as in previous work. The crystals were crosslinked by direct addition of 1% glyoxal for 2 hrs. The reaction was quenched in 30 mM hydroxylamine and 100 mM dimethylamine borane complex at pH 5.0.

HisProbe$^{TM}$-Horseradish Peroxidase (hHRP, Sigma Aldrich) was fluorescently tagged with NHS-Fluorescein (Sigma Aldrich) for ease of imaging. The HisProbe$^{TM}$ is a proprietary tridentate chelator with a mechanism similar to that of iminodiacetic acid (IDA) for binding divalent metals. HisProbe$^{TM}$, in combination with the 6xHisTag on the C-teminus of the CJ protein, allow for shared metal affinity between the peroxidase and the crystal and should encourage enzyme loading into the crystal as well as retain the enzyme long-term.

A standard curve of protein concentration was created using a Bradford assay and a standard curve of fluorescence intensity as a function of protein concentration was created using a fluorescence plate reader (FLUOStar Omega, BMG Labtech) (Fig. 4.1).

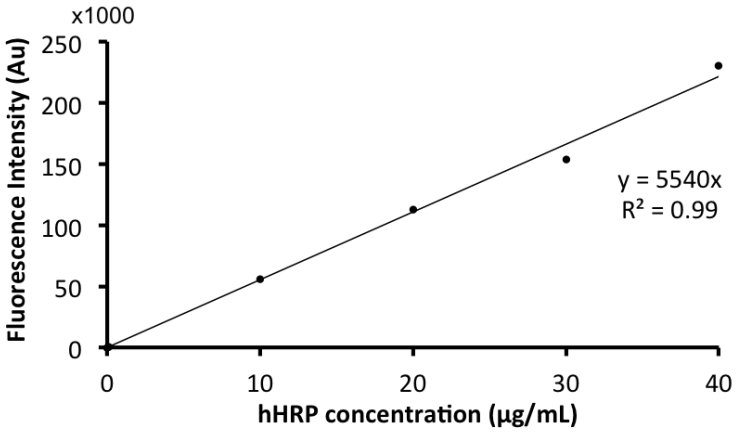


Figure 4.1 hHRP standard curves

Fluoresence intensity standard curve as measured at 461 nm wavelength excitation on a FluoSTAR Omega (BMG Labtech) plate reader.

We first monitored hHRP loading into the crystal via a Nikon TI spinning-disk confocal microscope. A crosslinked CJ crystal, previously loaded with 10 mM $NiSO_4$, was immobilized to a glass slide using a drop of UV-curable glue (Bondic) (Fig. 4.2E). Typically crystals were glued along their lateral side, leaving the 13 nm axial pores accessible on both top and bottom of the crystal. A drop of fluorescently tagged hHRP at 30 ug/mL was pipetted onto the crystal and the system was sealed with a glass cover slip and vacuum grease. At t=0, the crystal was much darker than the surrounding solution (Fig. 4.2A) when imaged under 488 nm wavelength light. Over, time the crystal adsorbed hHRP and became brighter than the surrounding solution (Fig. 4.2D). All

images were taken through a central plane of the crystal. The white dotted line in Figure 4.2A depicts the location where the pixel intensity of the image was calculated using ImageJ and used to create the graph in Figure 4.2F. After 16 hrs, the interior of the crystal is approximately twice as bright as the surrounding solution (line D in Fig. 4.2F). This experiment qualitatively confirmed that hHRP adsorbed strongly throughout the entire thickness of a crosslinked CJ crystal in the presence of Ni(II).

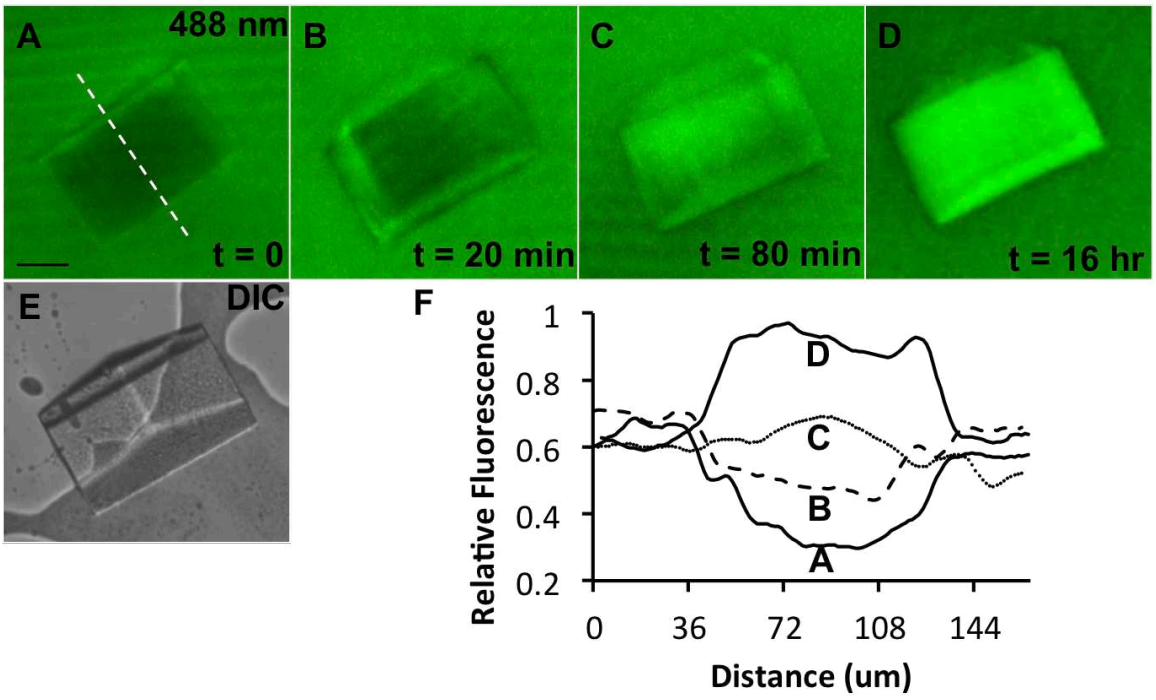


Figure 4.2 Absorbance of hHRP into a CJ crystal

(A-D) Over 16 hours, hHRP at 30 ug/mL adsorbs into the pores of a CJ crystal. Fluorescence was imaged on a spinning disk confocal microscope at 488 nm wavelength excitation. (F) A differential interference contrast (DIC) microscopy image of the CJ crystal on the glass slide. (E) Using ImageJ, pixel intensity across the center of the crystal, as shown by the white dotted line in (A), was determined at the four loading timepoints (A-D). Scale bar is 50 um.

A fluorescence plate reader was used to quantify hHRP loading into CJ crystals over time (Fig. 4.3). Three or more crystals, of known volume, were placed in a 150 µL

well of ~10 μg/mL hHRP in Buffer A. Aliquots of 75 μL of the enzyme solution were sampled at various time points to monitor the decrease in enzyme concentration in the solution as enzyme was adsorbed by the crystals. After measurement, the 75 μL aliquot was returned to its' original well, and pipetted to mix with the remaining 75 μL of solution and the crystals. A black-walled 96-well plate (Costar) was used for the fluorescence plate reader measurements. Crystal volumes were measured using Motic Imaging software to calculate the adsorbed enzyme concentration for each crystal.

Although the equilibrium enzyme concentration is expected to be similar for any size crystal, the rate of loading depends on the crystal surface area, thickness, and overall volume. Sample 2, which contained the largest total crystal volume, loaded guest enzymes more slowly per unit volume than the other two samples but had a similar equilibrium hHRP loading concentration. Our previous work has shown that the aspect ratio and size of CJ crystals can be tuned by adjusting crystal growth conditions such as pH and salt concentration, providing a potential opportunity to create custom scaffolds with varying loading (or unloading) rates.

Equilibrium conditions were achieved after 20-24 hours, and enzymes loaded to a final concentration of ~0.7 mM. The original enzyme concentration in solution was approximately 0.23 μm; thus the enzyme adsorbed well beyond the concentration expected by pure diffusion. If hHRP could bind to every HisTag presented in the crystal pores, the loading concentration would be expected to reach approximately 14 mM. Close packing within the crystal pores prevents every HisTag from being able to bind with large guest molecules.

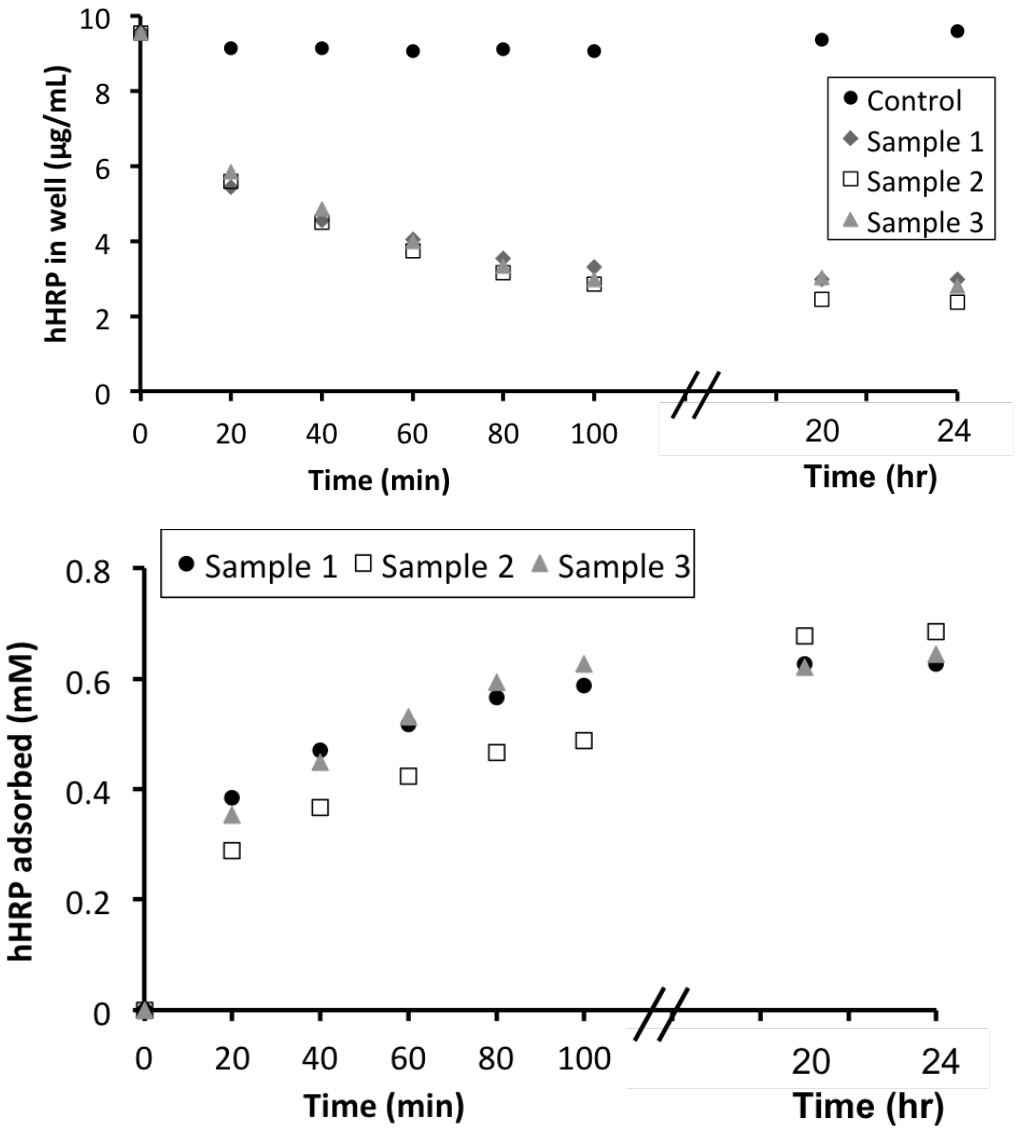


Figure 4.3 Quantification of hHRP loading

(Top) Three samples of three crystals each load 10 ug/mL hHRP over time. At various timepoints, 75 uL of the solution was transferred from the loading well to the fluorescence plate reader in order to determine the concentration of hHRP remaining in the well at that time. This in turn allowed us to calculate the concentration of hHRP that had adsorbed into crystals of known volume (bottom).

*In crystallo catalysis and recycling*

After assessing single enzyme loading and retention within CJ crystals, we demonstrated that it was possible to simultaneously load a second guest, fluorescently-tagged glucose oxidase (GOx), and that both enzymes were catalytically active within the crystal pores (Fig. 4.4). In the two-step GOx/hHRP pathway, GOx reacted with D-glucose and oxygen to form D-gluconolactone and hydrogen peroxide. hHRP reacted with AmplexRed and hydrogen peroxide to form resorufin and oxygen. Both enzymes (hHRP and GOx), as well as both substrates (glucose and AmplexRed) needed to be present for the resorufin product to be formed. Resorufin fluoresces red under 561 nm wavelength light.

To image product formation and prevent crystal movement throughout the experiment, crystals were again immobilized to a glass slide with UV-curable glue. However, the same enzyme pathway was tested on a crystal in free solution to confirm that the presence of the glue did not alter the reaction. Crystals were first loaded with hHRP by soaking for a minimum of one hour in Buffer A plus 10 mM nickel sulfate and then soaking for at least one hour in 0.5 mg/mL hHRP in Buffer A. The crystal was subsequently loaded with 1.5 mg/mL glucose oxidase (GOx) for 2 hours. The GOx, lacking a metal-chelating group, was physically trapped within the crystal pores by briefly exposing the crystal to a solution of 1% glyoxal and 1 mg/mL bovine serum albumin (BSA). Together, the glyoxal crosslinker and the BSA should form a gelatinous shell surrounding the crystal.

In order to observe product formation from the GOx/hHRP pathway, the storage solution (Buffer A) was removed and 20 µL of substrate solution (Buffer A supplemented

with 10 μM AmplexRed and 100 μM glucose) was pipetted atop the crystal on the glass slide. Confocal excitation at 561 nm distinctly showed fluorescent product formation throughout the crystal when both enzymes and substrates were present. In less than 30 seconds, resorufin began diffusing into the surrounding bulk solution.

Figure 4.4 shows the results of a single crystal trial for the experiment and four corresponding negative controls. Product formation only occurs in the top row of the figure, when both enzymes and both substrates are present. In the second row, GOx, tagged with CF405S, which fluoresces under 405 nm wavelength light, is absent from the crystal. In the third row, NHS-fluorescein tagged hHRP is absent. In the bottom two rows, both enzymes are present, but the substrate solution lacks either AmplexRed (fourth row) or glucose (bottom row).

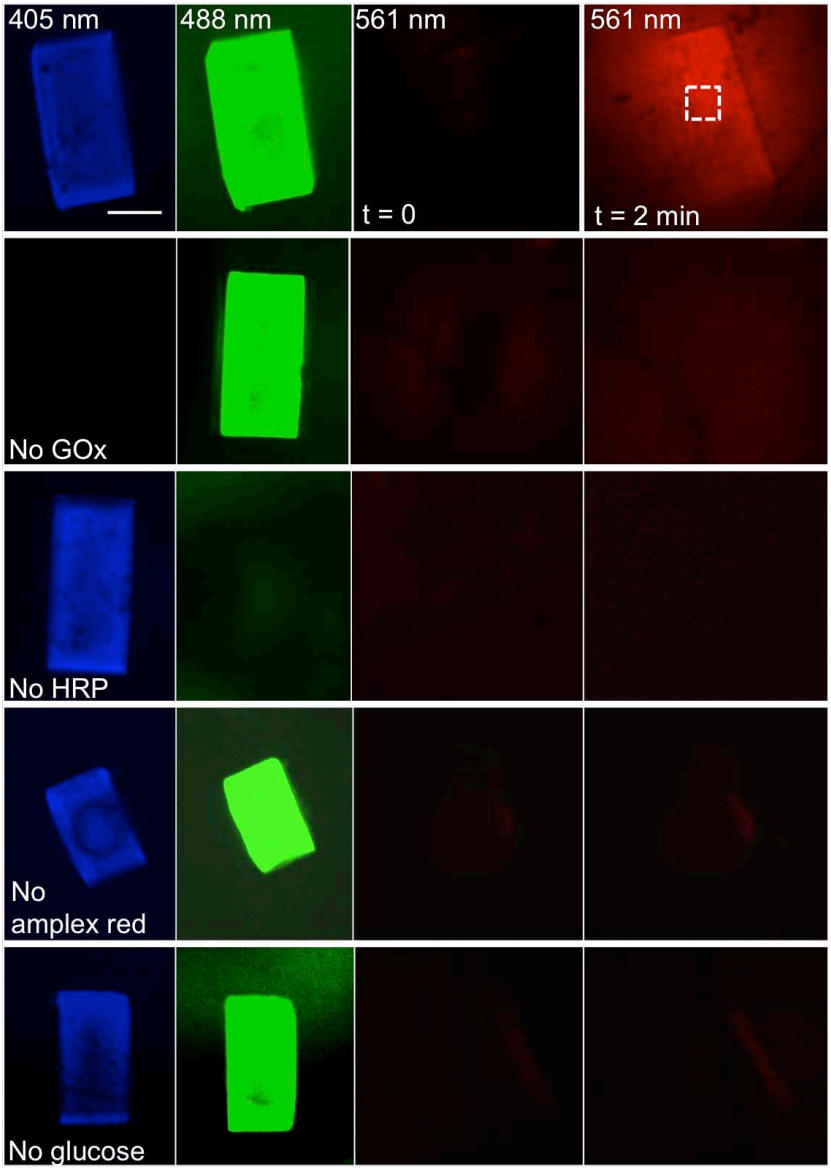


Figure 4.4 GOx/hHRP pathway.

A CJ crystal is loaded with 1.5 mg/mL glucose oxidase (GOx) and 0.5 mg/mL HisProbe™ horseradish peroxidase (hHRP) (top row), only hHRP (second row), or only GOx (third row).The crystal is exposed to 100 uM glucose and 10 uM AmplexRed (top three rows), only glucose (fourth row), or only AmplexRed (bottom row). GOx, tagged with CF™405S, fluoresces blue under 405 nm wavelength light (left column). hHRP, tagged with fluorescein, fluorescence green under 488 nm light (second column from left). The formation of resorufin, which is dependent on the presence of both enzymes and both substrates, causes red fluorescence under 561 nm wavelength light (right two columns). All fluorescence images were taken using a spinning disk confocal microscope. Scale bar is 100 μm.

The experiment in Figure 4.4 was repeated two additional times, and the results of the three trials are presented in Figure 4.5. Figure 4.5 shows the increasing pixel intensity as resorufin product was formed in assays with three different crystals. Pixel intensity was determined in ImageJ by averaging over a 25x25 μm box within the image, as demonstrated in the top right panel of Figure 4.4.

Pixel intensity in Figure 4.5 was reported raw (top) and corrected for crystal volume (bottom), as a larger crystal volume resulted in a larger number of active enzymes and thus a higher overall pixel intensity. Triplicate negative controls had negligible pixel intensity (Fig. 4.7) and confirmed that product formation only occurred in the presence of a complete GOx/HRP pathway. In the absence of GOx, HRP, AmplexRed, or glucose, minimal to no resorufin production was observed. Over two minutes, the average pixel intensity of crystals loaded with both enzymes was greater than 100 times higher than that of any negative control.

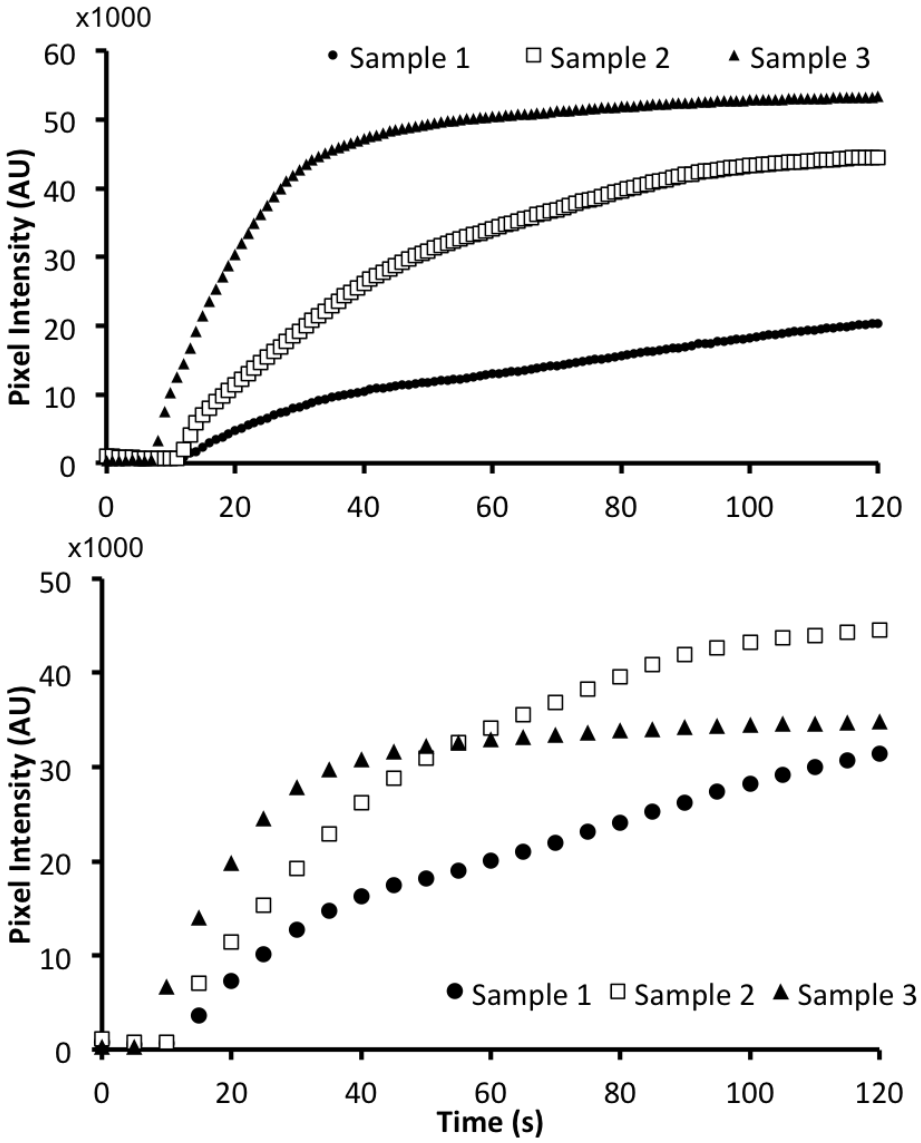


Figure 4.5 Resorufin production

Pixel intensity corresponding to resorufin production imaged under 561 nm light, as measured by averaging a 25x25 μm box within each crystal (demonstrated in the top row of Fig. 4). Pixel intensity increases in the presence of both enzymes and both substrates for three samples. Correcting the raw pixel intensity (top) for crystal volume (bottom) removed some variability in product formation over time, as larger crystals would contain more enzyme and produce more resorufin. Average pixel intensity was calculated using ImageJ.

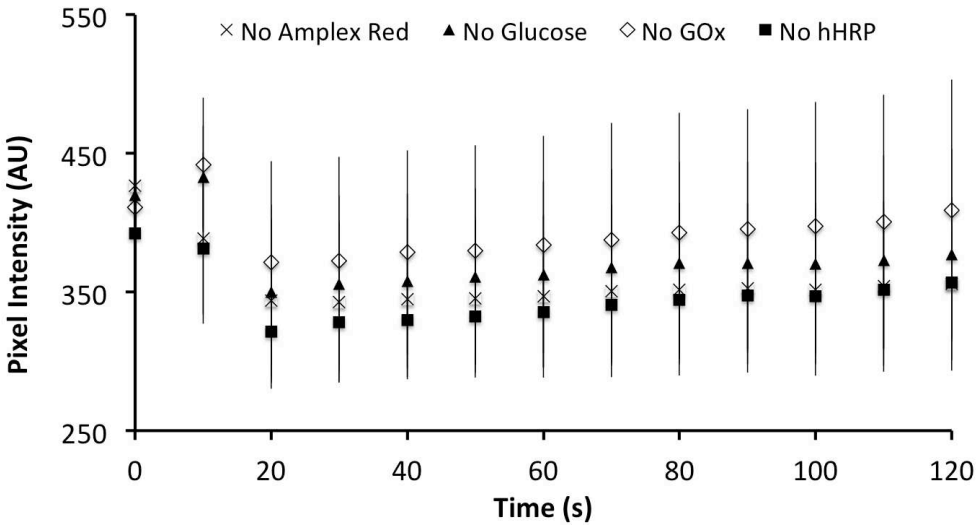


Figure 4.6 GOx/hHRP pathway negative controls

In the absence of horseradish peroxidase (hHRP), glucose oxidase (GOx), glucose, or AmplexRed, the pixel intensity of a 25x25 μm box (as displayed in the top row of Fig. 4.4) is much lower than for any positive control. Error bars show the standard deviation of three samples.

*Comparison of immobilized versus free enzyme activity*

Immobilized enzymes often exhibit reduced activity compared to their free counterparts, as a result of transport limitations, or the loss or inhibition of active enzymes. To investigate the effect of immobilization within CJ crystals on the activity of hHRP, hHRP was entrapped within several CJ crystals of varying size (Figs. 4.8, 4.9).

A standard curve of resorufin product formation was calculated using a fluorescence plate reader (FLUOstar Omega, BMG Labtech) in order to relate fluorescence intensity to resorufin concentration produced during the reaction of hHRP with AmplexRed and $H_2O_2$ (Fig. 4.7). In all plate reader experiments, a black-walled 96-well plate (Costar) was used, and the plate was shaken for one second between each fluorescence measurement to encourage uniform product distribution in the drop.

Additionally, fluorescence readings were taken from above the well in order to minimize the effect of the crystal, which sat at the bottom of the well.

Figure 4.8 shows resorufin formation over time from the same concentration of free hHRP in solution and hHRP immobilized within two crystal samples. Sample "Immobilized Enzyme 1" consisted of one crystal of known dimensions. "Immobilized Enzyme 2" consisted of two crystals of the same height and total volume (within 2%) as "Immobilized Enzyme 1," such that when loaded with hHRP for equal durations (30 mins), both samples should contain the same total amount of enzyme (0.38 mM or 0.09÷0.0019 μg, as calculated from Fig. 4.3 and the known crystal volumes).

Figure 4.10 helps to illustrate how the crystals were chosen for this experiment. Immobilized Enzyme 1 consisted of one large crystal of height, h, and side length, s. Immobilized Enzyme two consisted of two smaller crystals each of height, h, and of total volume equal to that of Immobilized Enzyme 1. Together, the surface area of the two crystals in Immobilized Enzyme 2 is significantly larger than that of Immobilized Enzyme 1.

Figure 4.8 shows that despite containing the same quantity of enzyme, the rate of product formation for the two immobilized enzyme samples was different. We hypothesized that differences in substrate diffusion contributed to this result. Immobilized Enzyme 2, despite containing the same amount of enzyme as Immobilized Enzyme 1, had a 16.2% larger surface area and thus a larger surface-to-volume ratio than sample 1 (Fig. 4.11). More hHRP enzyme was accessible to the substrate during the reaction, which allowed Immobilized Enzyme 2 to produce resorufin at a higher rate than Immobilized Enzyme 1 when both were exposed to the same substrate

concentrations, 100 μM AmplexRed and 100 μM $H_2O_2$. Both samples of immobilized enzyme showed lower rates of product formation than the same concentration of free enzyme in solution.

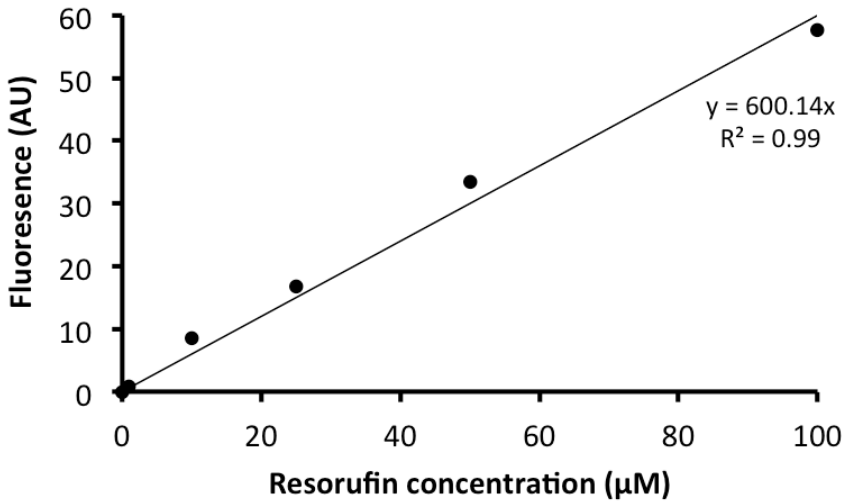


Figure 4.7 Fluorescence intensity standard curve for resorufin in Buffer A.

Resorufin is the fluorescent product formed through the oxidation of AmplexRed by hHRP. Fluorescence measurements were collected on a FLUORstar Omega fluorescence plate reader at 561 nm wavelength light.

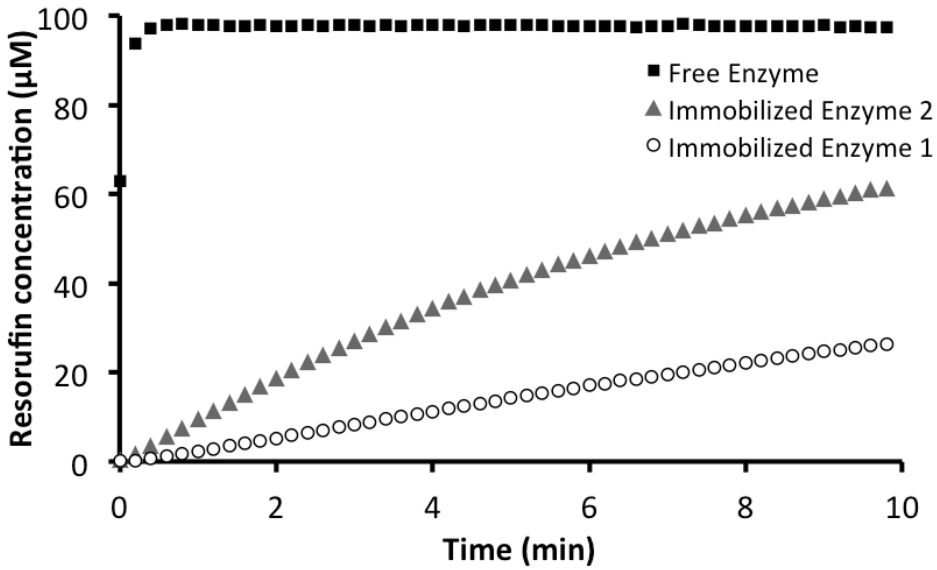


Figure 4.8 Diffusion limitations alter the activity of the immobilized enzyme

Each sample consisted of 0.38 mM hHRP either free in 100 μL of Buffer A or immobilized via Ni(II) affinity within a crystal sample, incubated in 100 μL of Buffer A. The height and volume of Immobilized Enzyme 1 and 2 were the same, but the surface area of Immobilized Enzyme 2 was 16.2% larger. Each sample was reacted with 100 μM AmplexRed and 100 μM $H_2O_2$.

To help confirm the reliability of this result, a similar experiment was performed with two different enzyme crystal samples (Fig. 4.9). In this case, each sample contained 0.5 mM hHRP, and the surface area of Immobilized Enzyme 2 was 16.8% larger than Immobilized Enzyme 1, despite the crystal volumes in the two samples being within 3% of each other. A similar trend was observed in both experiments.

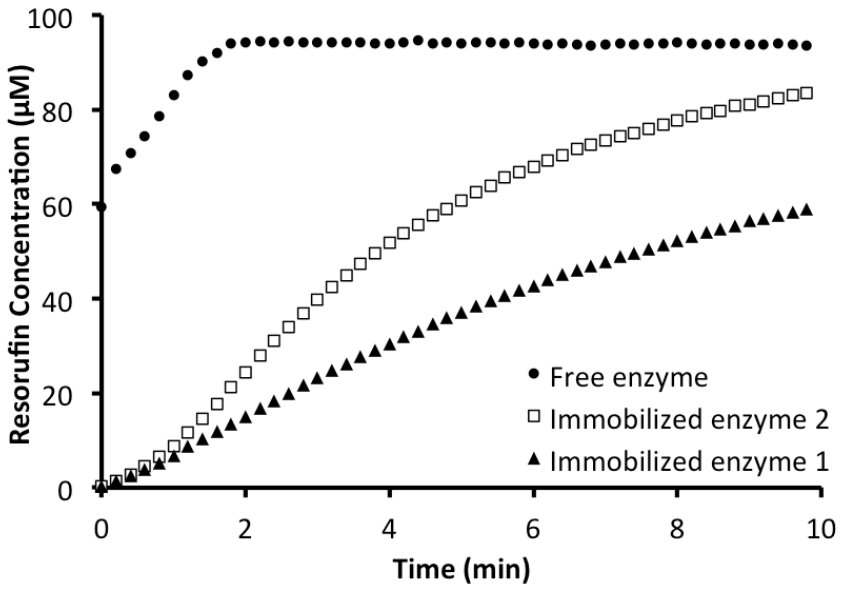


Figure 4.9 Diffusion limitations alter the activity of the immobilized enzyme

A similar experiment to Figure 4.7. Each sample consisted of 0.5 mM hHRP either free in 100 μL of Buffer A or immobilized via Ni(II) affinity within a crystal sample, incubated in 100 μL of Buffer A. The height and volume of Immobilized Enzyme 1 and 2 were the same, but the surface area of Immobilized Enzyme 2 was 16.8% larger. Each sample was reacted with 100 μM AmplexRed and 100 μM $H_2O_2$.

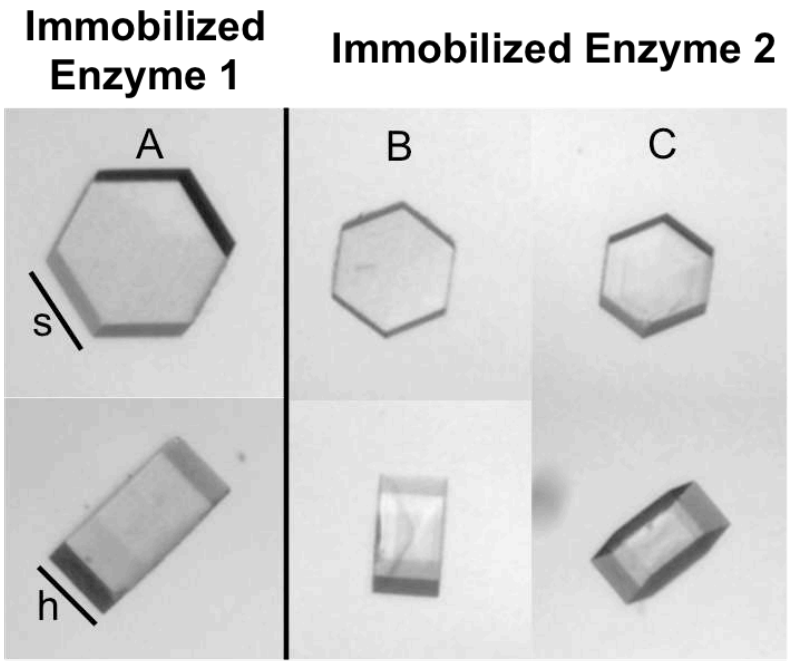


$$\text{volume (V) of hexagonal prism} = \frac{3\sqrt{3}}{2}s^2h$$

$$\text{surface area (SA) of hexagonal prism} = 6sh + 3\sqrt{3}s^2$$

$$h_A = h_B = h_C$$
$$V_A = V_B + V_C$$
$$SA_A > SA_B + SA_C$$

Figure 4.10 Surface-to-volume ratio schematic

A schematic showing how samples were chosen for the experiments described in Figure 6 and Figure S6. The height of all three crystals in sample 1 and 2 were the same, and the volume of the two crystals in sample 2 was equal to that of the one crystal in sample 1. This allowed the same amount of enzyme to be loaded into both samples, but the surface area of sample 2 to be higher than that of sample 1.

**A**

| | Immobilized Enzyme 1 | Immobilized Enzyme 2 | |
|---|---|---|---|
| s (um) | 107.7 | 93.3 | 56.3 |
| h (um) | 94.0 | 95.0 | 76.0 |
| V($um^3$) | 2832768.9 | 2148926.8 | 625867.3 |
| Total V ($um^3$) | 2832768.9 | 2774794.2 | |
| % Difference in V | **2.1** | | |
| SA ($um^2$) | 121014.5 | 98426.6 | 42143.0 |
| Total SA ($um^2$) | 121014.5 | 140569.6 | |
| % Difference in SA | **16.2** | | |

**B**

| | Immobilized Enzyme 1 | Immobilized Enzyme 2 | |
|---|---|---|---|
| s (um) | 95.9 | 64.2 | 69.1 |
| h (um) | 74.6 | 71.2 | 77.9 |
| V($um^3$) | 1782493.4 | 762433.4 | 966374.4 |
| Total V ($um^3$) | 1782493.4 | 1728807.9 | |
| % Difference in V | **3.1** | | |
| SA ($um^2$) | 90712.9 | 48842.9 | 57108.0 |
| Total SA ($um^2$) | 90712.9 | 105950.9 | |
| % Difference in SA | **16.8** | | |

Figure 4.11 Crystal sizes used in Figures 4.7 and 4.8

(A) Crystals used in Figure 4.7 (B) Crystals used in Figure 4.8. The size of the immobilized crystals is within 2-3% by volume, but in both experiments, Immobilized Enzyme 2 is ~16% larger than Immobilized Enzyme 2 by surface area.

As we saw that crystal surface-to-volume ratio affects the rate of product formation, it would be improbable to determine the Michaelis-Menten parameters for hHRP immobilized within any arbitrarily sized CJ crystal. In order to accurately determine the kinetic parameters for immobilized hHRP, the enzyme was immobilized within micrometer and sub-micrometer wide crystals (Fig. 4.12). These 'microcrystals,' are much smaller than the average CJ crystals used for imaging, which are normally

hundreds of microns across. Thus, a much higher fraction of the hHRP enzyme immobilized within these microcrystals would be accessible to solvent, and transport limitations could be minimized. Kinetic differences here between free and microcrystal-immobilized enzyme could instead be attributed to steric hindrance or active site inhibition of the immobilized enzyme. In fact, Quiocho and Richards proposed in 1966 that enzyme crystal transport limitations could be removed by using enzyme crystals less than 5 microns across.[182] In a similar study, Doscher and Richards theorized that in larger crystals, activity was confined to a thin layer approximately 1 - 6 μm thick on the surface.[183] Therefore, by using crystals less than 5 μm in diameter, we hope to calculate a generic $k_{cat}$ for hHRP immobilized in CJ crystals, without taking into account an effective hHRP concentration near the crystal surface due to transport limitations. In this way, the immobilized enzyme $k_{cat}$ can directly be compared to the free enzyme $k_{cat}$.

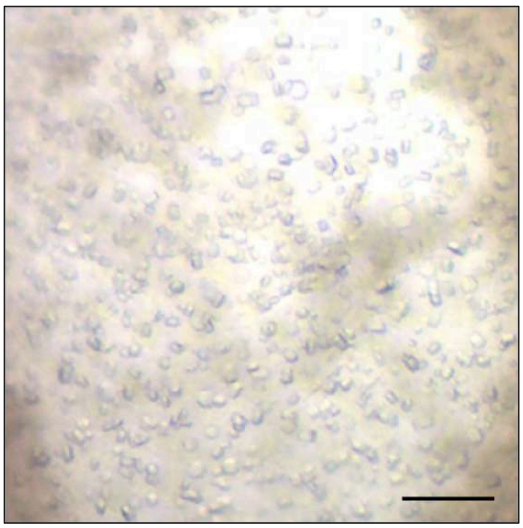

Figure 4.12 CJ microcrystals

Brightfield transmission optical microscope image of a growth well of CJ microcrystals. Crystals can be grown to less than 1 μm in diameter using high salt conditions. Scale bar is 100 μm.

CJ microcrystal handling is slightly different than for typical CJ crystals. The microcrystals are crosslinked and loaded with enzyme in batch conditions. Rather than looping each crystal individually, the sample of hundreds of microcrystals is centrifuged within a microcentrifuge tube in order to remove a solution and add a new solution to the crystals. In order to quantify hHRP loading, Ni(II)-laden microcrystals are loaded with a known volume and concentration of hHRP. After 1 hr, the sample is spun down and the concentration of hHRP remaining in solution is determined via a fluorescence plate reader. Next, the concentration that has loaded into the microcrystals can be calculated, as well as the volume of buffer in which the microcrystals should be suspended in order to reach a desired final concentration of hHRP.

Michaelis-Menten kinetic parameters $K_{cat}$ and $K_m$ were determined for 0.1 nM hHRP samples in Buffer A and immobilized in microcrystals at substrate concentrations ranging from 0.1 - 100 μM (Figs. 4.13-4.17). Figure 4.13 shows resorufin product formation over time for 0.1 mM hHRP in Buffer A at nine substrate concentrations from 0.1 μM to 500 μM $H_2O_2$. AmplexRed was held constant for all the reactions. As substrate concentration increases, product formation increases until a saturating substrate concentration is reached. Beyond the saturating substrate concentration, the enzyme activity is the limiting factor and the product formation will not increase at higher substrate concentrations.

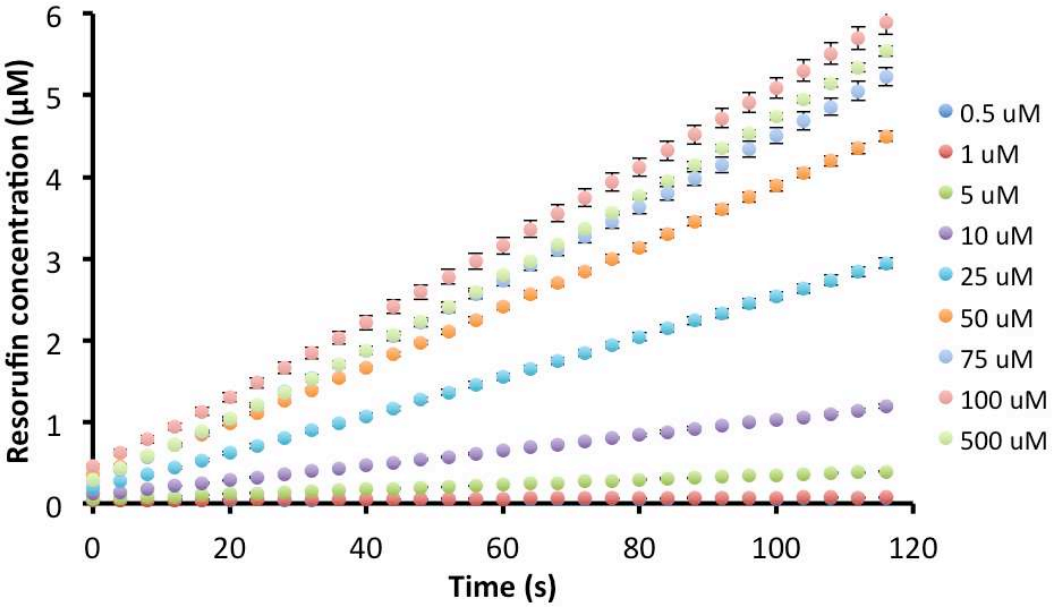

Figure 4.13 Raw activity for free hHRP

Raw activity for free hHRP in Buffer A (0.1 nM) with $H_2O_2$ varied from 0.1 - 500 uM and AmplexRed at 100 uM, monitoring fluorescence at 561 nm. Error bars were calculated from the standard deviation of three replicates.

The slope of each line in Figure 4.13 corresponds to initial rate of product formation on the y-axis of Figure 4.14. The Michaelis-Menten plot (Fig. 4.14) displayes the rate of resorufin production as a function of substrate concentration for free hHRP in solution. Through hyperbolic regression, Michaelis-Menten kinetic parameters can be calculated, where:

$$v_0 = \frac{V_{\max}[S]}{K_M + [S]}$$

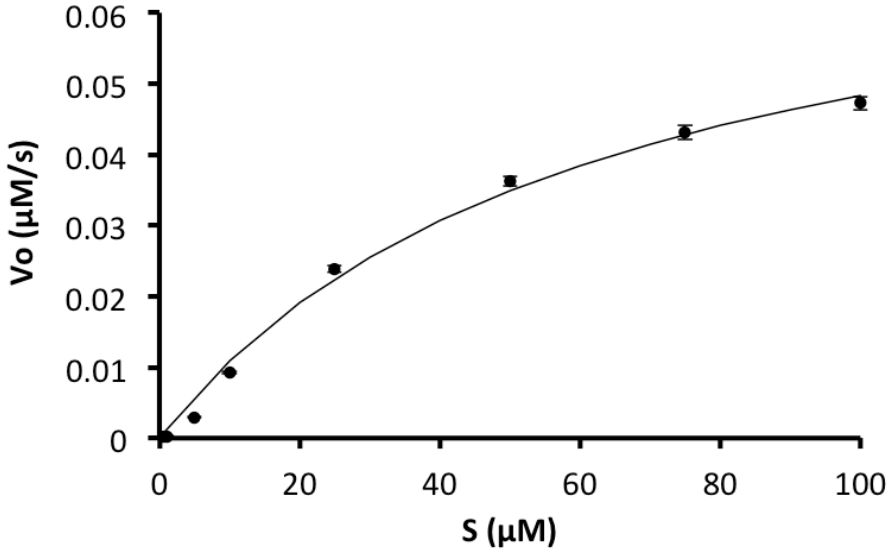


Figure 4.14 Free enzyme Michaelis-Menten kinetics

Michaelis-Menten plot of the initial rate of resorufin formation as a function of $H_2O_2$ concentration for free hHRP enzyme in solution. Rates calculated from the slope of each line in Figure 4.13. Error bars are calculated from the standard deviation of triplicate samples.

The same experiment was performed with hHRP immobilized in microcrystals at 0.1 nM in Buffer A (Figure 4.15, 4.16). Microcrystal-immobilized hHRP followed Michaelis-Menten kinetics, which is not always the case with immobilized enzymes due to transport limitations and active site inhibition.[178] This result supports our hypothesis that the use of sub-micron sized crystals would limit diffusion restrictions on enzyme activity.

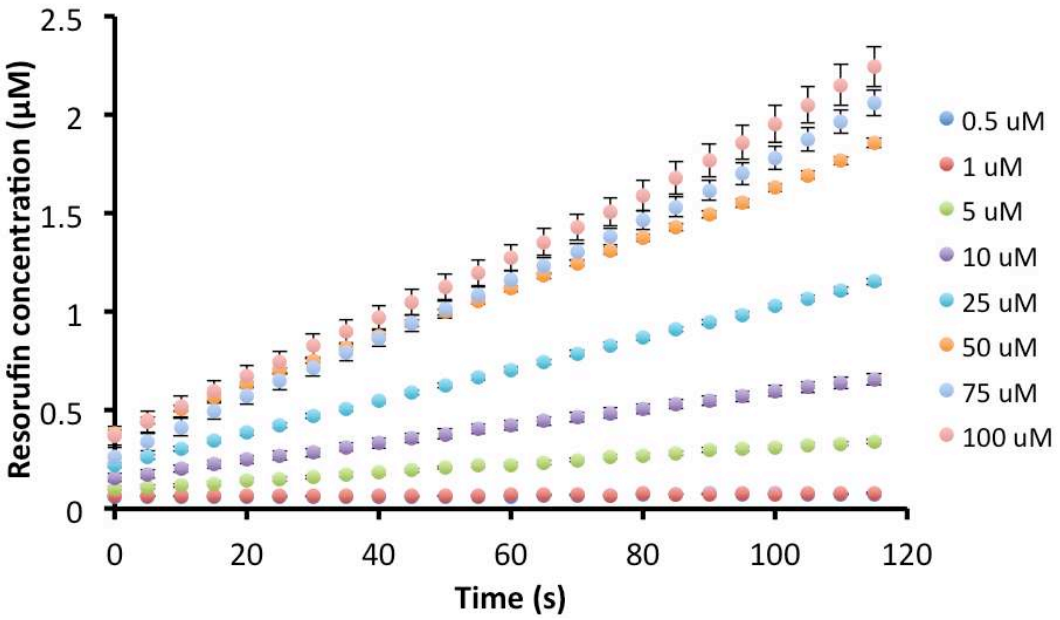


Figure 4.15 Raw activity for microcrystal-immobilized hHRP

Raw activity for microcrystal-immobilized hHRP in Buffer A (0.1 nM) with $H_2O_2$ varied from 0.1 - 100 uM and AmplexRed at 100 uM, monitoring fluorescence at 561 nm. Error bars were calculated from the standard deviation of three replicates.

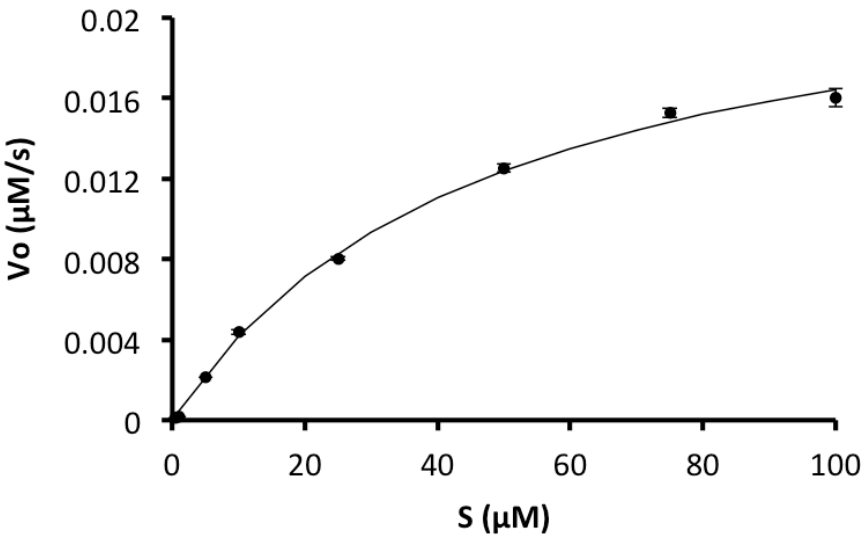


Figure 4.16 Immobilized enzyme Michaelis-Menten kinetics

Michaelis-Menten plot of the initial rate of resorufin formation as a function of $H_2O_2$ concentration for microcrystal-immobilized hHRP. Rates calculated from the slope of each line in Figure 4.15. Error bars are calculated from the standard deviation of triplicate samples.

Figure 4.17 displays the Michaelis-Menten parameters for free hHRP and microcrystal-immobilized hHRP. The turnover number, $k_{cat}$, is approximately 3 times higher for free enzyme than immobilized enzyme. It's possible the immobilized enzymes have a lower turnover number due to noncompetitive inhibition from binding to the crystal pore, a high local enzyme concentration leading to blocked active sites, or product inhibition, as diffusion of the product within the pore will be slower than in solution.

| | $K_m$ (uM) | $K_{cat}$ (1/s) |
|---|---|---|
| **Microcrystal-immobilized enzyme** | 48.5 ± 7 | 245 ± 30 |
| **Free enzyme** | 62.3 ± 7 | 784 ± 67 |

Figure 4.17 Free vs. immobilized enzyme kinetic parameters

Average and standard deviation of Michaelis-Menten kinetic parameters for 0.1 nM samples of free hHRP in Buffer A and Ni(II)-immobilized hHRP within microcrystals. Data was averaged from triplicate samples.

*Immobilized enzyme recycle*

Recycle or reuse is a major industrial benefit of enzyme immobilization. In order to test a CJ crystal's capacity for long-term enzyme entrapment and retention of enzyme activity within the crystal, sample 3 from Figure 4.5 was reused in multiple cycles (Fig. 4.18). After the initial experiment, the crystal was washed in a large volume of Buffer A for 48 hours to allow for diffusion of residual resorufin product from the crystal pores. The crystal was then immobilized again using UV-curable glue and exposed to 10 μM AmplexRed and 100 μM glucose (cycle 2). After cycles 2 and 3, the crystal was removed from the UV-glue, washed for 30 minutes to remove residual resorufin, and then re-glued to a glass slide. After cycle 4, the crystal was incubated in a large reservoir of Buffer A at room temperature for 16 days prior to use in cycle 5

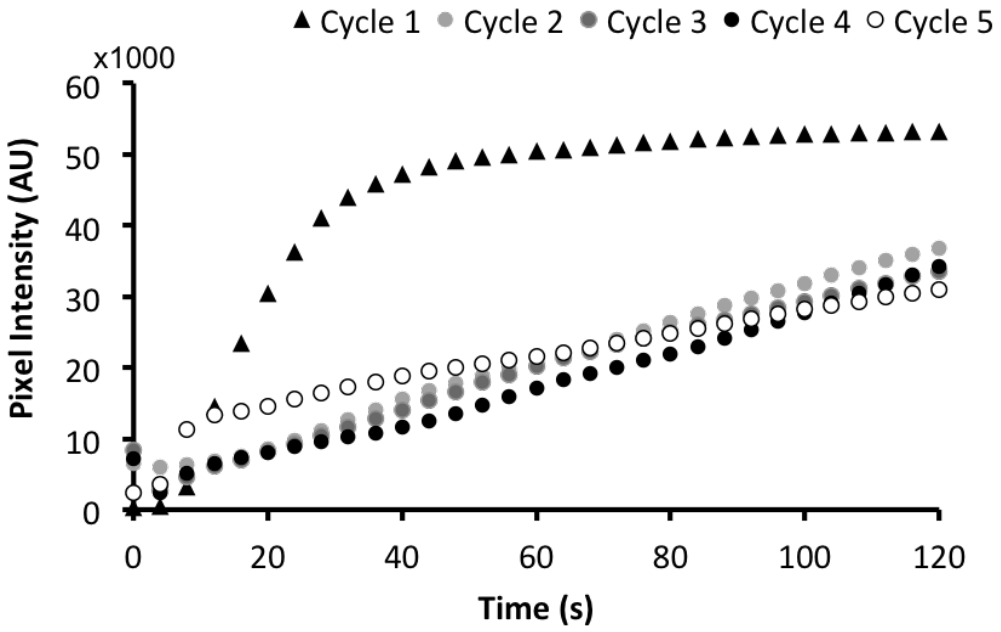


Figure 4.18 Immobilized enzyme recycle

Crystal sample 3 from Figure 5, after the initial experiment (cycle 1), was washed for 48 hrs in large reservoir of Buffer A prior to use in cycles 2 through 4. The crystal was washed in Buffer A for 30 minutes between each cycle 2 through 4 to remove residual resorufin. The crystal was then incubated in a large reservoir of Buffer A for 16 days prior to cycle 5. Cycles 2 through 5 consisted of exposure to 100 uM glucose and 10 uM AmplexRed, as in Figure 4. Fluorescence intensity was detected under 561 nm wavelength light on a spinning disk confocal microscope.

We hypothesize that the initial loss of fluorescence between cycle 1 and cycle 2 could be caused by loss of GOx enzyme due to incomplete BSA/glyoxal crosslinking. It is likely that some unbound enzyme diffused from the crystal pores during the 48hr wash period. When a similar experiment was performed using BSA and glutaraldehyde, activity was maintained at a more consistent rate after multiple use cycles. Glutaraldehyde is highly reactive and readily polymerizes,[184,185] likely resulting in high enzyme retention within the crystal. Even after three days storage in Buffer A at 4$^{o}$C and five reuse cycles, the GOx/BSA/glutaraldehyde crystal maintained >85% relative

activity. A crystal stored at 4°C for 62 days displayed low but detectable activity on AmplexRed.

*Immobilized enzyme thermal stability*

Enhanced thermal tolerance is often a benefit of enzyme immobilization. In order to test the thermal stability of hHRP enzyme immobilized within CJ crystals, a known quantity of hHRP was loaded into two equally-sized crystals. Resorufin production from both samples was monitored using a fluorescence plate reader (Fig. 4.19).

One sample was kept at room temperature while the second sample was incubated at 45°C for 10 minutes prior to the reaction. The second sample was also maintained at 45°C throughout the reaction. The experiment was simultaneously performed on the same concentration of free enzyme in solution. Free enzyme in solution at 45°C exhibited decreased rates of product formation and lower overall product formation than free enzyme at room temperature, whereas enhanced substrate and product diffusion and heat tolerance in immobilized enzymes may have contributed to the increased product formation at elevated temperatures in the immobilized samples.

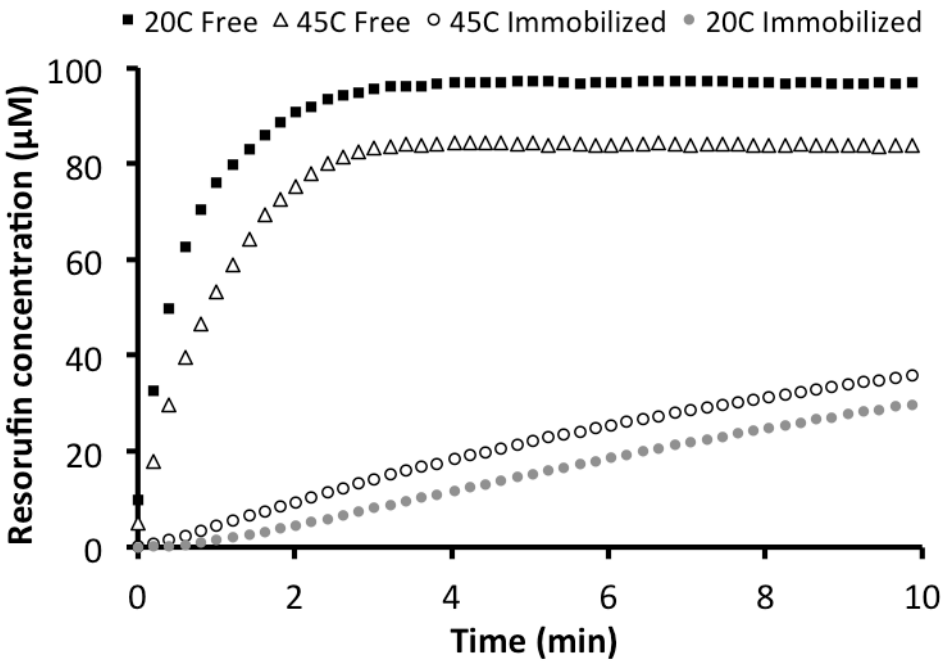


Figure 4.19 Enhanced thermal stability in immobilized enzymes

At 45°C, free enzyme in solution (45C free) had lower rates of product formation than free enzyme at room temperature (20C Free). Immobilized hHRP showed higher rates of product formation than the same concentration of immobilized enzyme at room temperature. All reactions were performed with 100 µM AmplexRed and 100 µM $H_2O_2$. Resorufin production was monitored under 561 nm wavelength light using a fluorescence plate reader.

This experiment was repeated with additional crystal samples at higher temperatures and more rigorous washing conditions with similar results (Figs. 4.20, 4.21). In Figure 4.20, three crystals of equal volume and dimensions were loaded with the same amount of hHRP. One crystal was incubated at 80°C for 10 minutes, while one crystal was incubated at 60°C for 10 minutes, and one crystal remained at room temperature. After the 10 minutes, the 80°C and 50°C crystals were moved into a new solution of Buffer A, effectively removing any enzyme that had diffused out of the crystal during the high temperature incubation. The room temperature crystal remained at 20°C

but was also transferred to a new drop of buffer. Each crystal was reacted with 100 μM AmplexRed and 100 μM $H_2O_2$, and resorufin product formation at 561 nm wavelength light was monitored. In this case, exposure to increased temperatures did decrease product formation for the immobilized enzymes (Fig. 4.20). This supports our previous hypothesis that some enzyme escaped the crystal during the pre-incubation step in Figure 4.19.

For free enzyme in solution (Fig. 4.21), increased temperatures had the expected effect of lowering the overall rate of production formation and amount of product formed. Notably, at 80°C, free enzyme activity is severely inhibited. The initial rate of product formation was approximately 53x less than at room temperature. In the immobilized enzyme, the initial rate of product formation was only about 5x less than the corresponding rate at room temperature.

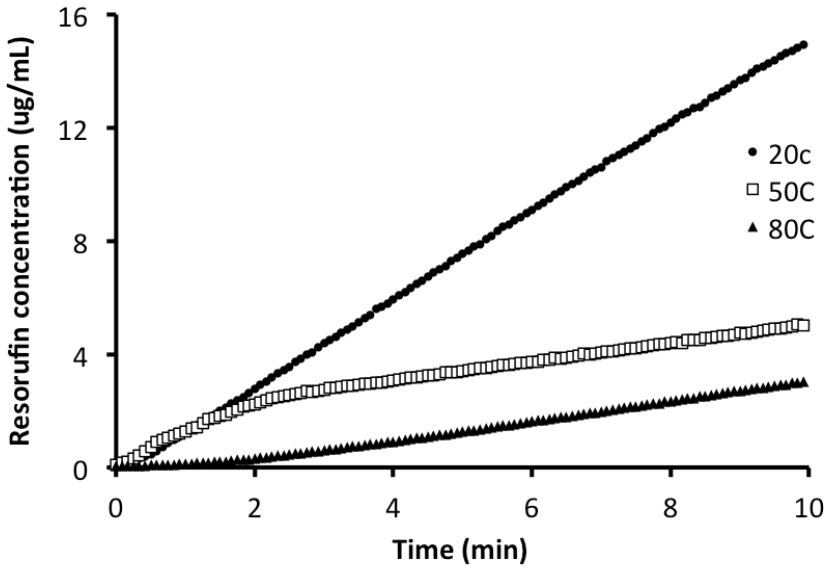


Figure 4.20 Immobilized enzyme thermal stability

Resorufin production from immobilized hHRP enzyme within CJ crystals exposed to 100 µM AmplexRed and 100 µM $H_2O_2$. Crystals were incubated at the specified temperatures for 10 minutes prior to the reaction. The 80°C and 50°C crystals were held at 45°C during the reaction. Resorufin production was detected at 561 nm on a fluorescence plate reader.

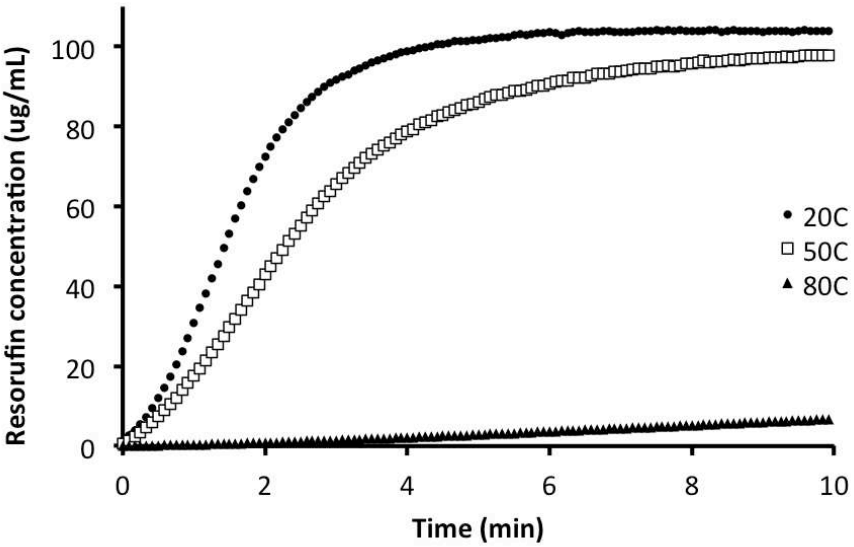


Figure 4.21 Free enzyme thermal stability

Resorufin production from free hHRP enzyme in Buffer A exposed to 100 μM AmplexRed and 100 μM $H_2O_2$. Samples were incubated at the specified temperatures for 10 minutes prior to the reaction. The 80°C and 60°C samples were held at 45°C during the reaction. Resorufin production was detected at 561 nm on a fluorescence plate reader.

## CONCLUSIONS

The benefits of crosslinked protein crystals[186] and crosslinked enzyme crystals[187] have been realized for many years, but the discovery of highly porous protein crystals with connected solvent channels greatly expands the list of potential applications.

We show here that porous protein crystals can be used to synthesize novel host-guest catalytic materials via controlled loading of macromolecules. Enzymes can be immobilized within the crystal pores and a two-enzyme pathway remains active for several recycles over multiple weeks. Despite having a slightly lower

activity ($k_{cat}$) than free enzyme in solution, preliminary work suggests these immobilized enzymes may have significant solvent and thermal stability imparted by the crosslinked, highly stable protein crystal.

Other protein crystals with smaller or larger pore sizes could be used to tailor specific diffusion properties. The range of possible protein modifications and crystal sizes provides a versatile and robust crystalline chassis for enzyme immobilization.

## EXPERIMENTAL

### *Protein crystal and enzyme preparation*

Horseradish peroxidase (HRP, Pierce™ #31490), HisProbe™-HRP conjugate (hHRP, Pierce™ #15165) and glucose oxidase from *Aspergillus niger* (GOX, SigmaAldrich #G7141) were purchased from commercial suppliers and used without further purification. The codon optimized gene encoding the *Campylobacter jejuni* protein (CJ, GenBank ID CJ0420) was independently cloned into the pSB3 expression vector. CJ was expressed in *E. coli* strains C41(DE3) and BL21(DE3), respectively. The target protein were purified from cell lysate via immobilized metal affinity chromatography. Prior to crystallization, CJ was dialyzed into 10 mM HEPES pH 7.5, 150 mM NaCl, 10% glycerol.

Enzymes were fluorescently labeled using blue (CF™405S succinimidyl ester, Biotium #92110) or green (NHS-fluorescien, ThermoFisher #46410) dyes for imaging via confocal fluorescence microscopy.

CJ was crystallized via sitting drop vapor diffusion by mixing 1 µl of ~15 mg/mL purified protein with 1 µl of crystallization buffer (3.2-3.5 M ammonium sulfate, pH 6.5). After overnight growth, CJ crystals were crosslinked using glyoxal to improve crystal stability. Glyoxal crosslinking steps consisted of a 30 minute wash in 4.2 M trimethylamine oxide (TMAO) buffer at pH 7.5, a two hour crosslink at room temperature in TMAO supplemented with 1% glyoxal, and a one hour quench in 1 M hydroxylamine with 100 mM DMAB at pH 5.0.

*Confocal loading and catalysis*

CJ crystals were attached via UV-curable glue to a glass slide to permit rapid substrate introduction or solution changes. For attachment, a small drop of Bondic glue was placed on a clean glass slide. The drop of glue was spread thin using a piece of wire and pre-cured for 5-10 seconds under 365 nm light to a tacky consistency. Next, 10-20 µl of storage buffer (Buffer A) was placed over the drop of glue. A crystal was looped into the solution and pressed gently into the glue at the desired orientation. The glue was cured for another 1-2 mins. Images were collected on a Nikon Eclipse Ti spinning-disk confocal microscope with an Andor iXon Ultra 897U EMCCD camera. Blue, green, and red fluorescent dyes were imaged using 405 nm, 488 nm, or 561 nm excitation wavelengths, respectively. Laser intensity was set to 20% for enzyme detection or 10% for product detection. All images were collected with a 100 ms exposure time and four-frame image averaging.

Prior to soaking in enzymes, each crosslinked CJ crystal was incubated for ~1 hr in Buffer A (50 mM HEPES, 300 mM NaCl, 10% glycerol, pH 7.5) with 10

mM nickel sulfate added for metal binding proteins. Crystals were then looped into ~1 mg/mL enzyme solutions in Buffer A and allowed to equilibrate at room temperature for at least one hour.

The activity of the HRP/GOx pathway was assessed on the substrate AmplexRed (ThermoFisher #A12222) by tracking resorufin product fluorescence at 561 nm excitation. For each reaction, a single enzyme-laden crystal was incubated with 10 μM AmplexRed and 100 μM glucose. Product formation was determined by measuring fluorescence intensity within a 25 μm x 25 μm square in the center of each crystal, or as an average over the entire image. Triplicate reactions were performed for each control.

*Fluorescence plate reader loading and catalysis*

A minimum of three crystals of known volume were placed in a 150 μL drop of known concentration hHRP in Buffer A (~30 μg/mL). At 0, 20, 40, 60, 80, and 100 minutes, and 20 and 24 hours, a 75 μL sample of the fluorescein-tagged hHRP solution was placed in a Costar black-walled 96-well plate (Corning, CLS3595) and fluorescence intensity was measured via excitation at 490 nm on a FLUOstar Omega plate reader (BMG Labtech). The fluorescence intensity was compared to a standard curve to determine protein concentration in the well. The standard curve was created using tagged hHRP of known concentrations (Fig. S1).

Resorufin product formation was monitored at 561 nm wavelength light on a FLUOstar Omega fluorescence plate reader (BMG Labtech). 100 μL aliquots of either free hHRP in Buffer A or hHRP immobilized within CJ crystals were used for all

experiments. Data was collected every 4-5 seconds after substrate addition, and the 96-well plate was shaken for 1 second between each timepoint.

# CONCLUSIONS AND FUTURE DIRECTIONS

The overarching goal of this work is to explore the feasibility of protein crystals as biotemplates and hybrid materials. We have shown that protein crystals can strongly adsorb and immobilize gold nanoparticles by reversible metal affinity interactions (Ch. II) and that these nanoparticles can serve as nucleation sites for the growth of nanorods within the pores of protein crystals by a variety of gold growth methods (Ch. III). Despite their stability, these crystals can be dissolved to release the gold structures, which can be analyzed by electron microscopy and elemental analysis. In Ch. IV, we showed that the crystals can entrap larger guests such as enzymes using the same metal affinity as in Ch. II, and the enzymes remain active while immobilized. The immobilized enzymes are reusable and exhibit enhanced thermal stability. Overall, this work contributes to the applications of protein crystals in nanomaterials and devices. The stability, many functional groups, and high solvent percentage of protein crystals makes them an ideal candidate for use as a templating scaffold.

There are a myriad of future directions in the field of biotemplating. We hope to expand to templating other structures, as preliminary work has been completed with carbon nanotubes, conductive polymers, semiconducting quantum dots, and lanthanide metals. Additionally, we plan to employ permanent or more rigid capture methods that may allow for atomic level precision over the placement of guests within the crystal. For example, if $Au_{25}$ clusters were covalently attached by ligand exchange to one or more cysteine residues within the crystal, both the placement and orientation of the cluster could be controlled to a higher precision.

With regards to *in situ* gold nanorod growth, high throughput imaging is crucial to elucidate the products formed from each distinct synthesis protocol. As it stands, we still don't know whether some of the phenomenon we witness (e.g. interconnected rod bundles, and varying rod widths and lengths) are a product of the syntheses themselves, or the harsh methods used to dissolve the crystal and image the resulting gold structures. The two most promising methods to visualize gold products within the crystals (TEM and spectroscopy) have been challenging thus far, and optimization of those protocols should be the next steps in this project. Additionally, it would be enlightening to monitor via spectroscopy the adsorption of $Au_{25}$ particles into the crystal in the axial and lateral orientations prior to growth. The location and concentration of these seeds particles presumably plays a large role in the resulting gold nanostructures.

It would also be beneficial to employ a covalent capture method for enzymes within the crystal pores. This may further enhance immobilized enzyme benefits such as recycle and thermal stability. Additionally, the use of multiple, distinct capture strategies may allow for the precise placement of different enzymes in close proximity for added pathway channeling benefits. In thinking about the industrial relevance of protein crystal immobilized enzymes, the development of improved microcrystal growth and handling methods are significant. For many protein crystal applications, we should perfect crystallization, crosslinking, and guest loading of large quantities of microcrystals. Additionally, it would be beneficial to test various separations methods (e.g. filtration, centrifugation, magnetic separation) to separate the microcrystals from the product.

For nanotemplating applications, protein crystal scaffolds will become more relevant as design strategies improve. Protein crystals have near infinite design

potential, and we can imagine a future in which the crystal scaffold is constructed specifically for each individual application, from targeted drug delivery to catalysis to inorganic nanostructure synthesis.

REFERENCES


1. Brust, M. & Kiely, C. J. Some recent advances in nanostructure preparation from gold and silver particles: a short topical review. *Colloids Surf. Physicochem. Eng. Asp.* **202,** 175–186 (2002).
2. Lee, S.-Y., Lim, J.-S. & Harris, M. T. Synthesis and application of virus-based hybrid nanomaterials. *Biotechnol. Bioeng.* **109,** 16–30 (2012).
3. Sharma, S., Gupta, N. & Srivastava, S. Modulating electron transfer properties of gold nanoparticles for efficient biosensing. *Biosens. Bioelectron.* **37,** 30–37 (2012).
4. Zeng, S. & Indrajit, R. A Review on functionalized gold nanoparticles for biosensing applications. *Plasmonics* **6,** 491–506 (2011).
5. Wang, Z. *et al.* Rapid Charging of Thermal Energy Storage Materials through Plasmonic Heating. *Sci. Rep.* **4,** (2014).
6. DaCosta, M. V., Doughan, S., Han, Y. & Krull, U. J. Lanthanide upconversion nanoparticles and applications in bioassays and bioimaging: A review. *Anal. Chim. Acta* **832,** 1–33 (2014).
7. Huang, X., Jain, P. K., El-Sayed, I. H. & El-Sayed, M. A. Gold nanoparticles: interesting optical properties and recent applications in cancer diagnostics and therapy. *Nanomed.* **2,** 681–693 (2007).
8. Jain, P. K., Lee, K. S., El-Sayed, I. H. & El-Sayed, M. A. Calculated Absorption and Scattering Properties of Gold Nanoparticles of Different Size, Shape, and Composition: Applications in Biological Imaging and Biomedicine. *J. Phys. Chem. B* **110,** 7238–7248 (2006).

9. Pissuwan, D., Niidome, T. & Cortie, M. B. The forthcoming applications of gold nanoparticles in drug and gene delivery systems. *J. Control. Release Off. J. Control. Release Soc.* **149,** 65–71 (2011).
10. Pérez-Juste, J., Pastoriza-Santos, I., Liz-Marzán, L. M. & Mulvaney, P. Gold nanorods: Synthesis, characterization and applications. *Coord. Chem. Rev.* **249,** 1870–1901 (2005).
11. Vreede, L. de, Göeken, K., Gill, R., Berg, A. van den & Eijkel, J. Fabrication of gold-nanoparticle arrays using photolithography and thermal dewetting. in *Proceedings of MicroTAS 2013, Freiburg, Germany, 27-31 October 2013* (ed. Zengerle, R.) 1418–1420 (The Priniting House, 2013).
12. Tan, B. J. Y. *et al.* Fabrication of Size-Tunable Gold Nanoparticles Array with Nanosphere Lithography, Reactive Ion Etching, and Thermal Annealing. *J. Phys. Chem. B* **109,** 11100–11109 (2005).
13. Fischer, S. *et al.* Shape and Interhelical Spacing of DNA Origami Nanostructures Studied by Small-Angle X-ray Scattering. *Nano Lett.* **16,** 4282–4287 (2016).
14. Zhan, P. *et al.* Reconfigurable Three-Dimensional Gold Nanorod Plasmonic Nanostructures Organized on DNA Origami Tripod. *ACS Nano* **11,** 1172–1179 (2017).
15. Okuda, M. *et al.* Fe3O4 nanoparticles: protein-mediated crystalline magnetic superstructures. *Nanotechnology* **23,** 415601 (2012).
16. King, N. P. *et al.* Accurate design of co-assembling multi-component protein nanomaterials. *Nature* **510,** 103–108 (2014).

17. Sotiropoulou, S., Sierra-Sastre, Y., Mark, S. S. & Batt, C. A. Biotemplated Nanostructured Materials. *Chem. Mater.* **20,** 821–834 (2008).
18. Cohen-Hadar, N. *et al.* Monitoring the stability of crosslinked protein crystals biotemplates: a feasibility study. *Biotechnol. Bioeng.* **94,** 1005–1011 (2006).
19. McMillan, R. A. *et al.* A Self-Assembling Protein Template for Constrained Synthesis and Patterning of Nanoparticle Arrays. *J. Am. Chem. Soc.* **127,** 2800–2801 (2005).
20. Zhang, D. & Paukstelis, P. J. Enhancing DNA Crystal Durability Through Chemical Crosslinking. *ChemBioChem* (2016).
21. Abe, S. & Ueno, T. Design of protein crystals in the development of solid biomaterials. *RSC Adv.* **5,** 21366–21375 (2015).
22. Ueno, T. Porous protein crystals as reaction vessels. *Chem. Eur. J.* **19,** 9096–9102 (2013).
23. Kostiainen, M. A. *et al.* Electrostatic assembly of binary nanoparticle superlattices using protein cages. *Nat. Nanotechnol.* **8,** 52–56 (2013).
24. Tabe, H., Abe, S., Hikage, T., Kitagawa, S. & Ueno, T. Porous protein crystals as catalytic vessels for organometallic complexes. *Chem. Asian J.* **9,** 1373–1378 (2014).
25. England, M. W. *et al.* Fabrication of polypyrrole nano-arrays in lysozyme single crystals. *Nanoscale* **4,** 6710–6713 (2012).
26. Tetter, S. & Hilvert, D. Enzyme Encapsulation by a Ferritin Cage. *Angew. Chem. Int. Ed Engl.* **56,** 14933–14936 (2017).

27. Liljeström, V., Mikkilä, J. & Kostiainen, M. A. Self-assembly and modular functionalization of three-dimensional crystals from oppositely charged proteins. *Nat. Commun.* **5,** (2014).
28. Wang, C. C. D. *et al.* Optical and electrical effects of gold nanoparticles in the active layer of polymer solar cells. *J. Mater. Chem.* **22,** 1206–1211 (2011).
29. Huang, X. & El-Sayed, M. A. Gold nanoparticles: Optical properties and implementations in cancer diagnosis and photothermal therapy. *J. Adv. Res.* **1,** 13–28 (2010).
30. Bohren, C. F. & Huffman, D. R. Absorption and Scattering by a Sphere. in *Absorption and Scattering of Light by Small Particles* 82–129 (Wiley-VCH Verlag GmbH, 1998). doi:10.1002/9783527618156.ch4
31. Papavassiliou, G. C. Optical properties of small inorganic and organic metal particles. *Prog. Solid State Chem.* **12,** 185–271 (1979).
32. *Optical Properties of Metal Clusters* | *Uwe Kreibig* | *Springer*.
33. Crespo, P. *et al.* Permanent Magnetism, Magnetic Anisotropy, and Hysteresis of Thiol-Capped Gold Nanoparticles. *Phys. Rev. Lett.* **93,** 87204 (2004).
34. Link, S. & El-Sayed, M. A. Shape and size dependence of radiative, non-radiative and photothermal properties of gold nanocrystals. *Int Rev. Phys. Chem.* **19,** 409–453 (2000).
35. Nealon, G. L. *et al.* Magnetism in gold nanoparticles. *Nanoscale* **4,** 5244–5258 (2012).
36. Wang, L., Xu, L., Kuang, H., Xu, C. & Kotov, N. A. Dynamic Nanoparticle Assemblies. *Acc. Chem. Res.* **45,** 1916–1926 (2012).

37. Mirkin, C. A., Letsinger, R. L., Mucic, R. C. & Storhoff, J. J. A DNA-based method for rationally assembling nanoparticles into macroscopic materials. *Nature* **382,** 607–609 (1996).

38. Funston, A. M., Novo, C., Davis, T. J. & Mulvaney, P. Plasmon coupling of gold nanorods at short distances and in different geometries. *Nano Lett.* **9,** 1651–1658 (2009).

39. Maier, S. A. *et al.* Plasmonics—A Route to Nanoscale Optical Devices. *Adv. Mater.* **13,** 1501–1505 (2001).

40. Elghanian, R., Storhoff, J. J., Mucic, R. C., Letsinger, R. L. & Mirkin, C. A. Selective Colorimetric Detection of Polynucleotides Based on the Distance-Dependent Optical Properties of Gold Nanoparticles. *Science* **277,** 1078–1081 (1997).

41. Observation of coupled plasmon-polariton modes in Au nanoparticle chain waveguides of different lengths: Estimation of waveguide loss. *Appl. Phys. Lett.* **81,** 1714–1716 (2002).

42. Maier, S. A., Brongersma, M. L., Kik, P. G. & Atwater, H. A. Observation of near-field coupling in metal nanoparticle chains using far-field polarization spectroscopy. *Phys. Rev. B* **65,** 193408 (2002).

43. Yamaki, M., Higo, J. & Nagayama, K. Size-Dependent Separation of Colloidal Particles In Two-Dimensional Convective Self-Assembly. *Langmuir* **11,** 2975–2978 (1995).

44. Kiely, C. J., Fink, J., Brust, M., Bethell, D. & Schiffrin, D. J. Spontaneous ordering of bimodal ensembles of nanoscopic gold clusters. *Nature* **396,** 444–446 (1998).

45. Musick, M. D., Keating, C. D., Keefe, M. H. & Natan, M. J. Stepwise Construction of Conductive Au Colloid Multilayers from Solution. *Chem. Mater.* **9,** 1499–1501 (1997).

46. Brust, M., Bethell, D., Kiely, C. J. & Schiffrin, D. J. Self-Assembled Gold Nanoparticle Thin Films with Nonmetallic Optical and Electronic Properties. *Langmuir* **14,** 5425–5429 (1998).

47. Joseph, Y. *et al.* Self-Assembled Gold Nanoparticle/Alkanedithiol Films: Preparation, Electron Microscopy, XPS-Analysis, Charge Transport, and Vapor-Sensing Properties. *J. Phys. Chem. B* **107,** 7406–7413 (2003).

48. Wessels, J. M. *et al.* Optical and Electrical Properties of Three-Dimensional Interlinked Gold Nanoparticle Assemblies. *J. Am. Chem. Soc.* **126,** 3349–3356 (2004).

49. Shiigi, H. & Nagaoka, T. Molecularly bridged gold nanoparticle array for sensing applications. *Anal. Sci. Int. J. Jpn. Soc. Anal. Chem.* **30,** 89–96 (2014).

50. Boisselier, E. & Astruc, D. Gold nanoparticles in nanomedicine: preparations, imaging, diagnostics, therapies and toxicity. *Chem. Soc. Rev.* **38,** 1759–1782 (2009).

51. Shipway, A., Katz, E. & Willner, I. Nanoparticle arrays on surface of electronic, optical, and sensor applications. *ChemPhysChem* **1,** 18–52 (2000).

52. Wilson, R. The use of gold nanoparticles in diagnostics and detection. *Chem. Soc. Rev.* **37,** 2028–2045 (2008).

53. Rai, A., Prabhune, A. & Perry, C. C. Antibiotic mediated synthesis of gold nanoparticles with potent antimicrobial activity and their application in antimicrobial coatings. *J. Mater. Chem.* **20,** 6789–6798 (2010).
54. Cai, W., Gao, T., Hong, H. & Sun, J. Applications of gold nanoparticles in cancer nanotechnology. *Nanotechnol. Sci. Appl.* **2008,** (2008).
55. Jain, S., Hirst, D. G. & O'Sullivan, J. M. Gold nanoparticles as novel agents for cancer therapy. *Br. J. Radiol.* **85,** 101–113 (2012).
56. StephanT Stern, ScottE McNeil, AnilK Patri & MarinaA Dobrovolskaia. Preclinical Characterization of Engineered Nanoparticles Intended for Cancer Therapeutics. in *Nanotechnology for Cancer Therapy* 105–137 (CRC Press, 2006).
57. Murphy, C. J. *et al.* Gold Nanoparticles in Biology: Beyond Toxicity to Cellular Imaging. *Acc. Chem. Res.* **41,** 1721–1730 (2008).
58. Zhang, Z., Ross, R. D. & Roeder, R. K. Preparation of functionalized gold nanoparticles as a targeted X-ray contrast agent for damaged bone tissue. *Nanoscale* **2,** 582–586 (2010).
59. Peng, G. *et al.* Detection of lung, breast, colorectal, and prostate cancers from exhaled breath using a single array of nanosensors. *Br. J. Cancer* **103,** 542–551 (2010).
60. Dimitratos, N., Lopez-Sanchez, J. A. & Hutchings, G. J. Selective liquid phase oxidation with supported metal nanoparticles. *Chem. Sci.* **3,** 20–44 (2011).
61. Daniel, M.-C. & Astruc, D. Gold nanoparticles: assembly, supramolecular chemistry, quantum-size-related properties, and applications toward biology, catalysis, and nanotechnology. *Chem. Rev.* **104,** 293–346 (2004).

62. Hashmi, A. S. K. The Catalysis Gold Rush: New Claims. *Angew. Chem. Int. Ed.* **44,** 6990–6993 (2005).

63. Suresh, V. *et al.* Hierarchically Built Gold Nanoparticle Supercluster Arrays as Charge Storage Centers for Enhancing the Performance of Flash Memory Devices. *ACS Appl. Mater. Interfaces* **7,** 279–286 (2015).

64. Zhu, G. *et al.* Toward Large-Scale Energy Harvesting by a Nanoparticle-Enhanced Triboelectric Nanogenerator. *Nano Lett.* **13,** 847–853 (2013).

65. Yue, W. *et al.* Electron-beam lithography of gold nanostructures for surface-enhanced Raman scattering. *J. Micromechanics Microengineering* **22,** 125007 (2012).

66. Boal, A. K. *et al.* Self-assembly of nanoparticles into structured spherical and network aggregates. *Nature* **404,** 746–748 (2000).

67. Liu, S., Zhu, T., Hu, R. & Liu, Z. Evaporation-induced self-assembly of gold nanoparticles into a highly organized two-dimensional array. *Phys. Chem. Chem. Phys.* **4,** 6059–6062 (2002).

68. Lin, G., Chee, S. W., Raj, S., Král, P. & Mirsaidov, U. Linker-Mediated Self-Assembly Dynamics of Charged Nanoparticles. *ACS Nano* **10,** 7443–7450 (2016).

69. Fukuoka, A. *et al.* Template Synthesis of Nanoparticle Arrays of Gold and Platinum in Mesoporous Silica Films. *Nano Lett.* **2,** 793–795 (2002).

70. Lamarre, S. S., Lemay, C., Labrecque, C. & Ritcey, A. M. Controlled 2D Organization of Gold Nanoparticles in Block Copolymer Monolayers. *Langmuir* **29,** 10891–10898 (2013).

71. Khullar, P. *et al.* Block Copolymer Micelles as Nanoreactors for Self-Assembled Morphologies of Gold Nanoparticles. *J. Phys. Chem. B* **117,** 3028–3039 (2013).
72. Ding, B. *et al.* Gold nanoparticle self-similar chain structure organized by DNA origami. *J. Am. Chem. Soc.* **132,** 3248–3249 (2010).
73. Chou, L. Y. T., Zagorovsky, K. & Chan, W. C. W. DNA assembly of nanoparticle superstructures for controlled biological delivery and elimination. *Nat. Nanotechnol.* **9,** 148–155 (2014).
74. Klein, W. P. *et al.* Multiscaffold DNA origami nanoparticle waveguides. *Nano Lett.* **13,** 3850–3856 (2013).
75. Thacker, V. V. *et al.* DNA origami based assembly of gold nanoparticle dimers for surface-enhanced Raman scattering. *Nat. Commun.* **5,** 3448 (2014).
76. Auyeung, E. *et al.* DNA-mediated nanoparticle crystallization into Wulff polyhedra. *Nature* **505,** 73–77 (2014).
77. Schreiber, R. *et al.* Hierarchical assembly of metal nanoparticles, quantum dots and organic dyes using DNA origami scaffolds. *Nat. Nanotechnol.* **9,** 74–78 (2014).
78. Zhao, Z., Jacovetty, E. L., Liu, Y. & Yan, H. Encapsulation of Gold Nanoparticles in a DNA Origami Cage. *Angew. Chem. Int. Ed.* **50,** 2041–2044 (2011).
79. Ackerson, C. J., Sykes, M. T. & Kornberg, R. D. Defined DNA/nanoparticle conjugates. *Proc. Natl. Acad. Sci. U. S. A.* **102,** 13383–13385 (2005).
80. Aldaye, F. A. & Sleiman, H. F. Dynamic DNA templates for discrete gold nanoparticle assemblies: control of geometry, modularity, write/erase and structural switching. *J. Am. Chem. Soc.* **129,** 4130–4131 (2007).

81. Alivisatos, A. P. *et al.* Organization of 'nanocrystal molecules' using DNA. *Nature* **382,** 609–611 (1996).

82. Bell, N. A. W. *et al.* DNA origami nanopores. *Nano Lett.* **12,** 512–517 (2012).

83. Chen, P.-Y. *et al.* Versatile Three-Dimensional Virus-Based Template for Dye-Sensitized Solar Cells with Improved Electron Transport and Light Harvesting. *ACS Nano* (2013). doi:10.1021/nn4014164

84. Huang, Y. *et al.* Programmable assembly of nanoarchitectures using genetically engineered viruses. *Nano Lett.* **5,** 1429–1434 (2005).

85. Amy Szuchmacher Blum, C. M. S. Cowpea Mosaic Virus as a Scaffold for 3-D Patterning of Gold Nanoparticles. *Nano Lett. - NANO LETT* **4,** (2004).

86. McMillan, R. A. *et al.* Ordered nanoparticle arrays formed on engineered chaperonin protein templates. *Nat. Mater.* **1,** 247–252 (2002).

87. Ackerson, C. J., Jadzinsky, P. D., Jensen, G. J. & Kornberg, R. D. Rigid, specific, and discrete gold nanoparticle/antibody conjugates. *J. Am. Chem. Soc.* **128,** 2635–2640 (2006).

88. Sexton, J. Z. & Ackerson, C. J. Determination of Rigidity of Protein Bound Au(144) Clusters by Electron Cryomicroscopy. *J. Phys. Chem. C Nanomater. Interfaces* **114,** 16037–16042 (2010).

89. Baneyx, F. & Matthaei, J. F. Self-assembled two-dimensional protein arrays in bionanotechnology: from S-layers to designed lattices. *Curr. Opin. Biotechnol.* **28,** 39–45 (2014).

90. Sarikaya, M., Tamerler, C., Jen, A. K.-Y., Schulten, K. & Baneyx, F. Molecular biomimetics: nanotechnology through biology. *Nat. Mater.* **2,** 577–585 (2003).

91. Gradisar, H. *et al.* Design of a single-chain polypeptide tetrahedron assembled from coiled-coil segments. *Nat. Chem. Biol.* **9,** (2013).
92. Györvary, E. *et al.* Formation of nanoparticle arrays on S-layer protein lattices. *J. Nanosci. Nanotechnol.* **4,** 115–120 (2004).
93. Deschaume, O. *et al.* Synthesis and Properties of Gold Nanoparticle Arrays Self-Organized on Surface-Deposited Lysozyme Amyloid Scaffolds. *Chem. Mater.* **26,** 5383–5393 (2014).
94. Maity, B., Abe, S. & Ueno, T. Observation of gold sub-nanocluster nucleation within a crystalline protein cage. *Nat. Commun.* **8,** 14820 (2017).
95. Takeda, Y., Kondow, T. & Mafuné, F. Self-assembly of gold nanoparticles in protein crystal. *Chem. Phys. Lett.* **504,** 175–179 (2011).
96. Berman, H. M. *et al.* The Protein Data Bank. *Nucleic Acids Res.* **28,** 235–242 (2000).
97. Krauss, I. R., Merlino, A., Vergara, A. & Sica, F. An overview of biological macromolecule crystallization. *Int J Mol Sci* **14,** 11643–11691 (2013).
98. Szöke, A., Szöke, H. & Somoza, J. R. Holographic Methods in X-ray Crystallography. V. Multiple IsomorphousReplacement, Multiple Anomalous Dispersion and Non-crystallographic Symmetry. *Acta Crystallogr. A* **53,** 291–313 (1997).
99. Karle, J. Some developments in anomalous dispersion for the structural investigation of macromolecular systems in biology. *Int. J. Quantum Chem.* **18,** 357–367 (1980).

100. Kartha, G. & Parthasarathy, R. Combination of multiple isomorphous replacement and anomalous dispersion data for protein structure determination. I. Determination of heavy-atom positions in protein derivatives. *Acta Crystallogr.* **18,** 745–749 (1965).

101. Gnatt, A. L., Cramer, P., Fu, J., Bushnell, D. A. & Kornberg, R. D. Structural basis of transcription: an RNA polymerase II elongation complex at 3.3 A resolution. *Science* **292,** 1876–1882 (2001).

102. Abe, S. *et al.* Porous Protein Crystals as Reaction Vessels for Controlling Magnetic Properties of Nanoparticles. *Small* **8,** 1314–1319 (2012).

103. Koshiyama, T. *et al.* Modification of porous protein crystals in development of biohybrid materials. *Bioconjug. Chem.* **21,** 264–269 (2010).

104. Yamada, H., Kuroki, R., Hirata, M. & Imoto, T. Intramolecular cross-linkage of lysozyme. Imidazole catalysis of the formation of the cross-link between lysine-13 (epsilon-amino) and leucine-129 (alpha-carboxyl) by carbodiimide reaction. *Biochemistry (Mosc.)* **22,** 4551–4556 (1983).

105. Wu, Z. & Jin, R. On the Ligand's Role in the Fluorescence of Gold Nanoclusters. *Nano Lett.* **10,** 2568–2573 (2010).

106. Uchinomiya, S. *et al.* Site-specific covalent labeling of His-tag fused proteins with a reactive Ni(II)-NTA probe. *Chem. Commun. Camb. Engl.* 5880–5882 (2009). doi:10.1039/b912025d

107. Hainfeld, J. F., Liu, W., Halsey, C. M., Freimuth, P. & Powell, R. D. Ni-NTA-gold clusters target His-tagged proteins. *J. Struct. Biol.* **127,** 185–198 (1999).

108. Kröger, D., Liley, M., Schiweck, W., Skerra, A. & Vogel, H. Immobilization of histidine-tagged proteins on gold surfaces using chelator thioalkanes. *Biosens. Bioelectron.* **14,** 155–161 (1999).

109. Nieba, L. *et al.* BIACORE analysis of histidine-tagged proteins using a chelating NTA sensor chip. *Anal. Biochem.* **252,** 217–228 (1997).

110. Locatelli, E., Monaco, I. & Franchini, M. C. Surface modifications of gold nanorods for applications in nanomedicine. *RSC Adv.* **5,** 21681–21699 (2015).

111. Pérez-Juste, J., Pastoriza-Santos, I., Liz-Marzán, L. M. & Mulvaney, P. Gold nanorods: Synthesis, characterization and applications. *Coord. Chem. Rev.* **249,** 1870–1901 (2005).

112. Li, J.-X., Xu, Y., Dai, Q.-F., Lan, S. & Tie, S.-L. Manipulating light–matter interaction in a gold nanorod assembly by plasmonic coupling. *Laser Photonics Rev.* **10,** 826–834 (2016).

113. Draine, B. T. & Flatau, P. J. Discrete-Dipole Approximation For Scattering Calculations. *JOSA A* **11,** 1491–1499 (1994).

114. Electromagnetic fields around silver nanoparticles and dimers. *J. Chem. Phys.* **120,** 357–366 (2003).

115. Gold nanorod extinction spectra. *J. Appl. Phys.* **99,** 123504 (2006).

116. Kelly, K. L., Coronado, E., Zhao, L. L. & Schatz, G. C. The Optical Properties of Metal Nanoparticles: The Influence of Size, Shape, and Dielectric Environment. *J. Phys. Chem. B* **107,** 668–677 (2003).

117. Niidome, Y., Haine, A. T. & Niidome, T. Anisotropic gold-based nanoparticles: Preparation, properties, and applications. *Chem. Lett.* **45,** 488–498 (2016).

118. Stone, J., Jackson, S. & Wright, D. Biological applications of gold nanorods. *Wiley Interdiscip. Rev. Nanomed. Nanobiotechnol.* **3,** 100–109 (2011).

119. Ma, Z. *et al.* Applications of gold nanorods in biomedical imaging and related fields. *Chin. Sci. Bull.* **58,** 2530–2536 (2013).

120. Xue, C. & Li, Q. Anisotropic Gold Nanoparticles: Preparation, Properties, and Applications. in *Anisotropic Nanomaterials* (ed. Li, Q.) 69–118 (Springer International Publishing, 2015). doi:10.1007/978-3-319-18293-3_3

121. Priecel, P., Adekunle Salami, H., Padilla, R. H., Zhong, Z. & Lopez-Sanchez, J. A. Anisotropic gold nanoparticles: Preparation and applications in catalysis. *Chin. J. Catal.* **37,** 1619–1650 (2016).

122. Gaware, U., Kamble, V. & Ankamwar, B. Ecofriendly Synthesis of Anisotropic Gold Nanoparticles: A Potential Candidate of SERS Studies. *Int. J. Electrochem.* **2012,** e276246 (2012).

123. Jana, N. R., Gearheart, L. & Murphy, C. J. Seed-Mediated Growth Approach for Shape-Controlled Synthesis of Spheroidal and Rod-like Gold Nanoparticles Using a Surfactant Template. *Adv. Mater.* **13,** 1389–1393 (2001).

124. Park, K. *et al.* Growth Mechanism of Gold Nanorods. *Chem. Mater.* **25,** 555–563 (2013).

125. Takenaka, Y. & Kitahata, H. High-aspect-ratio gold nanorods synthesized in a surfactant gel phase. *Chem. Phys. Lett.* **467,** 327–330 (2009).

126. Scarabelli, L., Sánchez-Iglesias, A., Pérez-Juste, J. & Liz-Marzán, L. M. A 'Tips and Tricks' Practical Guide to the Synthesis of Gold Nanorods. *J. Phys. Chem. Lett.* **6,** 4270–4279 (2015).

127. Vigderman, L., Khanal, B. P. & Zubarev, E. R. Functional Gold Nanorods: Synthesis, Self-Assembly, and Sensing Applications. *Adv. Mater.* **24,** 4811–4841 (2012).

128. Burrows, N. D., Harvey, S., Idesis, F. A. & Murphy, C. J. Understanding the Seed-Mediated Growth of Gold Nanorods through a Fractional Factorial Design of Experiments. *Langmuir* **33,** 1891–1907 (2017).

129. Busbee, B. d., Obare, S. o. & Murphy, C. j. An Improved Synthesis of High-Aspect-Ratio Gold Nanorods. *Adv. Mater.* **15,** 414–416 (2003).

130. Zweifel, D. A. & Wei, A. Sulfide-Arrested Growth of Gold Nanorods. *Chem. Mater.* **17,** 4256–4261 (2005).

131. Boleininger, J., Kurz, A., Reuss, V. & Sönnichsen, C. Microfluidic continuous flow synthesis of rod-shaped gold and silver nanocrystals. *Phys. Chem. Chem. Phys. PCCP* **8,** 3824–3827 (2006).

132. Vigderman, L. High-Yield Synthesis and Applications of Anisotropic Gold Nanoparticles. (Rice University, 2013).

133. Ward, C. J., Tronndorf, R., Eustes, A. S., Auad, M. L. & Davis, E. W. Seed-Mediated Growth of Gold Nanorods: Limits of Length to Diameter Ratio Control. *J. Nanomater.* **2014,** e765618 (2014).

134. Smith, D. K. & Korgel, B. A. The Importance of the CTAB Surfactant on the Colloidal Seed-Mediated Synthesis of Gold Nanorods. *Langmuir* **24,** 644–649 (2008).

135. Gao, C., Zhang, Q., Lu, Z. & Yin, Y. Templated Synthesis of Metal Nanorods in Silica Nanotubes. *J. Am. Chem. Soc.* **133,** 19706–19709 (2011).

136. Lagziel-Simis, S., Cohen-Hadar, N., Moscovich-Dagan, H., Wine, Y. & Freeman, A. Protein-mediated nanoscale biotemplating. *Curr. Opin. Biotechnol.* **17,** 569–573 (2006).

137. Chen, C.-L., Zhang, P. & Rosi, N. L. A New Peptide-Based Method for the Design and Synthesis of Nanoparticle Superstructures: Construction of Highly Ordered Gold Nanoparticle Double Helices. *J. Am. Chem. Soc.* **130,** 13555–13557 (2008).

138. Guli, M., Lambert, E. M., Li, M. & Mann, S. Template-directed synthesis of nanoplasmonic arrays by intracrystalline metalization of cross-linked lysozyme crystals. *Angew. Chem. Int. Ed Engl.* **49,** 520–523 (2010).

139. Muskens, O. L., England, M. W., Danos, L., Li, M. & Mann, S. Plasmonic Response of Ag- and Au-Infiltrated Cross-Linked Lysozyme Crystals. *Adv. Funct. Mater.* n/a–n/a (2012). doi:10.1002/adfm.201201718

140. Liu, M. *et al.* Superior Catalytic Performance of Gold Nanoparticles Within Small Cross-Linked Lysozyme Crystals. *Langmuir* **32,** 10895–10904 (2016).

141. Reches, M. & Gazit, E. Casting Metal Nanowires Within Discrete Self-Assembled Peptide Nanotubes. *Science* **300,** 625–627 (2003).

142. Sone, E. D. & Stupp, S. I. Bioinspired Magnetite Mineralization of Peptide−Amphiphile Nanofibers. *Chem. Mater.* **23,** 2005–2007 (2011).

143. Yao, Q. *et al.* Understanding seed-mediated growth of gold nanoclusters at molecular level. *Nat. Commun.* **8,** 927 (2017).

144. Luo, Z. *et al.* Toward Understanding the Growth Mechanism: Tracing All Stable Intermediate Species from Reduction of Au(I)–Thiolate Complexes to Evolution of Au25 Nanoclusters. *J. Am. Chem. Soc.* **136,** 10577–10580 (2014).

145. Wei, H. *et al.* Time-dependent, protein-directed growth of gold nanoparticles within a single crystal of lysozyme. *Nat. Nanotechnol.* **6,** 93–97 (2011).

146. Merlino, A., Caterino, M., Krauss, I. R. & Vergara, A. Missing gold atoms in lysozyme crystals used to grow gold nanoparticles. *Nat. Nanotechnol.* **10,** 285 (2015).

147. Spherical Gold Nanoparticles Kit (30-90 nm) - Supplier Data by Strem Chemicals. *AZoNano.com* (2011). Available at: http://www.azonano.com/article.aspx?ArticleID=2875. (Accessed: 11th January 2017)

148. Introduction to Gold Nanoparticle Characterization. *Cytodiagnostics* (2017).

149. Xie, J., Zheng, Y. & Ying, J. Y. Protein-Directed Synthesis of Highly Fluorescent Gold Nanoclusters. *J. Am. Chem. Soc.* **131,** 888–889 (2009).

150. Basu, N., Bhattacharya, R. & Mukherjee, P. Protein-mediated autoreduction of gold salts to gold nanoparticles. *Biomed. Mater.* **3,** 34105 (2008).

151. Bhargava, S. K., Booth, J. M., Agrawal, S., Coloe, P. & Kar, G. Gold Nanoparticle Formation during Bromoaurate Reduction by Amino Acids. *Langmuir* **21,** 5949–5956 (2005).

152. Dreier, T. A. & Ackerson, C. J. Radicals are required for thiol etching of gold particles. *Angew. Chem. Int. Ed Engl.* **54,** 9249–9252 (2015).

153. Li, S., Yang, X., Yang, S., Zhu, M. & Wang, X. Technology Prospecting on Enzymes: Application, Marketing and Engineering. *Comput. Struct. Biotechnol. J.* **2,** (2012).

154. Kirk, O., Borchert, T. V. & Fuglsang, C. C. Industrial enzyme applications. *Curr. Opin. Biotechnol.* **13,** 345–351 (2002).

155. Sheldon, R. A. Enzyme immobilization: The quest for optimum performance. *Adv. Synth. Catal.* **349,** 1289–1307 (2007).

156. Beilen, J. B. van & Li, Z. Enzyme technology: an overview. *Curr. Opin. Biotechnol.* **13,** 338–344 (2002).

157. Garcia-Galan, C., Berenguer-Murcia, A., Fernandez-Lafuente, R. & Rodrigues, R. C. Potential of Different Enzyme Immobilization Strategies to Improve Enzyme Performance. *Adv. Synth. Catal.* **353,** 2885–2904 (2011).

158. Mohamad, N. R., Marzuki, N. H. C., Buang, N. A., Huyop, F. & Wahab, R. A. An overview of technologies for immobilization of enzymes and surface analysis techniques for immobilized enzymes. *Biotechnol. Biotechnol. Equip.* **29,** 205–220 (2015).

159. Xie, T. *et al.* Recent advance in the support and technology used in enzyme immobilization. *Afr. J. Biotechnol.* **8,** (2009).

160. Datta, S., Christena, L. R. & Rajaram, Y. R. S. Enzyme immobilization: an overview on techniques and support materials. *3 Biotech* **3,** 1–9 (2013).

161. Matto, M. & Husain, Q. Calcium alginate–starch hybrid support for both surface immobilization and entrapment of bitter gourd (Momordica charantia) peroxidase. *J. Mol. Catal. B Enzym.* **57,** 164–170 (2009).

162. Fortes, C. C. S., Daniel-da-Silva, A. L., Xavier, A. M. R. B. & Tavares, A. P. M. Optimization of enzyme immobilization on functionalized magnetic nanoparticles for laccase biocatalytic reactions. *Chem. Eng. Process. Process Intensif.* **117,** 1–8 (2017).

163. Asuri, P. *et al.* Water-soluble carbon nanotube-enzyme conjugates as functional biocatalytic formulations. *Biotechnol. Bioeng.* **95,** 804–811 (2006).

164. Jegan Roy, J. & Emilia Abraham, T. Strategies in making cross-linked enzyme crystals. *Chem. Rev.* **104,** 3705–3722 (2004).

165. Matijošytė, I., Arends, I. W. C. E., de Vries, S. & Sheldon, R. A. Preparation and use of cross-linked enzyme aggregates (CLEAs) of laccases. *J. Mol. Catal. B Enzym.* **62,** 142–148 (2010).

166. Preparation and characterization of cross-linked enzyme aggregates (CLEA) of Subtilisin for controlled release applications - ScienceDirect. Available at: https://www.sciencedirect.com/science/article/pii/S0141813008001384. (Accessed: 3rd October 2018)

167. Bhattacharya, A. & Pletschke, B. I. Magnetic cross-linked enzyme aggregates (CLEAs): A novel concept towards carrier free immobilization of lignocellulolytic enzymes. *Enzyme Microb. Technol.* **61–62,** 17–27 (2014).

168. Conrado, R. J., Varner, J. D. & DeLisa, M. P. Engineering the spatial organization of metabolic enzymes: mimicking nature's synergy. *Curr. Opin. Biotechnol.* **19,** 492–499 (2008).

169. Chen, A. H. & Silver, P. A. Designing biological compartmentalization. *Trends Cell Biol.* **22,** 662–670 (2012).

170. Whitaker, W. R. & Dueber, J. E. Metabolic pathway flux enhancement by synthetic protein scaffolding. *Methods Enzymol.* **497,** 447–468 (2011).

171. Bonacci, W. *et al.* Modularity of a carbon-fixing protein organelle. *Proc. Natl. Acad. Sci.* **109,** 478–483 (2012).

172. Müller, J. & Niemeyer, C. M. DNA-directed assembly of artificial multienzyme complexes. *Biochem. Biophys. Res. Commun.* **377,** 62–67 (2008).

173. Niemeyer, C. M., Koehler, J. & Wuerdemann, C. DNA-Directed Assembly of Bienzymic Complexes from In Vivo Biotinylated NAD(P)H:FMN Oxidoreductase and Luciferase. *ChemBioChem* **3,** 242–245 (2002).

174. Channon, K., Bromley, E. H. C. & Woolfson, D. N. Synthetic biology through biomolecular design and engineering. *Curr. Opin. Struct. Biol.* **18,** 491–498 (2008).

175. Synthesis of Methyl Halides from Biomass Using Engineered Microbes - Journal of the American Chemical Society (ACS Publications). Available at: https://pubs.acs.org/doi/10.1021/ja809461u. (Accessed: 3rd October 2018)

176. Fu, J., Liu, M., Liu, Y., Woodbury, N. W. & Yan, H. Interenzyme Substrate Diffusion for an Enzyme Cascade Organized on Spatially Addressable DNA Nanostructures. *J. Am. Chem. Soc.* **134,** 5516–5519 (2012).

177. Fu, J. *et al.* Multi-enzyme complexes on DNA scaffolds capable of substrate channelling with an artificial swinging arm. *Nat. Nanotechnol.* **9,** 531–536 (2014).

178. Geng, C. & Paukstelis, P. J. DNA Crystals as Vehicles for Biocatalysis. *J. Am. Chem. Soc.* **136,** 7817–7820 (2014).

179. Zhao, Z. *et al.* Nanocaged enzymes with enhanced catalytic activity and increased stability against protease digestion. *Nat. Commun.* **7,** (2016).

180. Liu, X. *et al.* Apoferritin–CeO2 nano-truffle that has excellent artificial redox enzyme activity. *Chem. Commun.* **48,** 3155–3157 (2012).

181. Abe, S. *et al.* Design of Enzyme-Encapsulated Protein Containers by In Vivo Crystal Engineering. *Adv. Mater. Deerfield Beach Fla* **27,** 7951–7956 (2015).

182. Quiocho, F. A. & Richards, F. M. The Enzymic Behavior of Carboxypeptidase-A in the Solid State*. *Biochemistry (Mosc.)* **5,** 4062–4076 (1966).

183. Doscher, M. S. & Richards, F. M. The Activity of an Enzyme in the Crystalline State: Ribonuclease S. *J. Biol. Chem.* **238,** 2399–2406 (1963).

184. Migneault, I., Dartiguenave, C., Bertrand, M. J. & Waldron, K. C. Glutaraldehyde: behavior in aqueous solution, reaction with proteins, and application to enzyme crosslinking. *BioTechniques* **37,** 790–796, 798–802 (2004).

185. Habeeb, A. F. S. A. & Hiramoto, R. Reaction of proteins with glutaraldehyde. *Arch. Biochem. Biophys.* **126,** 16–26 (1968).

186. Margolin, A. L. & Navia, M. A. Protein Crystals as Novel Catalytic Materials. *Angew. Chem. Int. Ed.* **40,** 2204–2222 (2001).

187. Nancy L. St. Clair, M. A. N. Cross-linked enzyme crystals as robust biocatalysts. J Am Chem Soc. *J. Am. Chem. Soc.* **114,** 7314–7316 (1992).

# APPENDIX

*DNASU Plasmid ID*
CjCD00089155

*CJ Protein Sequence*
MKEYTLDKAHTDVGFKIKHLQISNVKGNFKDYSAVIDFDPASAEFKKLDVTIKIASVNTENQTRDNHLQQD
DFFKAKKYPDMTFTMKKYEKIDNEKGKMTGTLTIAGVSKDIVLDAEIGGVAKGKDGKEKIGFSLNGKIKRS
DFKFATSTSTITLSDDINLNIEVKANEKEGGSHHHHHH**
*CJ DNA Sequence*
TTAAGAAGGAGATATACATATGAAAAAAGTTCTGCTGAGCAGCCTGGTTGCAGTTAGCCTGCTGAGT
ACCGGTCTGTTTGCAAAAGAATATACCCTGGATAAAGCCCATACCGATGTTGGCTTTAAAATCAAACA
TCTGCAGATTAGCAATGTGAAAGGCAACTTTAAAGATTATAGCGCAGTGATCGATTTTGATCCGGCAA
GTGCAGAATTCAAAAAACTGGATGTGACCATTAAAATCGCCAGCGTGAATACCGAAAATCAGACCCG
TGATAATCATCTGCAGCAGGATGACTTCTTCAAAGCCAAAAAATACCCGGATATGACCTTTACCATGA
AAAAATACGAGAAAATCGATAACGAAAAAGGCAAAATGACCGGCACCCTGACCATTGCCGGTGTTAG
CAAAGATATTGTTCTGGATGCAGAAATTGGTGGTGTTGCCAAAGGTAAAGATGGCAAAGAAAAAATT
GGCTTTAGCCTGAACGGCAAAATCAAACGTAGCGATTTCAAATTTGCAACCAGCACCAGCACCattAC
CCTGAGTGATGACATTAATCTGAACATTGAAGTGAAAGCCAACGAGAAAGAAGGTGGTAGTCATCAC
CACCACCATCACTAATAACTCGAGCACCACCACCACCACCACTGAGATCCGGCTG

*CJΔH6 Protein Sequence*
MHHHHHHENLYFQGKEYTLDKAHTDVGFKIKHLQISNVKGNFKDYSAVIDFDPASAEFKKLDVTIKIASVN
TENQTRDNHLQQDDFFKAKKYPDMTFTMKKYEKIDNEKGKMTGTLTIAGVSKDIVLDAEIGGVAKGKDGK
EKIGFSLNGKIKRSDFKFATSTSTITLSDDINLNIEVKANEKE**TADDY
*CJΔH6 DNA Sequence*
TCCCCTCTAGAAATAATTTTGTTTAACTTTAAGAAGGAGATATACATATGCATCACCACCACCATCACG
AAAATTTGTATTTCCAGGGAAAAGAATATACCCTGGATAAAGCCCATACCGATGTTGGCTTTAAAATC
AAACATCTGCAGATTAGCAATGTGAAAGGCAACTTTAAAGATTATAGCGCAGTGATCGATTTTGATCC
GGCAAGTGCAGAATTCAAAAAACTGGATGTGACCATTAAAATCGCCAGCGTGAATACCGAAAATCAG
ACCCGTGATAATCATCTGCAGCAGGATGACTTCTTCAAAGCCAAAAAATACCCGGATATGACCTTTAC
CATGAAAAAATACGAGAAAATCGATAACGAAAAAGGCAAAATGACCGGCACCCTGACCATTGCCGGT
GTTAGCAAAGATATTGTTCTGGATGCAGAAATTGGTGGTGTTGCCAAAGGTAAAGATGGCAAAGAAA
AAATTGGCTTTAGCCTGAACGGCAAAATCAAACGTAGCGATTTCAAATTTGCAACCAGCACCAGCAC
CATTACCCTGAGTGATGACATTAATCTGAACATTGAAGTGAAAGCCAACGAGAAAGAATGATGAACC
GCCGATGATTATTGAGATCCGGCTGCTAACAAAGCCCGAAAGGAAGCT

Figure S1. Protein sequences

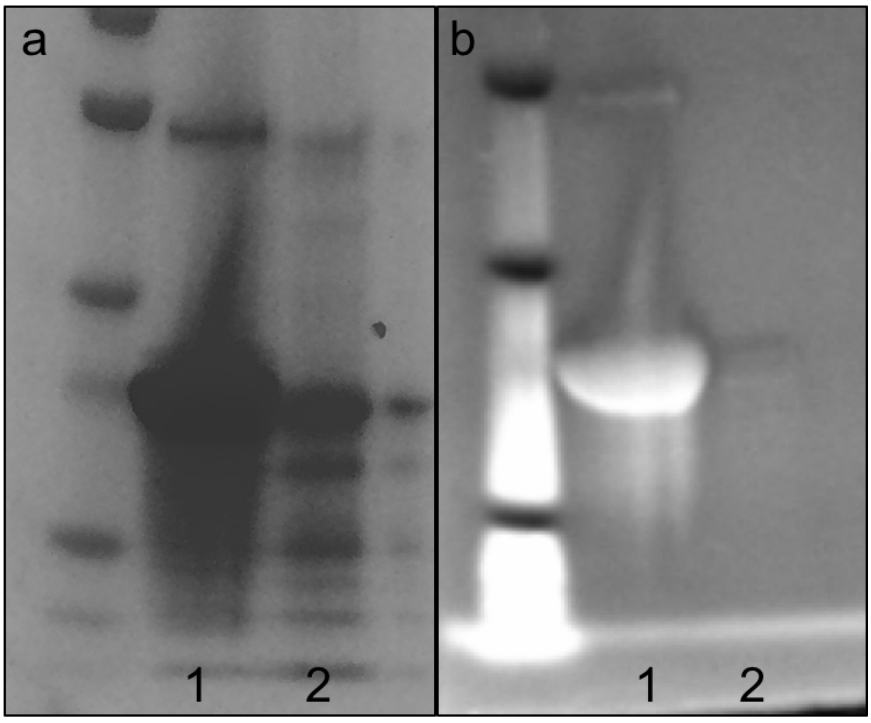


Figure S2. SDS-Page of purified protein samples (1) CJ and (2) CJ ΔH6 after (a) total protein staining by Coomassie and (b) InVision™ His-tag staining and UV transillumination.

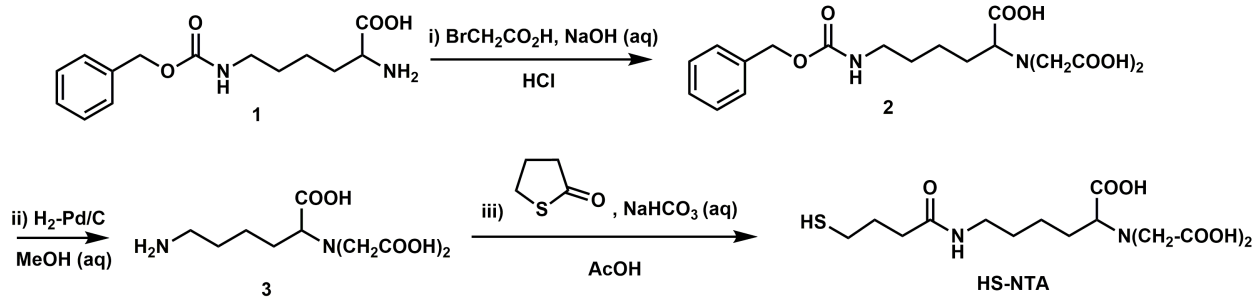


Scheme S1. Synthesis of HS-NTA

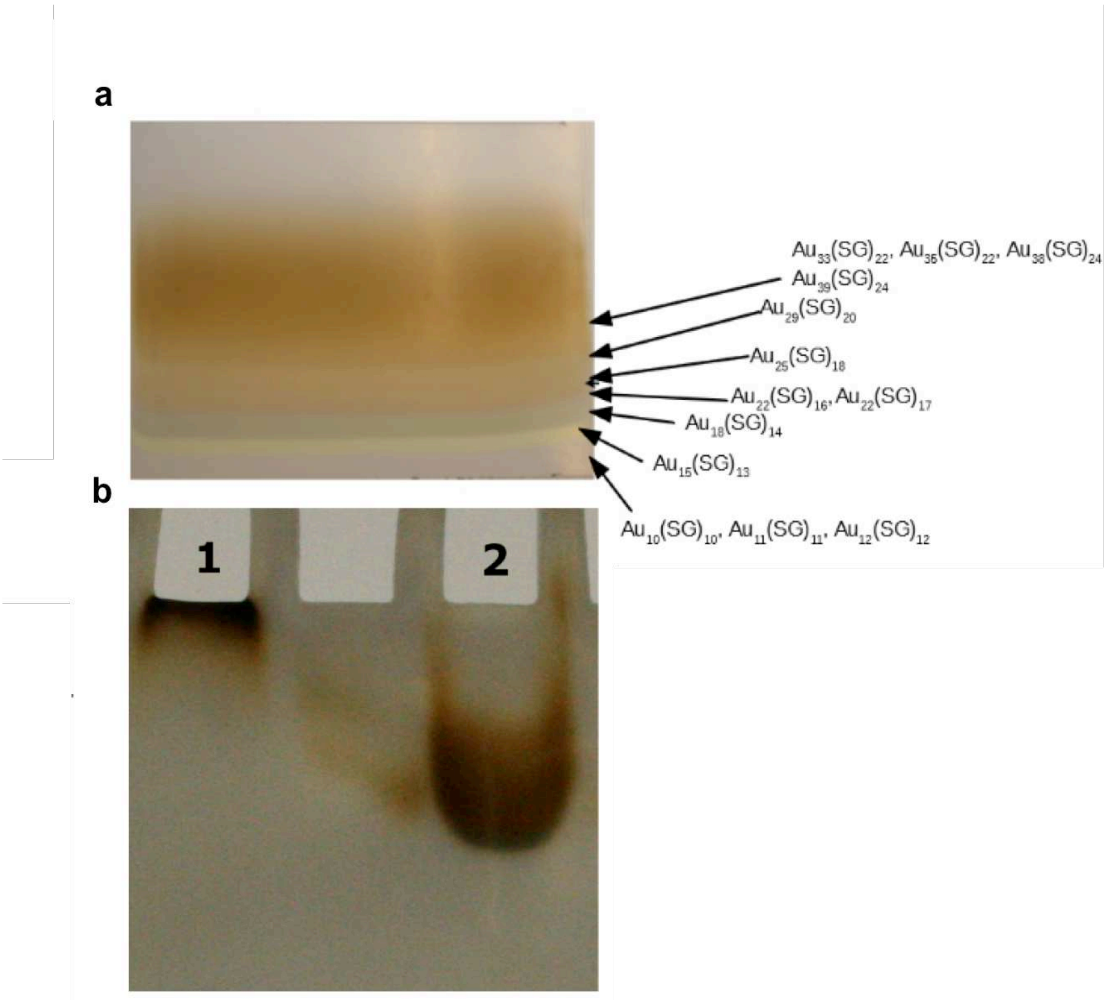


Figure S3. (a) Representative gel purification of crude $Au_{25}(GSH)_{18}$. (b) Representative gel of (1) $Au_{25}(GSH)_{18}$ and (2) $Au_{25}(GSH)_{17}NTA$. After ligand exchange the sample runs farther down the gel due to increased charge on the ligand layer.

| Lower Resolution (Å) | High Resolution (Å) | Average I | Average Error | CC1/2 | CC* | |
|---|---|---|---|---|---|---|
| 50 | 10.47 | 36.8 | 1.7 | 0.999 | 1 | |
| 10.47 | 8.33 | 12.6 | 1.2 | 0.989 | 0.997 | |
| 8.33 | 7.28 | 4.9 | 1 | 0.911 | 0.976 | |
| 7.28 | 6.61 | 5 | 1.1 | 0.995 | 0.999 | |
| 6.61 | 6.14 | 2.9 | 1.2 | 0.857 | 0.961 | |
| 6.14 | 5.78 | 4.1 | 1.3 | 0.816 | 0.948 | |
| 5.78 | 5.49 | 2.8 | 1.3 | 0.863 | 0.963 | |
| 5.49 | 5.25 | 3.1 | 1.4 | 0.786 | 0.938 | |
| 5.25 | 5.05 | 3.6 | 1.6 | 0.867 | 0.964 | |
| 5.05 | 4.88 | 3.4 | 1.6 | 0.671 | 0.896 | |
| 4.88 | 4.72 | 3.7 | 1.7 | 0.562 | 0.848 | |
| 4.72 | 4.59 | 3.9 | 1.8 | 0.866 | 0.963 | |
| 4.59 | 4.47 | 4.6 | 1.8 | 0.481 | 0.806 | |
| 4.47 | 4.36 | 5.7 | 1.9 | 0.061 | 0.338 | |
| 4.36 | 4.26 | 5.2 | 2.1 | 0.511 | 0.823 | ← High Resolution Estimate |
| 4.26 | 4.17 | 2.6 | 2.1 | 0.25 | 0.633 | |
| 4.17 | 4.09 | 2.6 | 2.2 | 0.756 | 0.928 | |
| 4.09 | 4.01 | 2.2 | 2.2 | 0.424 | 0.772 | |
| 4.01 | 3.94 | 1.4 | 2.3 | 0.424 | 0.772 | |

Table S1. Scala output log for 10 frame diffraction check on a CJ crystal incubated in 1 mg/mL $Au_{25}(GSH)_{17}(NTA)$ for 30 min.

| Lower Resolution (Å) | High Resolution (Å) | Average I | Average Error | CC1/2 | CC* | |
|---|---|---|---|---|---|---|
| 50 | 11.36 | 34.8 | 1.5 | 1 | 1 | |
| 11.36 | 9.03 | 21.7 | 1.2 | 0.988 | 0.997 | |
| 9.03 | 7.9 | 11.2 | 1 | 0.996 | 0.999 | |
| 7.9 | 7.18 | 7 | 1 | 0.984 | 0.996 | |
| 7.18 | 6.66 | 5.7 | 1.1 | 0.942 | 0.985 | |
| 6.66 | 6.27 | 4.7 | 1.1 | 0.733 | 0.92 | |
| 6.27 | 5.96 | 3.8 | 1.1 | 0.94 | 0.985 | |
| 5.96 | 5.7 | 4.4 | 1.2 | 0.915 | 0.978 | |
| 5.7 | 5.48 | 3 | 1.2 | 0.864 | 0.963 | |
| 5.48 | 5.29 | 3.3 | 1.4 | 0.922 | 0.979 | |
| 5.29 | 5.13 | 3.9 | 1.3 | 0.665 | 0.894 | |
| 5.13 | 4.98 | 5.1 | 1.5 | 0.851 | 0.959 | |
| 4.98 | 4.85 | 5.1 | 1.6 | 0.838 | 0.955 | |
| 4.85 | 4.73 | 6.5 | 1.5 | 0.962 | 0.99 | |
| 4.73 | 4.62 | 5.3 | 1.7 | 0.94 | 0.984 | |
| 4.62 | 4.52 | 6.9 | 1.7 | 0.752 | 0.927 | |
| 4.52 | 4.43 | 3.5 | 1.8 | 0.482 | 0.807 | |
| 4.43 | 4.35 | 4.7 | 1.7 | 0.541 | 0.838 | |
| 4.35 | 4.27 | 6.8 | 2.3 | 0.81 | 0.946 | ← **High Resolution Estimate** |
| 4.27 | 4.2 | 6.5 | 2 | 0.342 | 0.714 | |

Table S2. Scala output log for 10 frame diffraction check on a CJ crystal after 30 min incubation in 1 mg/mL $Au_{25}(GSH)_{17}(NTA)$ min followed by 30 min incubation in 0.1M EDTA at pH 7.0.

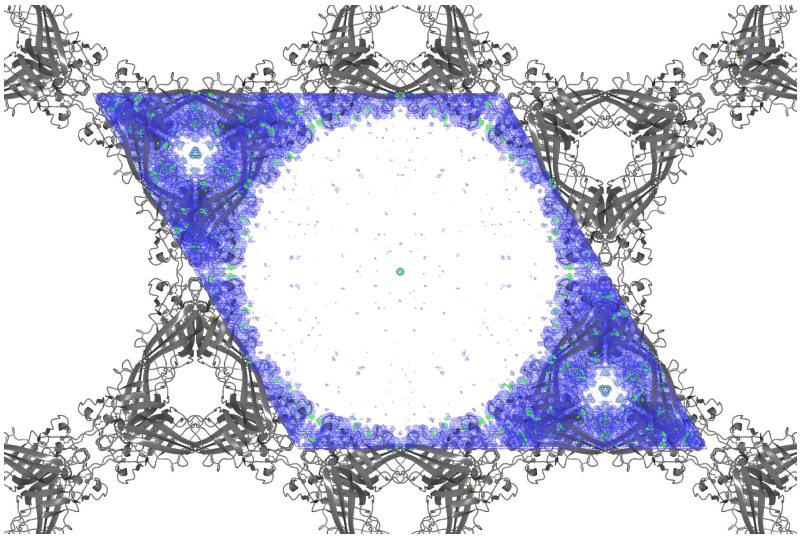

Figure S4. 2Fo-Fc map contoured to 1s (blue) and Fo-Fc difference map contoured to 3s (green) reveals no obvious preferred $Au_{25}(GSH)_{17}(NTA)$ binding orientation in the crystal solvent pore after 2 hr incubation.

| **Data Collection** | | **CJ Au25 2 hr load** |
|---|---|---|
| Space group | | P 6 2 2 |
| Unit cell Dimensions: | a (Å) | 178.461 |
| | b (Å) | 178.461 |
| | c (Å) | 50.1605 |
| Total reflections | | 16044 (1244) |
| Unique reflections | | 8220 (750) |
| Multiplicity | | 2.0 (1.7) |
| Completeness (%) | | 0.99 (0.93) |
| Mean I/σ(I) | | 11.78 (1.10) |
| Wilson B-factor | | 56.65 |
| $R_{merge}$ | | 0.0621 (0.5722) |
| $R_{meas}$ | | 0.08783 (0.8092) |
| $CC_{1/2}$ | | 0.995 (0.59) |
| CC* | | 0.999 (0.862) |
| **Refinement** | | |
| Reflections used in refinement | | 8207 (750) |
| Reflections used for R-free | | 398 (33) |
| $R_{work}$ | | 0.2349 (0.3236) |
| $R_{free}$ | | 0.2625 (0.3277) |
| CC(work) | | 0.943 (0.584) |
| CC(free) | | 0.886 (0.789) |
| RMS(bonds) | | 0.012 |
| RMS(angles) | | 1.65 |
| Average B-factor | | 55.12 |
| macromolecules | | 55.47 |
| ligands | | 48.46 |
| solvent | | 30.58 |
| Reflection statistics for the highest-resolution shell are shown in parentheses | | |

Table S3. X-ray diffraction data and refinement statistics for CJ crystal with 5T05L crosslink followed by 2 hour incubation in $Au_{25}(GSH)_{17}(NTA)$.

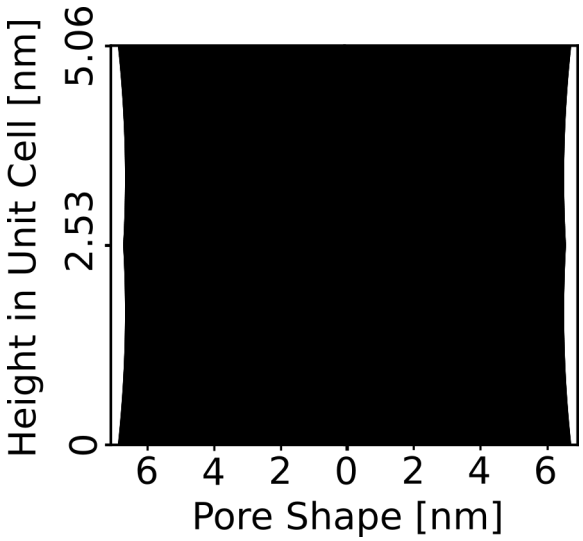


Figure S5. The pore diameter varies only slightly along the z-axis (13.1 to 13.6 nm). From any point along the pore center line, the minimum distance to a heavy atom in the protein crystal (including z-axis periodicity) is 6.57 nm.

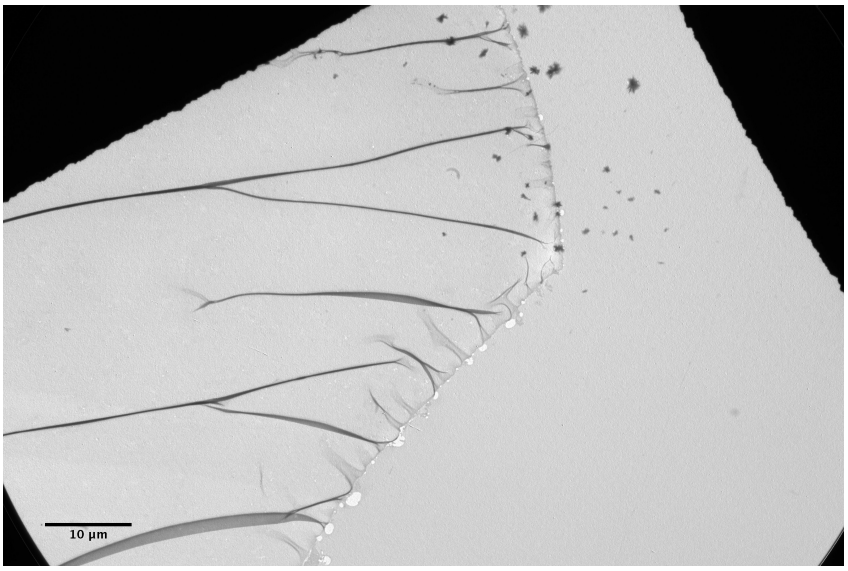


Figure S6. Ultramicrotomed section of CJ crystal on a TEM grid shows folding and warping. Scale bar is 10 µm.

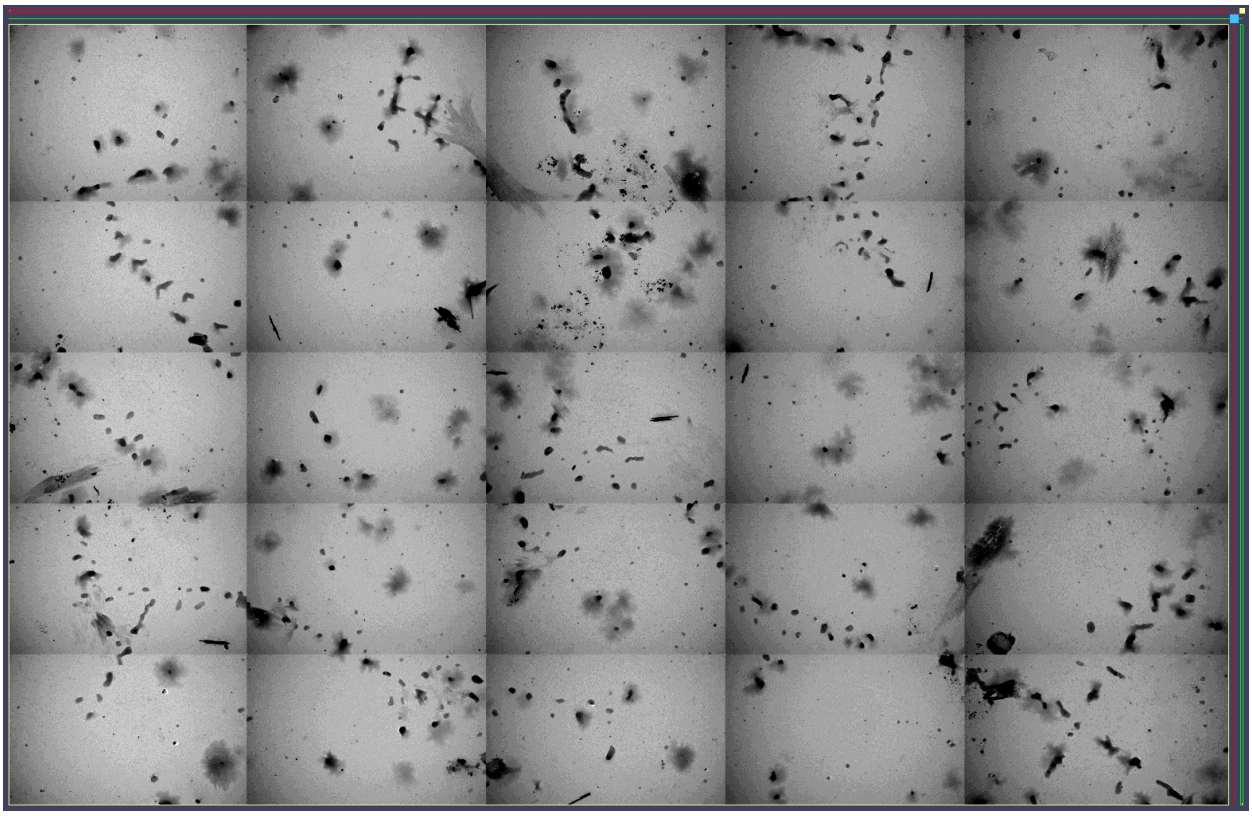

Figure S7. TEM montage showing the products after gold growth by 1 mg/mL $Au_{25}$, 10 mM $HAuCl_4$, and 10 mM ascorbic acid. Various products including rods, rod bundles, and particles are all visible within a single sample.

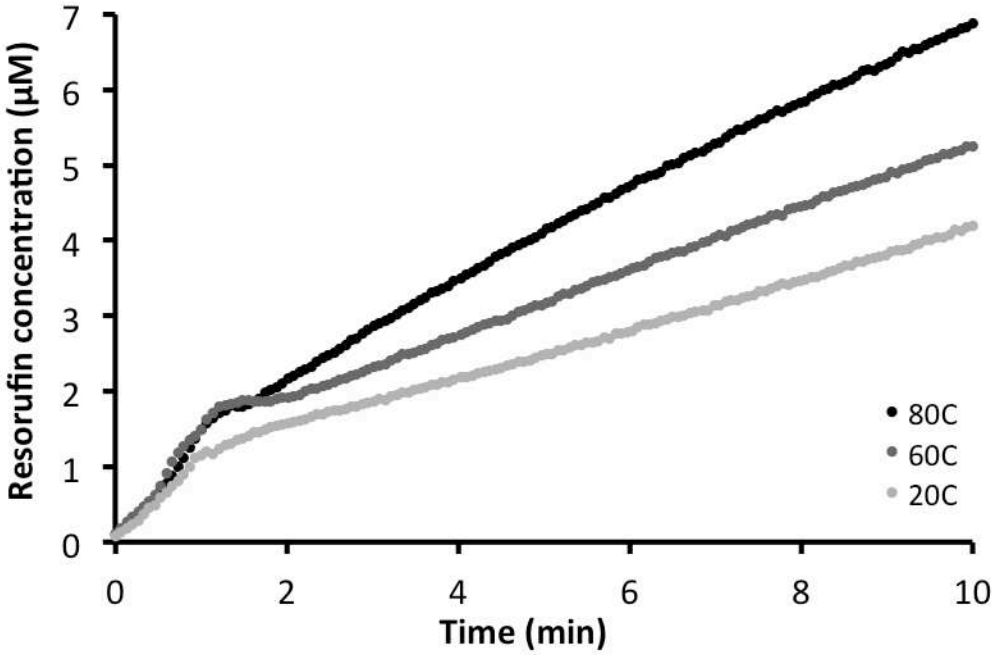

Figure S8. Three CJ crystals of equal volume, each loaded with the same concentration of hHRP, were incubated at 80°C, 60°C, or room temperature for 10 minutes. After 10 mins, the 80°C and 60°C were held at 45°C for 10 mins while product formation was monitored at 561 nm light on a fluorescence plate reader. 100μM AmplexRed and 100μM $H_2O_2$ were used as the substrates.

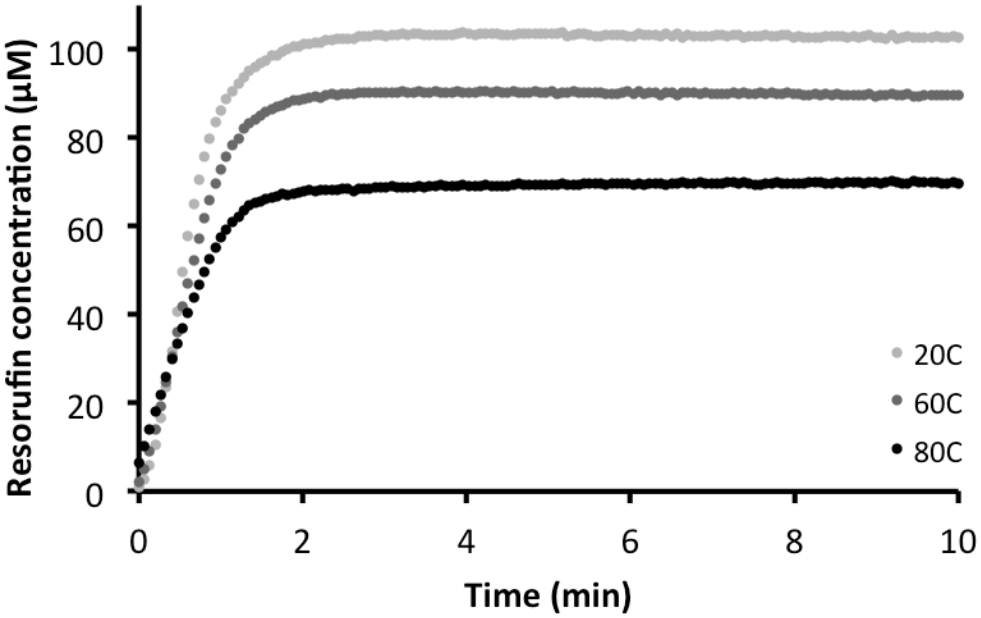


Figure S9. Three solutions of the same concentration of hHRP, were incubated at 80°C, 60°C, or room temperature for 10 minutes. After 10 mins, the 80°C and 60°C were held at 45°C for 10 mins while product formation was monitored at 561 nm light on a fluorescence plate reader. 100μM AmplexRed and 100μM $H_2O_2$ were used as the substrates.

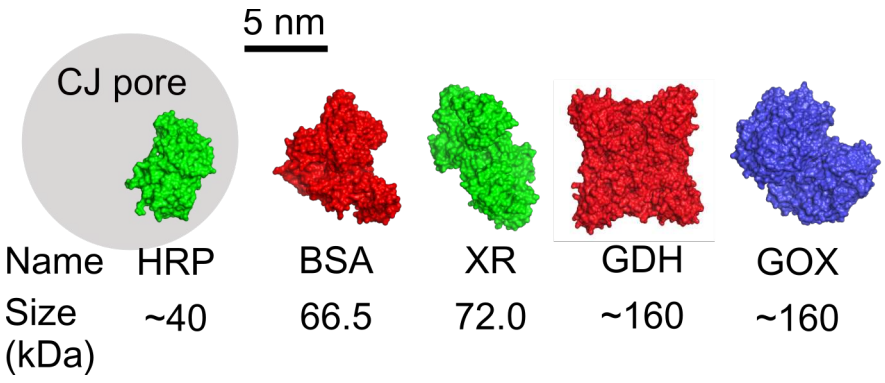


Figure S10. Crosslinked CJ crystals are able to load macromolecules of sizes up to 160 kDa.

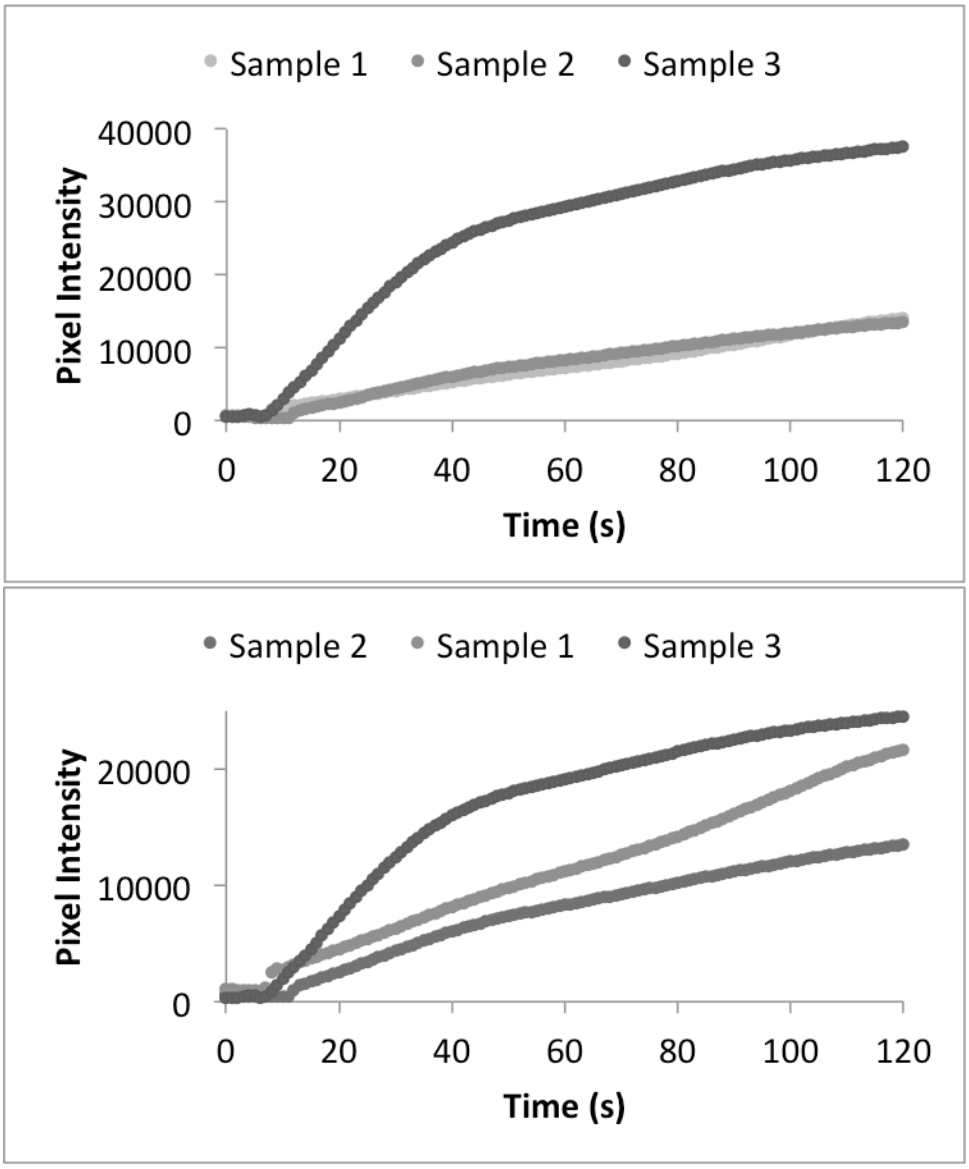


Figure S11. In order to confirm that the pixel intensity measurements from Figure 4.5 were not biased by the choice of 25 x 25 $\mu m^2$ box from which to average the pixel intensity, the entire confocal microscope field of view was used to determine the increasing pixel intensity during product formation. The top graph shows the raw pixel intensity data while, similarly to Figure 4.5, the volume normalization in the bottom graph removes variation among samples. Each sample consisted of a CJ crystal loaded with 0.5 mg/mL hHRP and 1.5 mg/mL GOx and exposed to 10 μM AmplexRed and 100 μM glucose while product formation was monitored under 561 nm light on a spinning disk confocal microscope.